

**Study of Branching Ratio and Polarization Fraction in Neutral B Meson
Decays to Negative Rho Meson Positive Kaon Resonance**

Baosen Cheng

Stanford Linear Accelerator Center
Stanford University
Stanford, CA 94309

SLAC-Report-806

Prepared for the Department of Energy
under contract number DE-AC02-76SF00515

Printed in the United States of America. Available from the National Technical Information Service, U.S. Department of Commerce, 5285 Port Royal Road, Springfield, VA 22161.

This document, and the material and data contained therein, was developed under sponsorship of the United States Government. Neither the United States nor the Department of Energy, nor the Leland Stanford Junior University, nor their employees, nor their respective contractors, subcontractors, or their employees, makes an warranty, express or implied, or assumes any liability of responsibility for accuracy, completeness or usefulness of any information, apparatus, product or process disclosed, or represents that its use will not infringe privately owned rights. Mention of any product, its manufacturer, or suppliers shall not, nor is it intended to, imply approval, disapproval, or fitness of any particular use. A royalty-free, nonexclusive right to use and disseminate same of whatsoever, is expressly reserved to the United States and the University.

STUDY OF BRANCHING RATIO AND
POLARIZATION FRACTION IN $B^0 \rightarrow \rho^- K^{*+}$

by

Baosen Cheng

A dissertation submitted in partial fulfillment
of the requirements for the degree of

Doctor of Philosophy

(Physics)

at the

UNIVERSITY OF WISCONSIN-MADISON

2005

Abstract

We present the preliminary results on the search for $B^0 \rightarrow \rho^- K^{*+}$. The data sample comprises 122.7 million $B\bar{B}$ pairs in the e^+e^- annihilation through the $\Upsilon(4S)$ resonance collected during 1999-2003 with the *BABAR* detector at the PEP-II asymmetric-energy collider at Stanford Linear Accelerator Center (SLAC). We obtain an upper limit of the branching ratio at 90% confidence level as $\mathcal{B}(B^0 \rightarrow \rho^- K^{*+}) < 17.2 \times 10^{-6}$. The fitted result on the polarization fraction shows no evidence that the decay is longitudinally dominated as predicted by various theoretical models.

Acknowledgment

The analysis included in this dissertation would not simply be possible if not for the support, patience, and collaboration of many individuals. I would like to extend my gratitude first and foremost to my thesis advisor, Prof. Sau Lan Wu, for her guiding me through extremely difficult times over the duration of this work with her superb insight on physics. She is the kind of advisors others can only dream of having. No one but me can truly understand. She kindly accepted me into the Ph.D. program and provided me constant support during the past five years and for that I sincerely thank her for her firm, unwavering confidence in me.

Following the proposal of Dr. Haibo Li, this analysis was brought to life in which he also played a leading role. It's my great pleasure to work closely with him and learn a lot from him. His enthusiasm and persistence keep this work alive and have made it more fruitful.

Prof. Yibin Pan, Dr. Mathew Graham, and my officemates, Paul Kutter and Attila Mihalyi closely revised my thesis, and provided me useful suggestions and detailed corrections. Many thanks go to them, as well as other members in *BABAR* Wisconsin group, from whom I got helpful discussions and invaluable advices.

Stanford Linear Accelerator Center (SLAC) is the host of the *BABAR* experiment and SLAC people provide comfortable and convenient working environment for its users. I'd like to take this opportunity to thank them for their excellent jobs.

Last but not least, I would like to thank all my family and friends for their continuous support and encouragement. Especially, I would like to extend my deepest appreciation

to my wife. She joined me for my study and sustained me with her love, patience and understanding. During the course of this work, she brought me the most treasured gift, my son Daniel, and took great care of him. They are always my strong backing forces.

Contents

Abstract	i
Acknowledgement	ii
1 Theory	1
1.1 Introduction	1
1.2 The Standard Model	2
1.3 The CKM Matrix	4
1.4 Signal Decay Modes	6
1.5 Decay Diagrams	7
1.6 Low Energy Effective Hamiltonian	8
1.7 $B \rightarrow VV$ Decay	8
2 The <i>BABAR</i> Experiment	15
2.1 Introduction	15
2.2 PEP-II Asymmetric B Factory	16
2.3 The <i>BABAR</i> Detector	18
2.3.1 Silicon Vertex Tracker (SVT)	20
2.3.2 Drift Chamber (DCH)	22
2.3.3 Detector of Internally Reflected Cherenkov light (DIRC)	26

2.3.4	Electromagnetic Calorimeter (EMC)	28
2.3.5	Instrumental Flux Return (IFR)	30
2.3.6	Trigger System	32
2.3.7	Online System	34
3	Analysis Approach	35
3.1	Data Sets	36
3.2	Monte Carlo (MC) Simulation	36
3.3	Event Reconstruction	38
3.3.1	Discriminating Variables	38
3.3.2	Events Pre-selection	40
3.3.3	Candidate Selection	41
3.3.4	Multiple Candidate and Signal Misreconstruction	42
3.3.5	Suppression of Continuum Background	45
3.3.6	Classification of B Related Backgrounds	47
3.3.7	Suppression of Peaking Charm B Backgrounds - D^0 Veto	49
3.3.8	Efficiencies	52
3.4	Maximum Likelihood (ML) Fit	52
3.4.1	The Likelihood Function	53
3.4.2	PDF Definitions	55
3.4.3	PDF Correlations	56
3.5	Fit Validations	57
3.5.1	Fits to Toy MC Samples - Pull Distributions	58
3.5.2	Fits to the Mixture of Signal MC Events and Toy Samples	58
3.5.3	Fits to MC Samples and Offpeak Data	60
3.6	Fit Stability Tests	61

3.7	Fit Result	62
3.7.1	Nominal Fit to Onpeak data	62
3.7.2	Goodness of Fit	63
3.7.3	Projection Plots	64
3.8	Systematic Uncertainties	65
3.8.1	Branching Ratio of B -Backgrounds	65
3.8.2	SCF Fraction	66
3.8.3	Ratio of Longitudinal and Transverse Signal Efficiencies	67
3.8.4	Uncertainties Relating to the ML Fit	68
3.8.5	Particle Identification	69
3.8.6	Neutral Correction	69
3.8.7	Tracking Efficiency	69
3.8.8	B Counting	70
3.8.9	Longitudinal Polarization Fraction f_L	70
3.8.10	Non-resonance Contributions	70
3.8.11	Summary of the Systematic Uncertainties	72
3.9	Results and Summary	73
A	Charmless B Decay modes	76
B	Distributions of the Discriminating Variables	82
C	Correlations Between Discriminating Variables	102
	Bibliography	108

Chapter 1

Theory

1.1 Introduction

Understanding the structure of matter has been a constant pursuit in the history of human civilization. From the “four elements” of the ancient Greeks (or “five elements” of ancient Chinese) to modern quarks, people’s knowledge on matters goes deeper and deeper. Nowadays, it is believed that quarks and leptons are fundamental building blocks of matters. These fundamental particles interact with each other by exchange of four fundamental forces: weak, electromagnetic, strong, and gravitational. Two of the forces, namely electromagnetic and weak, are unified in a so-called electroweak theory which was first proposed by S. Weinberg and A. Salam in the 1960’s [1]. It is also believed that the strong and the unified electroweak forces can be again unified at much higher energy of 10^{14} GeV (as compared to the electroweak scale of 100 GeV). Much of these understandings are summarized in the Standard Model (SM) and its extensions. The Standard Model provides an excellent description of the electroweak and strong interactions for the quarks and leptons, agreeing with experimental data up to the energy scale of today’s most powerful accelerators. However, being the most successful theory in modern particle physics, the SM is not the ultimate

theory and it still leaves many questions open. One of the major tasks of modern high energy particle experiments is to precisely test the SM's various predictions and to intensively probe its possible extensions. This work is just one of such efforts.

This chapter gives a short review of particle theories most relevant to this work. The Standard Model and the CKM matrix are briefly reviewed in Section 1.2, 1.3. Section 1.4-1.7 discuss in detail about this analysis and the available results of some other charmless $B \rightarrow VV$ decay modes are given for comparison.

1.2 The Standard Model

The Standard Model (SM) is a theory of elementary particles and their interactions. In the SM, the constituents of all matters are fundamental fermions with an intrinsic spin of $\frac{1}{2}$. There are six quarks of down (d), up (u), strange (s), charm (c), bottom (b), top (t), and six leptons of e , ν_e , μ , ν_μ , τ , ν_τ , grouped into three generations doublets, $\begin{pmatrix} e^- \\ \nu_e \end{pmatrix}$, $\begin{pmatrix} d \\ u \end{pmatrix}$ for the first generation, $\begin{pmatrix} \mu^- \\ \nu_\mu \end{pmatrix}$, $\begin{pmatrix} s \\ c \end{pmatrix}$ for the second generation, and $\begin{pmatrix} \tau^- \\ \nu_\tau \end{pmatrix}$, $\begin{pmatrix} b \\ t \end{pmatrix}$ for the third generation. The mass of quarks varies significantly from several hundred MeV/ c^2 in the first generation to the heaviest t quark ($\sim 174 \text{ GeV}/c^2$) in the third generation. While the charged leptons have mass of 0.511 MeV/ c^2 for e^- , 106 MeV/ c^2 for μ^- , and 1.777 GeV/ c^2 for τ^- , the neutrinos have very tiny masses and are practically considered as massless. These fermions interact with each other by exchanging gauge bosons of spin 1. In the SM, only three fundamental forces, strong, electromagnetic, and weak interactions, are accounted for, while the gravitation is excluded.

Electromagnetic interactions are mediated by photon (γ) exchange between charged fermions. Photon is massless and the electromagnetic interaction is a long-range force cou-

pling to electric charge with strength proportional to $\sqrt{\alpha}$ ($\alpha \sim \frac{1}{137}$). Electromagnetic interactions are well described in Quantum Electrodynamics (QED), where interactions are expanded in the perturbation series with the transition amplitude proportional to α^2 . Since $\alpha < 1$, the lowest order (two vertices) dominates. QED is the most studied and understood aspect of the SM.

Similar to QED, Quantum Chromodynamics (QCD) is the quantum theory of strong interactions, which take place between quarks and are mediated by massless gluons with a coupling constant of α_s . Both quarks and gluons carry “colors” strong charges, just like the electric charge in QED. In QCD, gluons can interact with other gluons. This strong self-interaction of gluons causes quarks to be confined within hadrons. At high energies, α_s is small, close to 0 (asymptotic freedom) [2]. The perturbation theory like the one used in QED is still applicable. However at low energies, α_s becomes large. This makes using the perturbation theory much harder, if not impossible.

Weak Interactions are very short-ranged interactions involving both quarks and leptons. At low energies ($q^2 \ll m_W^2$), weak interactions are taken to be four-fermion pointlike interactions with the Fermi coupling strength of G_F ($G_F = 1.166 \times 10^{-5} \text{ GeV}^{-2}$), while at high energies, Fermi theory breaks down and weak interactions are described by the exchange of the massive bosons, W^\pm for charged current and Z^0 for neutral current interactions. In the SM, the charged current has a pure $V - A$ form, $\gamma^\mu(1 - \gamma^5)$, and the neutral current takes the form $\gamma^\mu(c_V - c_A\gamma^5)$, where in general $c_V \neq c_A$. Weak interactions exhibit the violation of parity transformation, which reverses the sign of the space while leaving spin and time unchanged. This means that weak interactions treat left-handed (spin anti-parallel to the direction of motion) and right-handed (spin parallel to the direction of motion) particles differently. In the relativistic (massless) limit only left-handed particles and right-handed anti-particles participate in weak interactions. For fermions with mass, weak interactions couple preferentially to left-handed particles or right-handed anti-particles, because neutral

currents have right-handed components. This argument is very important to this analysis (see Section 1.7).

The complete theory to describe the weak interaction is achieved together with the unification of the electromagnetic interaction. The electroweak theory is a spontaneously symmetry breaking gauge theory, based on the gauge group $SU(2)_L \times U(1)_Y$, where L denotes that the weak isospin current couples only left-handed fermions, Y is the weak hypercharge defined by $Q = T^3 + \frac{Y}{2}$, where T^3 is the third component of weak isospin. There are four massless mediating bosons, an isotriplet of $W_\mu^i, i = 1, 2, 3$, coupled to the weak isospin current J_μ^i , and an isosinglet of B_μ coupled to the weak hypercharge current J_μ^Y , from which the physical bosons are constructed:

$$\begin{aligned} W^\pm &= \sqrt{\frac{1}{2}} (W_\mu^1 \mp iW_\mu^2) \\ Z_\mu &= W_\mu^3 \cos\theta_W - B_\mu \sin\theta_W \\ A_\mu &= W_\mu^3 \sin\theta_W + B_\mu \cos\theta_W \end{aligned} \tag{1.1}$$

where neutral bosons, W_μ^3 and B_μ , are mixed with the weak mixing angle θ_W to give the fields for Z^0 and γ . Both the Z^0 and the γ are combinations of $SU(2)_L$ part $U(1)$ gauge bosons, so the coupling of the Z^0 is now a mixture of electromagnetic (V) and weak ($V - A$) couplings. The physical bosons W^\pm and Z^0 acquire mass via the Higgs mechanism [3], while the γ remains massless.

1.3 The CKM Matrix

One of the most important effects in weak interactions is flavor mixing: weak eigenstates are different from mass eigenstates. For three generation quarks, they are connected with the

three-dimension unitary Cabibbo-Kobayashi-Maskawa (CKM) matrix [4],

$$\begin{pmatrix} d' \\ s' \\ b' \end{pmatrix} = \begin{pmatrix} V_{ud} & V_{us} & V_{ub} \\ V_{cd} & V_{cs} & V_{cb} \\ V_{td} & V_{ts} & V_{tb} \end{pmatrix} \begin{pmatrix} d \\ s \\ b \end{pmatrix} = V_{CKM} \begin{pmatrix} d \\ s \\ b \end{pmatrix}, \quad (1.2)$$

where each element $V_{q_i q_j}$ represents the amplitude of flavor changing charged current weak interactions between q_i and q_j .

The unitarity of the CKM matrix can be manifested using an explicit parametrization in terms of three rotation angles θ_{12} , θ_{23} , θ_{13} and a complex phase δ ,

$$V_{CKM} = \begin{pmatrix} c_{12}c_{13} & s_{12}c_{13} & s_{13}e^{-i\delta} \\ -s_{12}c_{23} - c_{12}s_{23}s_{13}e^{i\delta} & c_{12}c_{23} - s_{12}s_{23}s_{13}e^{i\delta} & s_{23}c_{13} \\ s_{12}s_{23} - c_{12}c_{23}s_{13}e^{i\delta} & -c_{12}s_{23} - s_{12}c_{23}s_{13}e^{i\delta} & c_{23}c_{13} \end{pmatrix}. \quad (1.3)$$

where $c_{ij} = \cos \theta_{ij}$ and $s_{ij} = \sin \theta_{ij}$ ($i \neq j$ and $i, j = 1, 2, 3$).

Three generations are necessary for the presence of the complex phase, whose non-zero values indicate CP violations for the weak interactions.

Most of the matrix elements can be measured directly by tree-level processes. Using the available experimental data, together with the CKM unitarity constraints, we have the 90% confidence limits on the magnitudes of the CKM elements of the complete matrix [5]

$$V_{CKM} = \begin{pmatrix} 0.9739 - 0.9751 & 0.221 - 0.227 & 0.0029 - 0.0045 \\ 0.221 - 0.227 & 0.9730 - 0.9744 & 0.039 - 0.044 \\ 0.0048 - 0.014 & 0.034 - 0.046 & 0.9990 - 0.9992 \end{pmatrix}. \quad (1.4)$$

The matrix is almost diagonal and the magnitudes of matrix elements show the hierarchy of the strengths of the charged-current process between different generations. To see it more

explicit, it is useful to express CKM matrix with four Wolfenstein parameters (λ, A, ρ, η) [6] and the matrix elements are expanded in terms of powers of λ ($\lambda = |V_{us}| \approx 0.22$),

$$V_{CKM} = \begin{pmatrix} 1 - \frac{\lambda^2}{2} & \lambda & A\lambda^3(\rho - i\eta) \\ -\lambda & 1 - \frac{\lambda^2}{2} & A\lambda^2 \\ A\lambda^3(1 - \rho - i\eta) & -A\lambda^2 & 1 \end{pmatrix} + \mathcal{O}(\lambda^4). \quad (1.5)$$

1.4 Signal Decay Modes

In this analysis, we are interested in the process of B^0 meson decaying into K^{*+} and ρ^- mesons ($B^0 \rightarrow \rho^- K^{*+}$).¹ In the SM, mesons are the bound states of a quark and an antiquark. Since the quark has a spin of $\frac{1}{2}$, mesons can have spin 0 (pseudoscalar mesons) or spin 1 (vector mesons). The B^0 meson, made of a d quark and a \bar{b} quark, has a mass of 5.279 GeV/ c^2 , a life time of $c\tau = 460 \mu\text{m}$, and a spin of 0. Most of the time, the B^0 decays to final state with at least a c quark in its decay chains. The branching ratio of charmless decay is usually very small. For $B^0 \rightarrow \rho^- K^{*+}$, it is approximately at the order of 10^{-6} . The K^{*+} is made of a u quark and an \bar{s} quark with a mass of 0.89166 GeV/ c^2 , while the ρ^- of a \bar{u} quark and a d quark with a mass of 0.7711 GeV/ c^2 . Both of them are vector mesons. The ρ^- decays dominantly to $\pi^-\pi^0$ ($\sim 100\%$), and the K^{*+} can decay to $K^+\pi^0$ ($\sim 33.3\%$) and $K^0\pi^+$ ($\sim 66.7\%$). At the quark level for the decay $B^0 \rightarrow \rho^- K^{*+}$, the \bar{b} quark decays as $\bar{b} \rightarrow \bar{s}u\bar{u}$ and the d quark is a spectator which does not participate in the decay. Both the strong and weak interactions are involved. This is discussed in more detail in the following sections.

¹Charge conjugate is implied through out this analysis.

1.5 Decay Diagrams

For the $B^0 \rightarrow \rho^- K^{*+}$ decay, both tree and penguin diagrams will contribute to the final state (see Figure 1.1). The tree diagram contains the exchange of a W boson between two charged currents. This involves two weak vertices, $V_{ub} \sim A\lambda^3$ and $V_{us} \sim \lambda$, thus the amplitude is proportional to $A\lambda^4$. The gluonic penguin happens at a one-loop level with a virtual t quark and a virtual W boson in the loop. The transition involves two weak vertices of $V_{tb} \sim 1$ and $V_{ts} \sim A\lambda^2$, and its amplitude is proportional to $A\lambda^2$. There are also electroweak penguin contributions, but they are suppressed due to the smaller electroweak coupling strength at the vertex of Z^0 (γ) comparing to the strong coupling strength at the vertex of gluon. Thus the gluonic penguin is CKM favored for this decay.

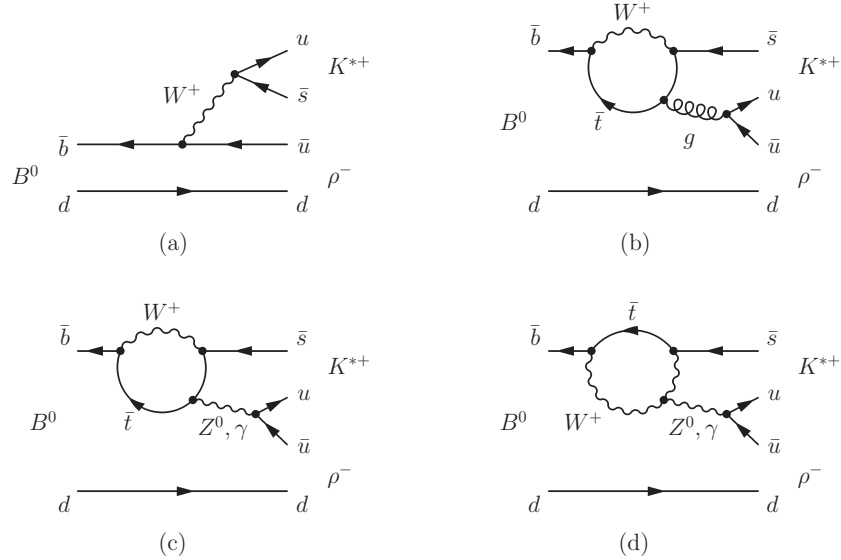


Figure 1.1: Tree, gluonic penguin and electroweak penguins. Gluonic penguin diagram (b) can be converted to an electroweak penguin by replacing the gluon with a Z^0 or γ (c). Electroweak penguin can also have Z^0 or γ emitted from a W^\pm (d).

1.6 Low Energy Effective Hamiltonian

Besides weak interactions, weak decays of hadrons also involve the strong interactions which bind the quarks into hadrons. The typical hadron energy has a scale of $\mu \approx \mathcal{O}(1 \text{ GeV})$, much lower than the scale of $\mathcal{O}(M_{W,Z})$ for weak interactions. In energetic two-body heavy meson decay, hadronization of the decay products becomes effective until they have traveled some distance away from each other. This allows us to separate the physics contributions to a decay amplitude into short-range contributions at scales higher than μ and long-range contributions at scales lower than μ . The hadronic scale μ is chosen large enough for perturbation theory to be applicable. The theoretical framework to study these decays is that of an effective theory by means of the Operator Product Expansion (OPE) [7].

In the case $|\Delta b| = 1$, $\Delta c = \Delta u = 0$, both tree and penguin processes will be present. The effective Hamiltonian can be written as [8]

$$\mathcal{H}_{eff} = \frac{G_F}{\sqrt{2}} \left\{ \sum_{j=u,c} \left[V_{jq}^* V_{jb} \sum_{k=1}^2 C_k(\mu) Q_k^{jq} \right] + V_{tq}^* V_{tb} \sum_{k=3}^{10} C_k(\mu) Q_k^q \right\} + h.c., \quad (1.6)$$

where G_F is the Fermi constant, the renormalization scale μ is of $\mathcal{O}(m_b)$, q denotes d, s quark corresponding to $b \rightarrow d$ and $b \rightarrow s$ transitions, respectively, $C_k(\mu)$ are the scale-dependent Wilson coefficients, and Q_k are the local operators. The heavy degrees of freedom is integrated out and contained in $C_i(\mu)$ while the non-perturbative long-distance soft gluons exchange effects are absorbed into the local four-quark operators $Q_i(\mu)$.

1.7 $B \rightarrow VV$ Decay

To calculate decay rates and angular correlations for $B \rightarrow V_1 V_2$, we need the matrix element $\langle V_1(\lambda_1) V_2(\lambda_2) | \mathcal{H}_{eff} | B \rangle$, where λ_1 and λ_2 are the helicities of the final-state vector particles

V_1 and V_2 . In the B rest frame, two-body decay products, the vector mesons V_1 and V_2 , are produced back-to-back, $\mathbf{p}_1 + \mathbf{p}_2 = 0$. Since the B is spinless, angular momentum conservation requires that V_1 and V_2 have opposite spins, thus have the same helicities $\lambda_1 = \lambda_2 \equiv \lambda$. We use the notation

$$A_\lambda = \langle V_1(\lambda)V_2(\lambda) | \mathcal{H}_{eff} | B \rangle \quad (1.7)$$

for the helicity matrix element. We have three independent helicity amplitudes A_0 , A_{-1} and A_{+1} , corresponding to $\lambda = 0, -1, +1$, respectively.

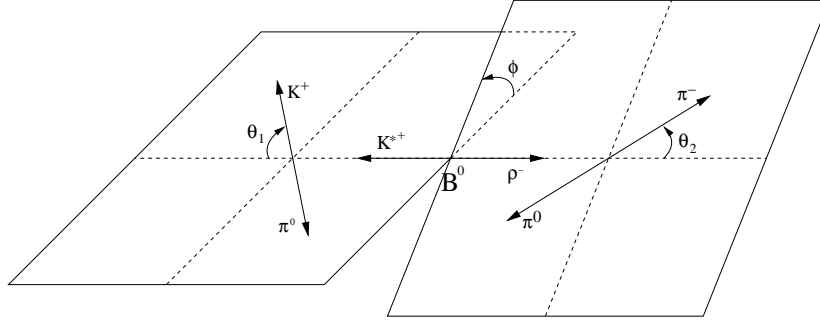


Figure 1.2: Definition of the helicity angles θ_1 , θ_2 , and the azimuth angle ϕ , for the decay $B^0 \rightarrow \rho^- K^{*+}$. The $K^+ \pi^0$ ($\pi^- \pi^0$) final states are shown in the K^{*+} (ρ^-) rest frame.

In general for $B \rightarrow V_1 V_2$ decay, the angular dependence can be expressed in terms of the spherical functions

$$\frac{d^3\Gamma}{d\cos\theta_1 d\cos\theta_2 d\phi} \propto \left| \sum_{|m| \leq J_1, J_2} A_m \times Y_{J_1, m}(\theta_1, \phi_1) \times Y_{J_2, -m}(\theta_2, \phi_2) \right|^2 \quad (1.8)$$

where A_m is the decay amplitude, J_1 (J_2) is the angular momentum quantum number for V_1 (V_2), θ_1 (θ_2) is the helicity angle of V_1 (V_2), which, for two-body decays of V_1 (V_2), is defined by the direction of the V_1 (V_2) decay axis and the direction of the B meson in the V_1 (V_2) rest frame, and $\phi = \phi_1 - \phi_2$ is the azimuthal angle between the two decay planes

(see Figure 1.2 for definition in $B^0 \rightarrow \rho^- K^{*+}$).

The exact form of the angular correlation depends on the spins of the decay product of the vector mesons V_1 and V_2 . For $B^0 \rightarrow \rho^- K^{*+}$, both K^{*+} and ρ^- decay into two pseudoscalar mesons, and the angular distribution takes the form [8]

$$\begin{aligned} \frac{1}{\Gamma} \frac{d^3\Gamma}{d\cos\theta_1 d\cos\theta_2 d\phi} = & \frac{9}{16\pi} \frac{1}{|A_0|^2 + |A_{+1}|^2 + |A_{-1}|^2} \\ & \times \left\{ \frac{1}{2} \sin^2\theta_1 \sin^2\theta_2 (|A_{+1}|^2 + |A_{-1}|^2) + 2 \cos^2\theta_1 \cos^2\theta_2 |A_0|^2 \right. \\ & + \sin^2\theta_1 \sin^2\theta_2 [\cos 2\phi \Re(A_{+1}A_{-1}^*) - \sin 2\phi \Im(A_{+1}A_{-1}^*)] \\ & \left. + \frac{1}{2} \sin 2\theta_1 \sin 2\theta_2 [\cos \phi \Re(A_{+1}A_0^* + A_{-1}A_0^*) - \sin \phi \Im(A_{+1}A_0^* - A_{-1}A_0^*)] \right\}. \quad (1.9) \end{aligned}$$

We may integrate the angular distribution over ϕ , assuming azimuthal uniformity of detector acceptance. We have

$$\frac{1}{\Gamma} \frac{d^2\Gamma}{d\cos\theta_1 d\cos\theta_2} = \frac{9}{4} \left[f_L \cos^2\theta_1 \cos^2\theta_2 + \frac{1}{4} (1 - f_L) \sin^2\theta_1 \sin^2\theta_2 \right], \quad (1.10)$$

where f_L is the longitudinal polarization fraction defined as

$$f_L = \frac{\Gamma_L}{\Gamma} = \frac{|A_0|^2}{|A_0|^2 + |A_{+1}|^2 + |A_{-1}|^2}. \quad (1.11)$$

As described in Section 1.6, the hadronic weak decay amplitude involves matrix elements of local four-quark operators, which are too complicated to be calculated on account of final states strong interaction effects. A simple approximation is naive factorization (NF) approach [9], which replaces the matrix element of the four-quark operator with the product of two current matrix elements. For this analysis, it reads

$$\langle \rho^- K^{*+} | (\bar{u}s)(\bar{u}\bar{b}) | B^0 \rangle \rightarrow \langle K^{*+} | (\bar{u}s)_{V-A} | 0 \rangle \langle \rho^- | (\bar{b}u)_{V-A} | B^0 \rangle. \quad (1.12)$$

The matrix element of local four-quark operators factorizes into the product of two current operators: a decay constant f_{K^*} and a $B^0 \rightarrow \rho^-$ transition matrix element. This transition matrix element is described by the invariant $B^0 \rightarrow \rho^-$ form factors from which the helicity amplitudes, A_0 , A_{+1} , and A_{-1} , are determined. They have been mostly calculated in well-defined theoretical models, such as lattice QCD [10], QCD sum rules [11], etc. In this framework, quantitative predictions on decay rates and polarization fractions can be made for $B \rightarrow VV$, taking into account the theoretical and experimental uncertainties in the input parameters. Some of these predictions are summarized in Table 1.1. In general, the longitudinal polarization fraction is predicted to be [8]

$$f_l \propto 1 - \frac{m_{V_1}^2}{m_B^2} = 1 - \frac{m_{K^{*+}}^2}{m_{B^0}^2}. \quad (1.13)$$

It is assumed that the exchange of gluons between the K^{*+} and the $(\rho^- B^0)$ system can be neglected. This approach is justified by the phenomenon of color-transparency [12], in which one expects that a pair of fast-moving quarks $u\bar{s}$ ($E_h \sim m_{B^0}/2$ for two-body decays) in a color-singlet state interact with the medium of gluons not individually but as a single-color dipole, so soft gluons are ineffective in rearranging them. Therefore, long-distance final-state interactions (FSI) can be neglected.

In the semi-classical picture, the fast-moving u and \bar{s} quarks are approximately in parallel and their transverse motion can be neglected. The K^{*+} is in a state with the orbital angular momentum $l=0$, so its spin $J=1$ is due to only the spins of the u and \bar{s} . Taking the K^{*+} moving direction as z direction, the third component satisfies $J_z = s_{1z} + s_{2z}$. The K^{*+} can have three spin states, $\uparrow\uparrow$, $\frac{1}{\sqrt{2}}(\uparrow\downarrow + \downarrow\uparrow)$, $\downarrow\downarrow$, corresponding to $\lambda = +1, 0, -1$, respectively. At the tree level, weak decay with an exchange of W couples only to the right-handed $\bar{s}(h_1 = +\frac{1}{2})$ and the left-handed $u(h_2 = -\frac{1}{2})$. We have $s_{1z} = +\frac{1}{2}$, $s_{2z} = -\frac{1}{2}$, $J_z = s_{1z} + s_{2z} = 0$, and the K^{*+} is in $\lambda=0$ state. The ρ^- , made of the right-handed $\bar{u}(h_1 = +\frac{1}{2})$ and the spectator quark

d with the indefinite helicity ($h_2 = \pm\frac{1}{2}$), can also be in the $\lambda = 0$ state. This argument is also valid for penguin operators with the left-handed u and the right-handed \bar{u} pair. For penguin operators with the right-handed u and the left-handed \bar{u} pair, the K^{*+} is formed with the right-handed $\bar{s}(h_1 = +\frac{1}{2})$ and the right-handed $u(h_2 = +\frac{1}{2})$, we have $s_{1z} = s_{2z} = +\frac{1}{2}$, and $J_z = s_{1z} + s_{2z} = 1$, so the K^{*+} has a helicity of $\lambda = +1$, but the ρ^- , being formed with the left-handed $\bar{u}(h_1 = -\frac{1}{2})$ and the spectator d , can only have $J_z = 0, -1$, corresponding to $\lambda = 0, -1$ states. The overall angular momentum conservation forbids this decay. Therefore the helicities and the overall angular momentum conservations forbid the A_+ and A_- states, and the A_0 is the only dominant state.

To the extent of non-zero quark and meson masses, the $\lambda = \pm 1$ states are allowed by the flip of spin, so the helicities conservation is violated. For the tree operators or the penguin operators with the left-handed u and the right-handed \bar{u} , the $\lambda = +1$ state is achieved by flipping the spin of $u(s_{2z} = -\frac{1}{2})$ in K^{*+} to $s_{2z} = \frac{1}{2}$ with the mass correction of $\mathcal{O}(\frac{p_t}{E}) = \mathcal{O}(\frac{m_{K^{*+}}}{m_{B^0}})$, where p_t is the transverse momentum of quarks inside the K^{*+} , $p_t \approx \frac{1}{2}m_{K^{*+}}$, $E = \frac{m_{B^0}}{2}$, while the spin of quarks in ρ^- , $s_{1z} = +\frac{1}{2}$ for \bar{u} and $s_{2z} = \pm\frac{1}{2}$ for the spectator d , are still good to get $\lambda = +1$ state. To get $\lambda = -1$ state, the spin of \bar{s} in K^{*+} has to flip to $s_{1z} = -\frac{1}{2}$, and the spin of \bar{u} in ρ^- also has to flip to $s_{1z} = -\frac{1}{2}$ with an additional mass correction of $\sim \mathcal{O}(\frac{m_{\rho^-}}{m_{B^0}})$. Furthermore, the $\lambda = +1$ or $\lambda = -1$ states can also be achieved for the penguin operators with the right-handed u and the left-handed \bar{u} by the flip of \bar{u} spin in ρ^- to $s_{1z} = +\frac{1}{2}$ or both \bar{s} and u spins to $-\frac{1}{2}$ in K^{*+} .

In summary, we have

$$A_0 = \mathcal{O}(1), \quad A_{+1} = \mathcal{O}\left(\frac{m_{K^{*+}}}{m_{B^0}}\right), \quad A_{-1} \approx \mathcal{O}\left(\frac{m_{K^{*+}}m_{\rho^-}}{m_{B^0}^2}\right). \quad (1.14)$$

From the definition of the longitudinal polarization fraction in (1.11), we know the decay is longitudinally dominated as naive factorization prediction in (1.13). This has been

experimentally verified in the tree-dominated decay modes, such as $B^+ \rightarrow \rho^+ \rho^0$ and $B^0 \rightarrow \rho^+ \rho^-$. The results from both *BABAR* and Belle collaborations confirmed that the longitudinal polarization fractions are close to 1 (see Table 1.1). However, sizable deviations from the NF prediction are observed in pure penguin modes. For $B \rightarrow \phi K^*$, results from both collaborations show that f_L differs dramatically from the NF counting rule, as low as $f_L = 0.43$. For $B^+ \rightarrow \rho^+ K^{*0}$, the longitudinal polarization fraction is found to be $f_L = 0.50$ from Belle, and $f_L = 0.79$ from *BABAR*. For the penguin dominated mode $B^+ \rightarrow \rho^0 K^{*+}$, the result from *BABAR* still shows the longitudinal polarization dominated with $f_L = 0.96$.

Mode	Prediction		Measurements	
	$\mathcal{B} (\times 10^{-6})$	$f_L (\%)$	$\mathcal{B} (\times 10^{-6})$	$f_L (\%)$
$B^0 \rightarrow \rho^+ \rho^-$	20-25	0.92	$33 \pm 4 \pm 5$ [13]	$0.99 \pm 0.03^{+0.04}_{-0.03}$
$B^+ \rightarrow \rho^0 \rho^+$	7-12	0.92	$22.5^{+5.7}_{-5.4} \pm 5.8$ [14]	$0.97^{+0.03}_{-0.07} \pm 0.04$
$B^+ \rightarrow \rho^0 \rho^+$	7-12	0.92	$31.7 \pm 7.1^{+3.8}_{-6.7}$ [15]	$0.95 \pm 0.01 \pm 0.02$
$B^+ \rightarrow \rho^0 K^{*+}$	6-10	0.90	$10.6^{+3.0}_{-2.6} \pm 2.4$ [14]	$0.96^{+0.04}_{-0.15} \pm 0.04$
$B^+ \rightarrow \rho^+ K^{*0}$	8-12	0.90	$17.0 \pm 2.9 \pm 2.0$ [16]	$0.79 \pm 0.08 \pm 0.04$
$B^+ \rightarrow \rho^+ K^{*0}$	8-12	0.90	$6.6 \pm 2.2 \pm 0.8$ [17]	$0.50 \pm 0.19^{+0.05}_{-0.07}$
$B^0 \rightarrow \rho^- K^{*+}$	6-10	0.90	$< 17.2\% \text{ @ } 90\% \text{ C.L.}$	-
$B^+ \rightarrow \phi K^{*+}$	8-16	0.85	$12.7^{+2.2}_{-2.0} \pm 1.1$ [14]	$0.46 \pm 0.12 \pm 0.03$
$B^0 \rightarrow \phi K^{*0}$	8-15	0.85	$9.2 \pm 0.9 \pm 0.5$ [18]	$0.52 \pm 0.05 \pm 0.02$
$B^0 \rightarrow \phi K^{*0}$	8-15	0.85	$10.0^{+1.6}_{-1.5} {}^{+0.7}_{-0.8}$ [19]	$0.43 \pm 0.09 \pm 0.04$

Table 1.1: Available results on the branching ratio and the polarization fraction f_L measurements for $B \rightarrow VV$ modes.

For pure penguin or penguin dominated modes, the corrections from the penguin annihilation and nonfactorizable contributions must be taken into account [33]. The longitudinal polarization fraction is expected to deviate from the NF counting rules. The decay mode in this analysis receives comparable tree and penguin contributions. Measuring its polarization fraction will help understand corrections from the long distance final state interactions in penguin diagrams.

There is another importance to study penguin dominated decays. Since the penguin

loops involve the heaviest known particles, t quark and W boson, measurements of these processes are sensitive to the new physics beyond the SM with charged Higgs or supersymmetry particles. Though it's hard to claim any new physics with our current understanding of the complicated QCD dynamics, the study of loop processes still constitutes the most efficient low-energy probes for such extensions to the SM.

Chapter 2

The *BABAR* Experiment

2.1 Introduction

The *BABAR* experiment is designed for the systematic study of CP asymmetries in the decays of neutral B mesons to CP eigenstates, which requires fully reconstructing the exclusive final state, tagging the flavor of the decaying particle and measuring the proper time of the B^0 decay with respect to its production, as the asymmetry in most cases cancels to zero in time-integrated measurements of e^+e^- machines. The PEP-II B Factory was designed to deliver the B mesons to the *BABAR* detector, and with its high luminosity, other interesting physics topics also become accessible, such as the precision measurement of the CKM matrix elements, rare B decays, other B physics, the charm and τ lepton physics, and two-photon physics, etc. The analysis presented in this thesis is one of the charmless $B \rightarrow VV$ rare decays, which is important for understanding some QCD evaluations of hadronic matrix elements in the SM by measuring its branching ratio and longitudinal polarization fraction, and for probing the possible involved new physics beyond the SM. As a time-independent analysis, it's not required to separate the decay vertices of two B mesons, but reconstructing the final state of the event with good resolution and high efficiency is very important.

This chapter is a short overview of the experimental facility. The PEP-II B Factory is briefly introduced in Section 2.2 while the *BABAR* detector and its components are summarized in Section 2.3.

2.2 PEP-II Asymmetric B Factory

PEP-II is an asymmetric e^+e^- storage ring system (see Figure 2.1). The e^- and e^+ beams are generated from the SLAC Linac, a 3-km-long linear accelerator, and injected into the two separate rings, the High Energy Ring (HER) ($E_{e^-} = 9.0$ GeV) and the Low Energy Ring (LER) ($E_{e^+} = 3.1$ GeV), which are installed on top of each other in a 2.2 km tunnel. As a result, it operates at a center-of-mass (CM) energy of 10.58 GeV, corresponding to the $\Upsilon(4S)$ resonance mass. The parameters of these energy asymmetric storage rings are presented in Table 2.1 [20]. The different energy of HER and LER also introduces a boost of $\beta\gamma = 0.56$, which is crucial in separating the B decay vertices in order to measure the relative decay time of B mesons, since the $B\bar{B}$ pairs are produced almost at rest in the CM system.

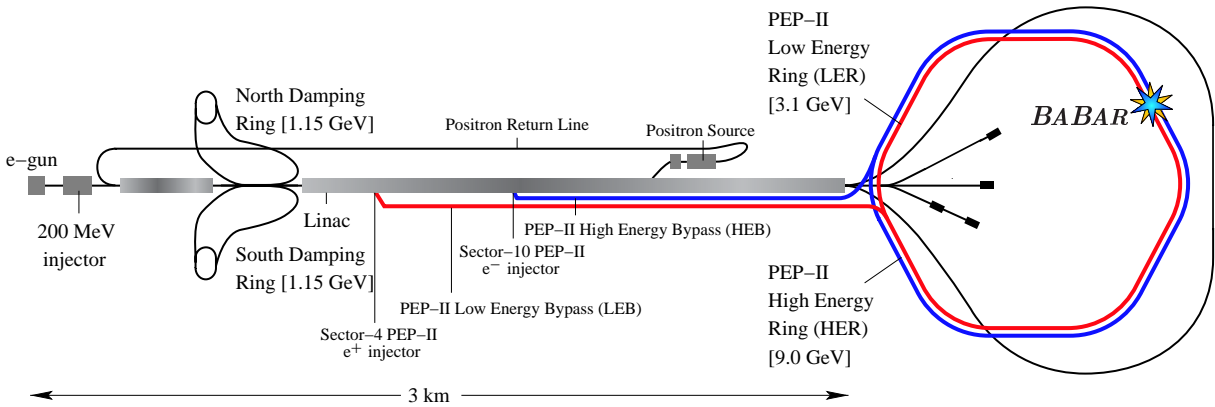


Figure 2.1: *The Linac, PEP-II storage rings and the location of BABAR detector.*

The e^- and e^+ bunches collide head-on in a single Interaction Point (IP) and are separated magnetically in the horizontal plane by a pair of dipole magnets (B1), located at ± 21 cm on

Parameters	Design	Typical
Energy HER/LER (GeV)	9.0/3.1	9.0/3.1
Current HER/LER (A)	0.75/2.15	1.55/2.45
Number of bunches	1658	1588
Bunch spacing (ns)	4.2	6.3-10.5
σ_x (μm)	222	170
σ_y (μm)	6.7	7.2
σ_z (mm)	11	13
Luminosity ($10^{33} \text{ cm}^{-2} \text{ s}^{-1}$)	3	9.21
Luminosity (fb^{-1}/m)	3.3	16

Table 2.1: *PEP-II beam parameters as of June 2004.* σ_x , σ_y and σ_z are the horizontal, vertical and longitudinal r.m.s sizes of the luminous region.

either side of the IP, followed by a series of offset quadrupoles, Q1-Q5 (see Figure 2.2). The Q1 quadrupoles are permanent magnets placed ± 90 cm from the IP, inside the field of the *BABAR* solenoid, while the Q2, Q4 and Q5 quadrupoles are standard iron magnets located outside or in the fringe field of the solenoid. The collision axis is off-set by about 20 mrad from the z -axis of the *BABAR* detector in the horizontal plane to minimize the perturbation of the beams by the solenoidal field [21].

A water-cooled beam pipe encloses the IP region with an outer radius of 27.9 mm. It is composed of two layers of beryllium (0.83 mm and 0.53 mm thick) with a 1.48 mm water channel between them. The inner surface of the pipe is coated with a 4- μm thin layer of gold to attenuate synchrotron radiation. The total thickness of the central beam pipe section at normal incidence is 1.06% of a radiation length. The beam pipe, the permanent magnets, and the SVT were assembled and aligned, and then enclosed in a 4.5-m-long support tube which spans the IP.

In the early running of PEP-II, *BABAR* had to be switched off every 45 to 90 minutes for the new bunches' injection. Since March 11, 2004, a new technique of trickle injection [22] was introduced to allow the *BABAR* detector to keep taking data uninterrupted while the

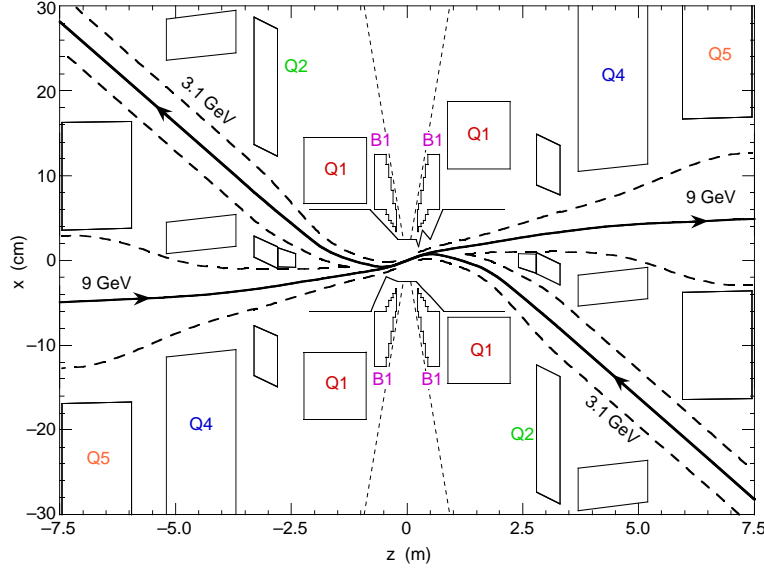


Figure 2.2: A schematic view of the IP region in the horizontal plane of the accelerator. The separation dipoles B1 and focusing quadrupoles Q1-Q5 are shown.

Linac injects e^- and e^+ bunches into the two rings, which increases the production of $B\bar{B}$ by up to 50%.

2.3 The *BABAR* Detector

The *BABAR* detector has been designed to operate optimally on the PEP-II *B* Factory with a forward-backward asymmetric layout along the direction of the beam. The center of the *BABAR* detector is shifted by 0.37 m from the IP, in the boost direction of the more energetic e^- beam to maximize the geometric acceptance, as shown in Figure 2.3.

The layers of *BABAR* sub-detectors are arranged concentrically around the IP in the transverse section. The inner detector consists of a Silicon Vertex Tracker (SVT), a Drift Chamber (DCH), a Detector of Internally Reflected Cherenkov light (DIRC), a CsI Electromagnetic Calorimeter (EMC). These systems are surrounded by a superconducting solenoid with a magnetic field of 1.5 T. The outermost is the Instrumented Flux Return (IFR).

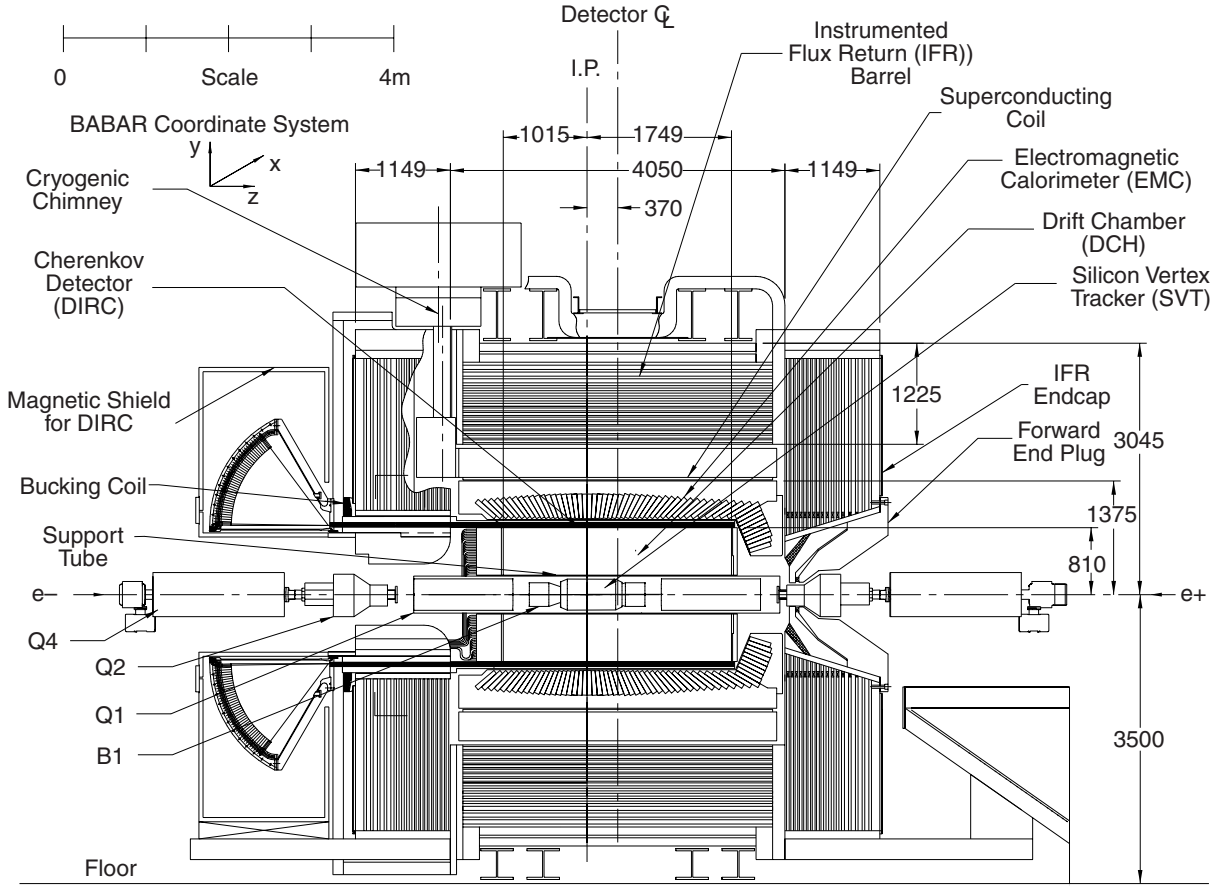


Figure 2.3: *Longitudinal section of the BABAR detector.*

The SVT provides precise position measurement on charged tracks and is the sole tracking device for very low momentum charged particles. The DCH, together with the SVT, provides the main momentum measurement for charged particles and also particle identification (PID) information through energy loss measurements. The DIRC is designed and optimized for high momentum charged particle identification. The EMC detects electromagnetic showers, as well provides good electron identification down to about 0.5 GeV. The IFR provides muon identification down to about 0.6 GeV and neutral hadron identification.

2.3.1 Silicon Vertex Tracker (SVT)

The SVT, as its name explains, is required to provide precision reconstruction of charged particle trajectories and decay vertices near the IP region.

The *BABAR* SVT detector consists of five concentric cylindrical layers of double-sided silicon strip sensors, which are organized in 6, 6, 6, 16 and 18 modules, respectively. The inner three layers are straight while the outer two layers are arch-shaped to minimize the amount of silicon required to cover the solid angle, as shown in Figure 2.4.

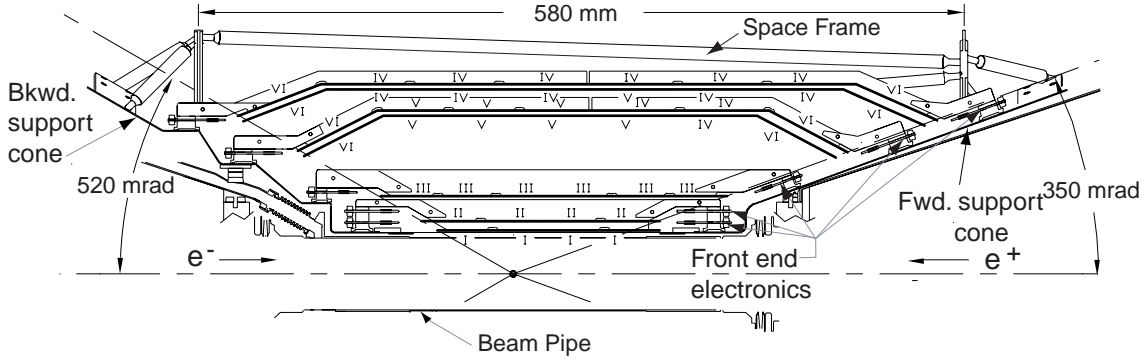


Figure 2.4: *Schematic view of SVT longitudinal section. Six different types of sensors are labelled with the roman numerals.*

The polar angles of the SVT coverage are 20.1° in the forward and -29.8° in the backward. In the CM system, the SVT covers 90% of the solid angle.

The inner three layers are mounted as close to the beam pipe as possible to minimize the impact of multiple scattering in the beam pipe on the extrapolation to the vertex. The modules in these layers are tilted in ϕ by 5° to provide full azimuthal coverage. The outer two layers are placed at much large radii, close to the inner wall of the DCH, to provide the coordinate and angle measurements needed for linking SVT and DCH tracks. Two layers are divided into two sub-layers (4a, 4b, 5a, 5b) and placed at slightly different radii to avoid

gaps in the ϕ coordinate (see Figure 2.5).

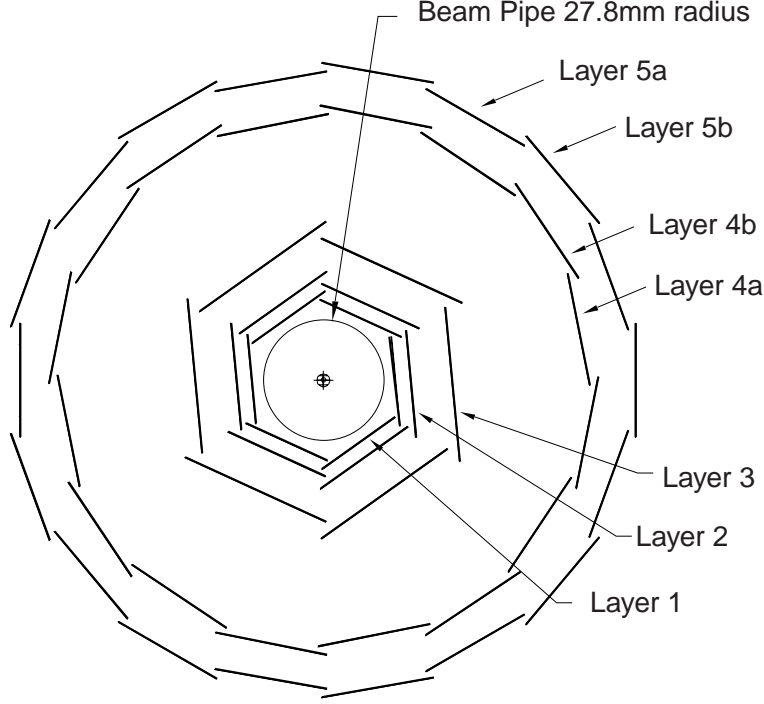


Figure 2.5: *Schematic view of SVT: transverse section.*

The strips on the opposite sides of each sensor are oriented orthogonally to each other with the ϕ measuring strips parallel to the beam and the z measuring strips oriented transversely to the beam axis.

The smallest detectors are $43 \times 42 \text{ mm}^2$ ($z \times \phi$) while the largest are $68 \times 53 \text{ mm}^2$. There are a total of 340 silicon detectors, covering an active area of 0.96 m^2 and the material traversed by particles is $\sim 4\%$ of a radiation length.

The energetic particles passing the sensor create electron-hole pairs and the deposited charges are collected. The sensors are $300 \text{ }\mu\text{m}$ thick double-sided p - n junction diodes at reverse bias, built on high-resistivity ($6\text{-}15 \text{ k}\Omega \text{ cm}$) n -type substrates with p^+ strips and n^+ strips on the two opposite sides. The n^+ strips are insulated with an inter-strip resistance greater than $100 \text{ M}\Omega$ at operating bias voltage. Strips are AC-coupled to the electronics via integrated decoupling capacitance. The energy required to create an electron-hole pair is

3.6 eV, which leads to an ionization yield for minimum ionizing particles of ~ 22000 electrons in the sensor.

The SVT dominates the position measurements near the IP. The charged tracks are fitted with parameters measured at the point of closest approach to the z -axis. The distances of this point from the origin of the coordinate system are taken as d_0 in the x - y plane and z_0 along the z -axis. The typical resolution is $\sigma_{d_0} = 55 \mu\text{m}$ and $\sigma_{z_0} = 65 \mu\text{m}$.

2.3.2 Drift Chamber (DCH)

As the main tracking system in *BABAR*, the DCH is designed for the efficient detection of charged particles and the precise measurement of their momenta and angles. The DCH complements the measurements of the impact parameter and the directions of charged tracks provided by the SVT near the IP. The reconstruction of decay and interaction vertices outside of the SVT volume, for instance some of K_s^0 decays, relies solely on the DCH. The DCH is also required to provide particle identification for low momentum charged particles by measuring ionization loss (dE/dx).

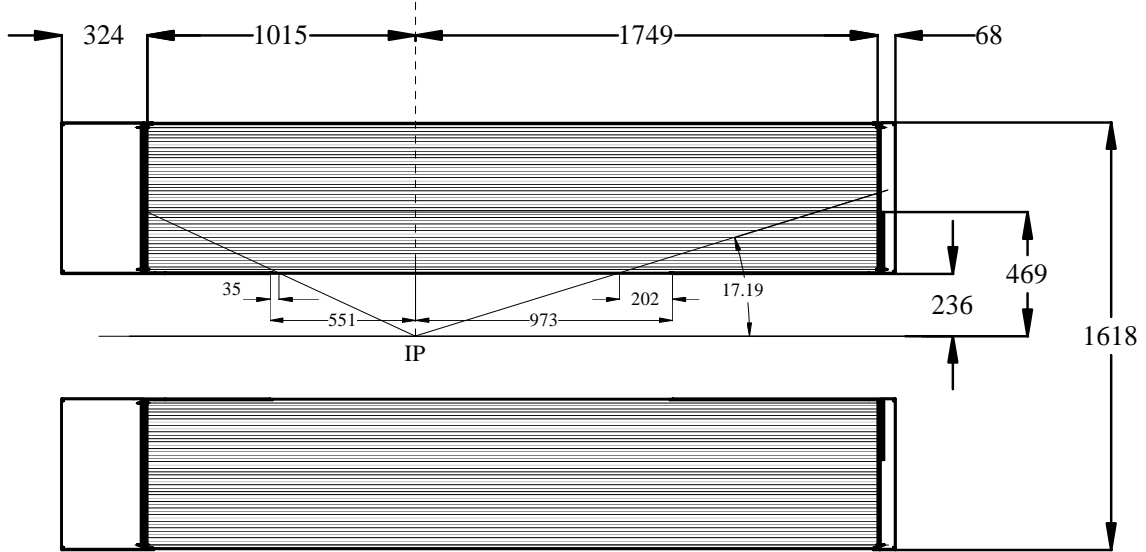


Figure 2.6: *Longitudinal section of the DCH with principal dimensions.*

The *BABAR* DCH is a 280-cm-long cylinder, with an inner radius of 23.6 cm and an outer radius of 80.9 cm, as shown in Figure 2.6. Its center is shifted by 37 cm with respect to the IP for large coverage in the forward. The forward length (1749 mm) and the backward length (1015 mm) allow the particles emitted at polar angle from 17.2° to 152.6° to traverse at least half of the layers.

There are a total of 7104 drift cells, arranged in 40 cylindrical layers, providing up to 40 spatial and ionization loss measurements for charged particles with transverse momentum greater than 180 MeV/ c . The 40 layers are grouped by four into ten superlayers, with the same wire orientation and equal numbers of cells in each layer of a superlayer. The stereo angles of the superlayers alternate between axial (A) and stereo (U,V) pairs, in the order AUVAUVAUVA, as shown in Figure 2.7. The stereo wires are placed at small angles (between ± 45 and ± 76 mrad) with respect to the z -axis, from which longitudinal position information is obtained.

Each cell consists of one sense wire surrounded by six field wires with a shape of hexagonal (see Figure 2.7). The sense wires are applied a positive high voltage and the field wires are at ground potential. The charged particles passing the chamber deposit energy by ionizing the gas medium and produce electrons, which drift to a sense wire. The accelerating gradient of field causes an avalanche of secondary ionization in the process of electrons drifting, and thus amplifies the signal received by the sense wire. The chamber is filled with a 80:20 helium-isobutane gas mixture. The noble gas helium is used as the ionization medium and the isobutane functions as the quenching gas which absorbs the photons released by excited atoms to keep the avalanche localized and avoid chamber breakdown. This gas mixture has a relative larger radiation length, and holds the multiple scattering inside the DCH to a minimum, less than 0.2% of the radiation length of the material, together with the employment of the low-mass aluminum field wires.

The data from both tracking systems, the SVT and the DCH, are combined for the re-

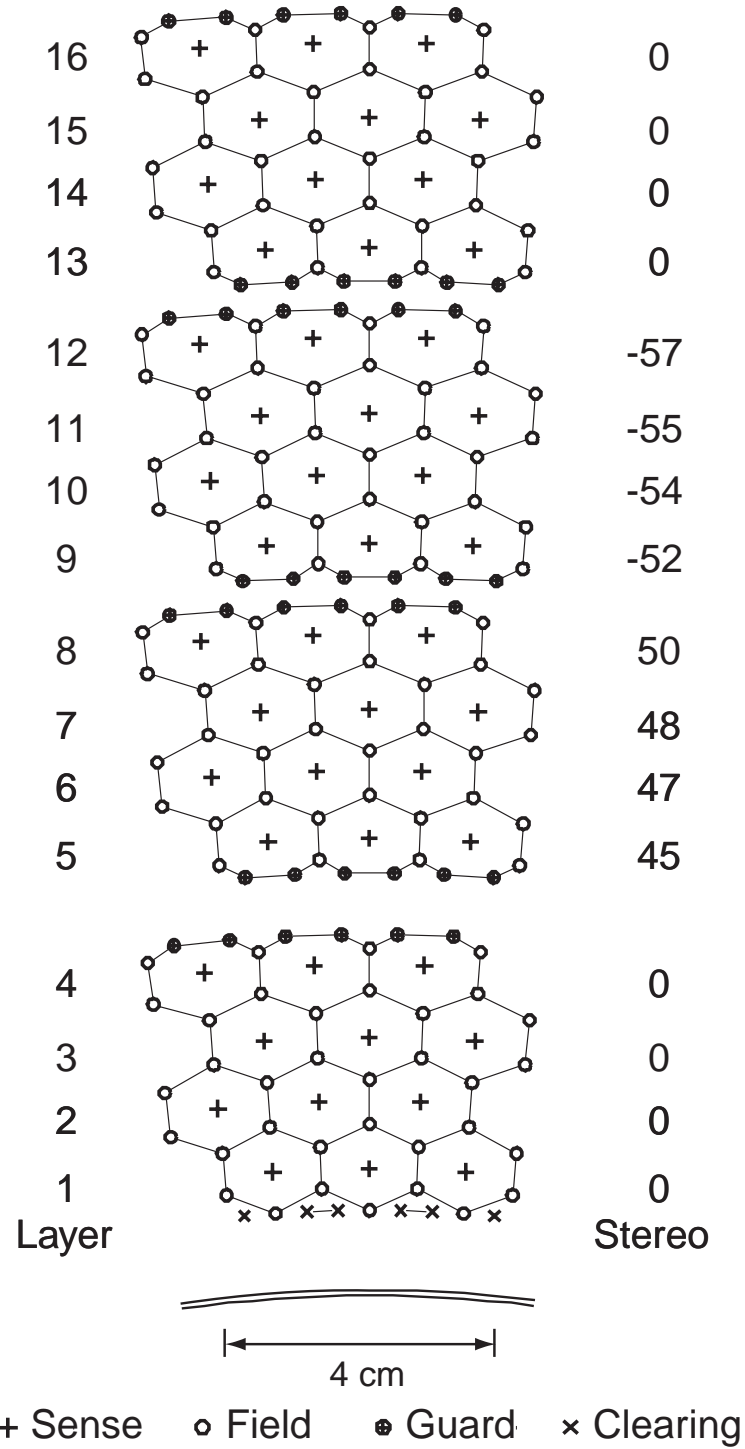


Figure 2.7: Schematic layout of drift cells for the four innermost superlayers. Lines are added to make the cell boundaries clear. The numbers on the right side show the stereo angle (in mrad) of sense wires in each layer.

construction of charged particle tracks. While the SVT measurements dominate the position and angle measurements near the IP, the DCH contributes primarily to the p_T measurement.

The resolution of measured p_T , σ_{p_T}/p_T , is a function of p_T (GeV/c)

$$\sigma_{p_T}/p_T = (0.13 \pm 0.01)\% \cdot p_T + (0.45 \pm 0.03)\%. \quad (2.1)$$

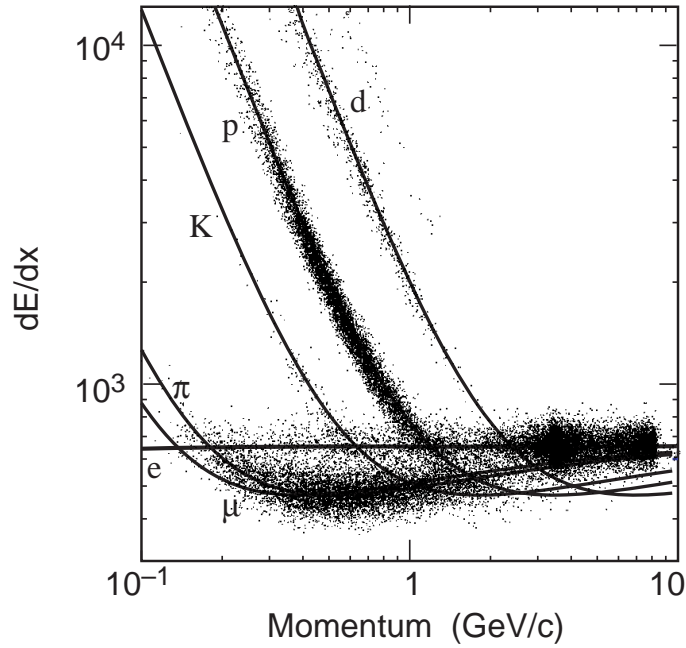


Figure 2.8: *Corrected measurement of dE/dx in the DCH as a function of track momenta. Data samples are from beam background triggers. The curves show the Bethe-Bloch predictions derived from selected control samples of particles of different masses.*

Figure 2.8 shows the distribution of the corrected dE/dx measurements as a function of track momenta. The superimposed Bethe-Bloch predictions for particles of different masses have been determined from selected control samples. A resolution of about 7% in dE/dx allows π/K separation up to 700 MeV/c. This capability is complementary to that of the DIRC in the barrel region, while in the extreme backward and forward directions without the DIRC coverage, the DCH is the only device for particle identification.

2.3.3 Detector of Internally Reflected Cherenkov light (DIRC)

BABAR uses a ring-imaging Cherenkov detector called the Detector of Internally Reflected Cherenkov light (DIRC) to meet the requirement of the particle identification in a wide momentum range, in a small radial dimension and with high tolerance of backgrounds.

The Cherenkov lights are generated by a charged particle whose velocity is greater than the local phase velocity of light. The half-angle of the Cherenkov cone for a charged particle with velocity βc in a medium with index of refraction n is determined by $\cos\theta_c = \frac{1}{n\beta}$. The DIRC is based on the principle that the magnitudes of angles are maintained upon reflection from a flat surface. A schematic of the DIRC geometry shown in Figure 2.9 illustrates the principles of light production, transport and imaging.

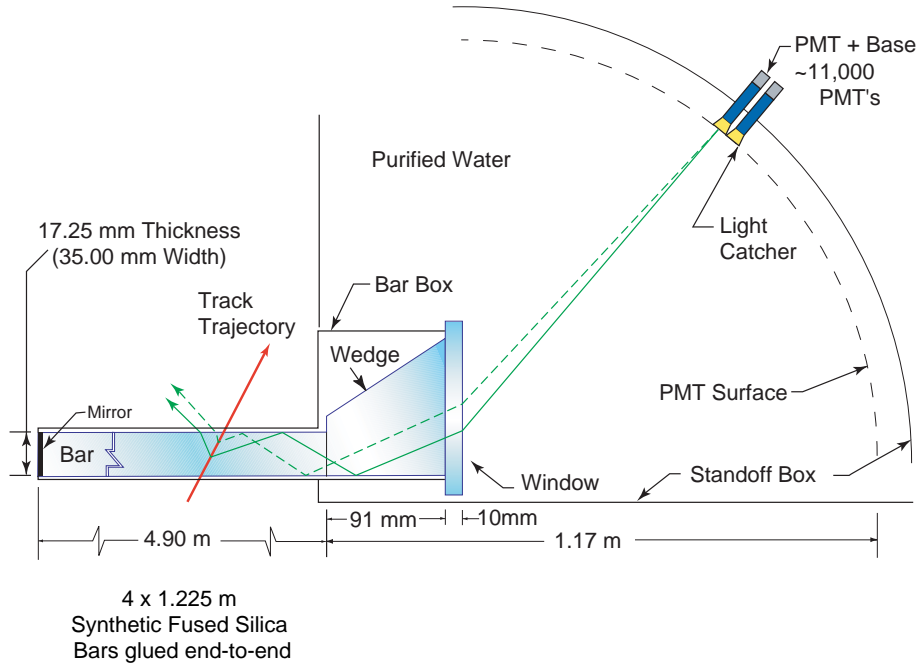


Figure 2.9: *Schematics of the DIRC fused silica radiator bar and imaging region.*

The DIRC consists of 144 long straight bars of synthetic, fused silica ($n=1.473$) with rectangular cross-section, serving both as radiators and as light pipes for the portion of the light trapped in the radiator by total internal reflection [23].

The bars are arranged in a 12-sided polygonal barrel (see Figure 2.10), and placed into 12 hermetically sealed containers, called *bar boxes*, made of very thin aluminum-hexcel panels. Each bar is 17-mm-thick, 35-mm-wide, and 4.9-m-long, assembled from four 1.225 m pieces that are glued end-to-end and has a fused silica wedge glued to it at the readout end. The 12 wedges in a bar box are glued to a common 10-mm-thick fused silica window, that provides the interface and seal to the 6000 litres of purified water filled in the standoff box. The low-cost water with an average index of refraction reasonably close to that of fused silica is used to minimize the total internal reflection at the silica-water interface.

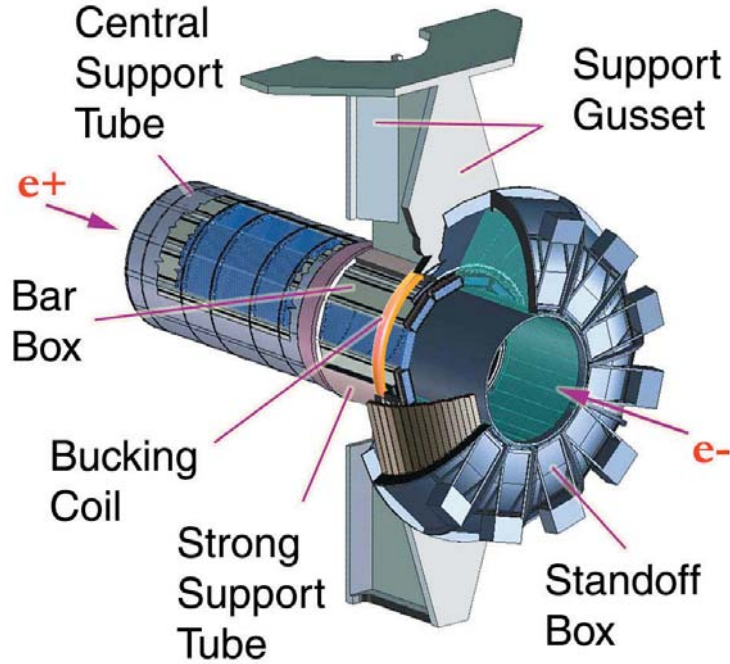


Figure 2.10: *Exploded view of the DIRC mechanical support structure.*

For particles with $\beta \approx 1$, some photons will always lie within the total internal reflection limit, and will be transported to either one or both ends of the bar, depending on the particle incident angle. The DIRC photon detector is placed at the backward end to minimize interference with other detector systems in the forward region, since the asymmetric beam

energy causes particles produced preferentially forward in the detector. At the forward end, a mirror is placed perpendicular to the bar axis to reflect incident photons to the backward, instrumented end. Once photons arrive at the instrumented end, most of them emerge into standoff box. The wedge at the exit of the bar reflects photons at large angles relative to the bar axis. It thereby reduces the size of the required detection surface and recovers those photons that would otherwise be lost due to internal reflection at the fused silica water interface. The photons are detected by 12 sectors of photomultiplier tubes (PMTs) lying on a surface at the rear of the standoff box, about 1.2 m from the bar end. Each of the 12 PMT sectors contains 896 PMTs, in a densely packed array inside the water volume.

The emission angle and the arrival time of the Cherenkov photons are reconstructed from the observed space-time coordinates of the PMT signals, transformed into the Cherenkov coordinate system, θ_c , the Cherenkov angle, ϕ_c , the azimuthal angle of a Cherenkov photon around the track direction, and δt , the difference between the measured and expected photon arrival time. With the measured Cherenkov angle, the charged particle's velocity is calculated. Combined with the momentum measurement by the tracking system, the particle's type is determined. An unbinned maximum likelihood formalism is used to provide a likelihood value for each of the five stable charged particle types (e , μ , π , K , p) if the track passes through the active volume of the DIRC. The expected π/K separation at 3 GeV/ c is about 4.2σ .

2.3.4 Electromagnetic Calorimeter (EMC)

To satisfy the requirements of measuring electromagnetic showers with excellent efficiency, and energy and angular resolutions over the energy range from 20 MeV to 9 GeV, the *BABAR* EMC uses a homogeneous calorimeter. It is composed of a finely segmented array of thallium-doped caesium iodide (CsI(Tl)) crystals. It covers full azimuth and from 15.8° to

141.8° in polar angle with a cylindrical barrel of 5760 crystals arranged in 48 distinct rings and a conical forward endcap of 820 crystals arranged in eight rings, as shown in Figure 2.11.

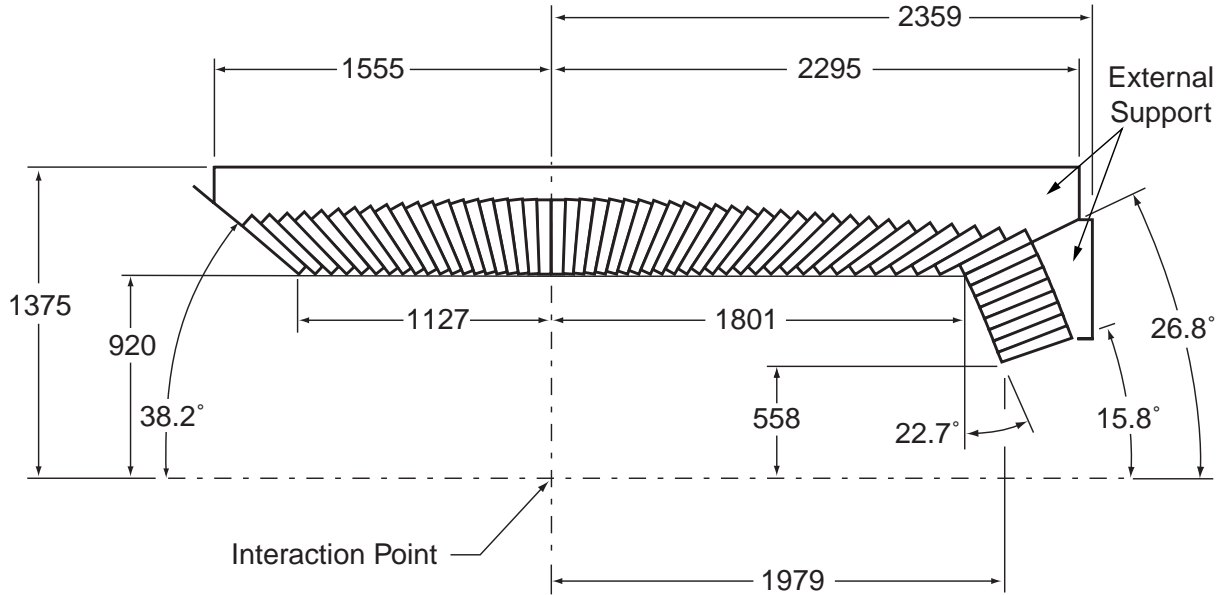


Figure 2.11: A longitudinal cross section of the EMC (only the top half is shown) indicating the arrangement of the 56 crystal rings. The detector is axially symmetric around the z -axis. All dimensions are given in mm.

The crystals have a tapered trapezoidal cross section with the length increasing from 29.6 cm in the backward to 32.4 cm in the forward direction to limit the effects of shower leakage from increasingly higher energy particles.

The crystals doped with 0.1% thallium have several properties. The high light yield and small Moliere radius [24] allow for excellent energy and angular resolutions, while the short radiation length allows for shower containment at *BABAR* energies with a relatively compact design. The high light yield and the emission spectrum also permit efficient use of silicon photodiodes which operate well in high magnetic fields.

Electromagnetic shower usually spreads over many adjacent crystals, which are grouped into two types of clusters: single clusters with one energy maximum and merged clusters with more than one local energy maximum (*bumps*). The measured energy is corrected for

shower leakage and particle pre-shower before entering the EMC.

The energy resolution is dependent of energy, a fit using various processes gives

$$\frac{\sigma_E}{E} = \frac{(2.32 \pm 0.30)\%}{\sqrt[4]{E(\text{GeV})}} \otimes (1.85 \pm 0.12)\%. \quad (2.2)$$

Typically, it is measured as $\sigma_E/E = (5.0 \pm 0.8)\%$ at low energy (6.13 MeV) with the radioactive source and $\sigma_E/E = (1.9 \pm 0.07)\%$ at high energy (7.5 GeV) with Bhabha scattering.

The angular resolution is also energy-dependent and can be parameterized as

$$\sigma_\theta = \sigma_\phi = \left(\frac{3.87 \pm 0.07}{\sqrt{E(\text{GeV})}} + 0.00 \pm 0.04 \right) \text{ mrad} \quad (2.3)$$

Electrons are separated from charged hadron primarily on the basis of the shower energy, lateral moments, and track momentum. The most important variable is the ratio of the shower energy to the track momentum (E/p), which is much larger for electrons than hadrons.

2.3.5 Instrumental Flux Return (IFR)

The penetrative muons and neutral hadrons are detected by the IFR. For muons, good efficiency and high background rejection are required, while for neutral hadrons, high efficiency and good angular resolution are most important. Both need a large solid angle coverage.

The *BABAR* IFR uses the steel flux return of the magnet as a muon filter and hadron absorber. The resistive plate chambers (RPCs) with two coordinates readout are installed in the gaps of the finely segmented steel of the barrel and the end doors of the flux return, as shown in Figure 2.12. There are 19 RPC layers in the barrel and 18 in the endcaps. In addition, two layers of cylindrical RPCs are installed between the EMC and the magnet solenoid to detect particles exiting the EMC.

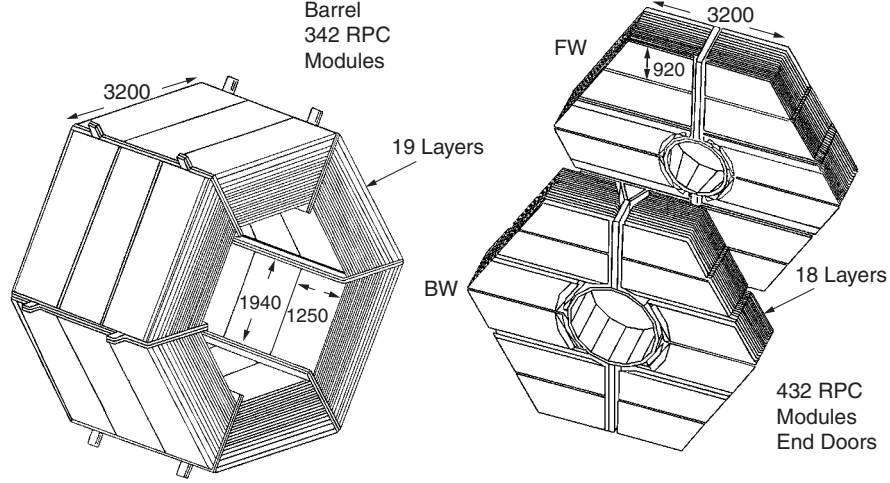


Figure 2.12: *Overview of the IFR: Barrel sectors and forward and backward end doors; the shape of the RPC modules and their dimensions are indicated.*

The IFR detectors cover an active area of about 2000 m^2 with a total of 806 RPC modules, 57 in each of the six barrel sectors, 108 in each of the four half end doors, and 32 in the two cylindrical layers. The maximum size of the material available is $320 \times 130 \text{ cm}^2$, which limits the size of a module. Two or three RPC modules are joined to form a gap-size chamber. More than 25 different shapes and sizes of modules are built to match to the steel dimensions with very little dead space. The modules of each chamber are connected to the gas system (56.7% argon, 38.8% freon, and 4.5% isobutane) in series, while the high voltage ($\sim 8 \text{ kV}$) is supplied separately to each module.

In the barrel sectors, the gaps between the steel plates extend 375 cm in the z direction and three modules are needed to cover the whole area of the gap. Each barrel module measures the z coordinate with 32 strips running perpendicular to the beam axis and ϕ with 96 strips in the orthogonal direction.

Each of the four half end doors is divided into three sections. Each section is covered by two RPC modules that are joined to form a larger chamber with horizontal and vertical readout strips.

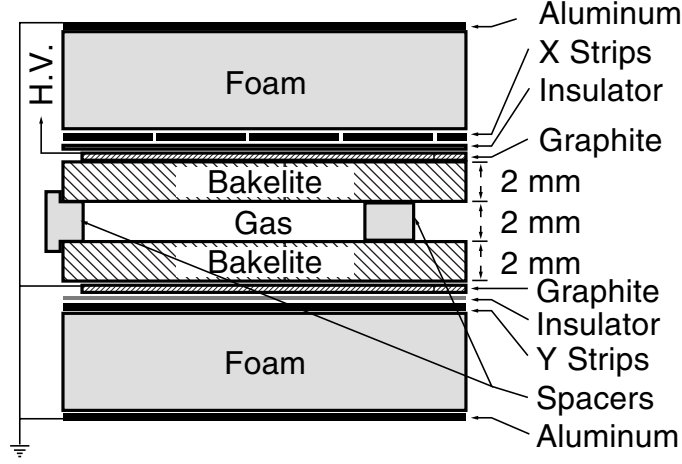


Figure 2.13: *Cross section view of a planar RPC. The high voltage (H.V.) connection is schematically shown.*

Figure 2.13 shows the cross section of an RPC. Energetic particles passing through the modules ionize gas inside, producing electrons and positive ions. These electrons traversing the RPC gap in a high electric field cause further ionizations, which are so large that the charge accumulated distorts the electric field, eventually discharges the gas and creates limited streamers between the bakelite plates. The signals are readout capacitively by strip electrodes.

Combined with other detector systems inside, the IFR provides a muon detection efficiency of close to 90% in the momentum range of $1.5 < p < 3.0$ GeV/ c with a fake rate of about 6 – 8% for pions. The neutral hadron are identified as clusters that are not associated with a charged track.

2.3.6 Trigger System

High luminosity requires the trigger system selecting events of interest with a high, stable, and well-understood efficiency of over 99% for all $B\bar{B}$ events and at least 95% for continuum

events, while rejecting beam-induced background events to keep the total event rate under 200 Hz.

The *BABAR* trigger is implemented as a two-level hierarchy, the Level 1 (L1) in hardware followed by the Level 3 (L3) in software.

The L1 trigger decision is based on charged tracks in the DCH above a preset transverse momentum, showers in the EMC, and tracks detected in the IFR, which are usually absent in beam-induced backgrounds. The trigger data are processed by three specialized corresponding hardware processors. The drift chamber trigger (DCT) and electromagnetic trigger (EMT) both satisfy all trigger requirements independently with high efficiency, and thereby provide a high degree of redundancy, which enables the measurement of trigger efficiency. The instrumented flux return trigger (IFT) is used for triggering $\mu^+\mu^-$ and cosmic rays, mostly for diagnostic purposes. Each of the three processors generates trigger *primitives*, summary data on the position and energy of particles, that are sent to the global trigger (GLT) every 134 ns. The GLT processes all trigger primitives to form specific trigger and then delivers them to the *Fast Control and Timing System* (FCTS). If a valid trigger remains, an *L1 Accept* is issued to initiate event readout. The trigger definition logic, masks, and prescale values are all configurable on a per run basis.

The L3 receives the output from the L1, performs a second stage rate reduction for the main physics sources, and identifies and flags the special categories of events needed for luminosity determination, diagnostic and calibration purposes. The L3 trigger software comprises event reconstruction and classification, a set of event selection filters, and monitoring. The filters have access to the complete event data for making their decision, including the output of the L1 trigger processors and the FCTS trigger scalars. The L3 operates by refining and augmenting the selection methods used in the L1 and consists of three phases. First, events are classified by defining L3 input lines, which are based on a logical OR of any number of the FCTS output lines. Then a number of scripts are executed independently. Each script

produces a single pass-fail output flag if its single L3 input line is true. Finally, taking the logical OR of selected script flags, the L3 output lines are formed to complete the trigger process.

2.3.7 Online System

The *BABAR* online system controls and coordinates the processes of data acquisition (DAQ). As shown schematically in Figure 2.14, it consists of detector, DAQ system, DAQ control and monitoring systems, data quality control and online calibration systems. From the point of view of software, it includes the following components: Online Dataflow (ODF) controls and communicates with the Front End Electronics (FEEs) to acquire event data; Online Event Processing (OEP) processes complete events, including L3 triggering, data quality monitoring and final stages of calibrations; Logging Manager (LM) receives events from OEP and writes them to disk as input to the Online Prompt Reconstruction (OPR) precessing; Online Detector Control (ODC) controls and monitors environmental conditions of the detector systems; OPR reconstructs and selects full event and collects monitoring data for quality control; Online Run Control (ORC) ties together all the other components, sequences their operations and provides a Graphical User Interface (GUI) for operator control.

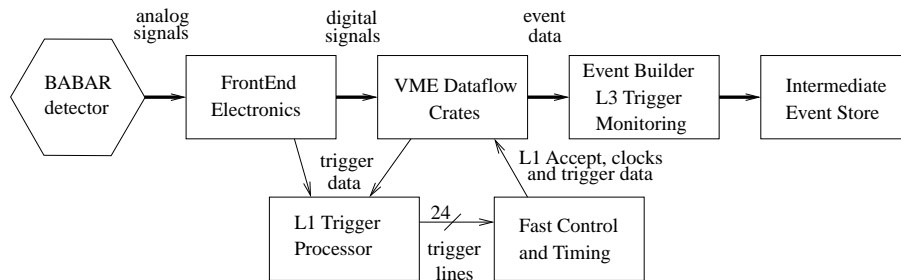


Figure 2.14: *Schematic diagram of the BABAR online system.*

The *BABAR* online system is capable of supporting an average event size of 32 kbytes, at ~ 2500 Hz L1 trigger rate and reducing this rate in L3 to the required 200 Hz limit.

Chapter 3

Analysis Approach

This chapter contains the detailed description of this analysis. The event samples are listed in Section 3.1 for data collected with the *BABAR* detector. Section 3.2 describes briefly the *BABAR* Monte Carlo (MC) simulation technique. Section 3.3 shows how the final state candidates are reconstructed. We extract the number of $B^0 \rightarrow \rho^- K^{*+}$ events and the longitudinal polarization fraction using a Maximum Likelihood (ML) fit, which is given in Section 3.4. Various fit tests are done in Section 3.5 and Section 3.6. The results and goodness of fit are demonstrated in Section 3.7. Section 3.8 discusses various systematic uncertainties contributing to this measurement. Finally, a summary and conclusion are given in Section 3.9.

This study used a blind analysis technique [25]. In the blinding stage, selection cuts are optimized, background contributions are estimated, and analysis procedures are determined. Any problems observed will be rectified and fit validation and stability checks are done. Only when the analysis is essentially finalized is the signal box opened, and the result unblinded for an observation or an upper limit.

Blind analysis is the optimal way to reduce or eliminate the risk of any experimenter's bias which could occur if the event selection is determined with prior knowledge of the effect of that selection on the data, eg., the selection cuts can be tuned to remove a few

extra background-like events or to improve the statistical significance of a small signal. It is obvious the value of a measurement does not contain any information about its correctness, knowledge of its value is of no use in performing the analysis itself.

For this analysis, the signal yield and the longitudinal polarization fraction are blinded.

3.1 Data Sets

The results presented in this thesis are based on data collected between 1999 and 2003 with the *BABAR* detector. There are a total integrated luminosity of 112.5 fb^{-1} onpeak data, corresponding to $122.7 \times 10^6 \text{ } B\bar{B}$ pairs, and 12.0 fb^{-1} offpeak data, taken 40 MeV below $\Upsilon(4S)$ resonance. The detailed data samples are listed in Table 3.1.

Run(Year)	Onpeak(fb^{-1})	Offpeak(fb^{-1})
Run-1(1999)	0.5	0.0
Run-1(2000)	20.1	2.6
Run-2(2001)	35.4	3.8
Run-2(2002)	25.39	3.22
Run-3(2002)	0.87	0.0
Run-3(2003)	30.28	2.39

Table 3.1: *The data samples*

3.2 Monte Carlo (MC) Simulation

We use MC simulated events for the studies of events properties, optimization of selection criteria and fit validation checks in the blinding analysis stage. In *BABAR* it consists of the following steps:

- Physics events generation: The physics of the e^+e^- collision is performed by one of

several event generators which simulate the different physics events according to different theory models. The particle types, momenta, angular distributions, etc. are determined for decay products. The most commonly used generators are EvtGen [26] for simulating exclusive physics processes in decays of B mesons and other resonances, and Jetset [27] for other inclusive B decays and continuum $q\bar{q}$ events.

- Particle transportation and interaction: The final particles produced in the generation step are propagated through the *BABAR* detector using the GEANT4 [28] package, which builds a virtual *BABAR* detector and simulates the particles' transportation and interaction with the materials of each detector component, then produces an output of idealized energy deposited and the corresponding locations, stored in a data structure called **GHits**.
- Smearing and digitization: The idealized **GHits** data are smeared and digitized into signals which look like the actual data collected by the *BABAR* detector electronics. Backgrounds are also overlaid to make the final output comparable to the data.
- Reconstruction: The raw simulation will be reconstructed in the same way as the data for physics analysis use. The output is various candidate lists of tracks and clusters, with the same format as data except with MC event truth information which is helpful for user to trace the original event production and physics decay chains.

Besides the exclusive signal MC events, which are used to study selection criteria, efficiencies and signal distributions, $B\bar{B}$ generic events (192.9×10^6 for the generic $B^0\bar{B}^0$ and 192.7×10^6 for the generic B^+B^-) are used to estimate the dominant neutral and charged charm B backgrounds. We also use around 180 exclusive charmless B decay modes to study the possible charmless B backgrounds contribution. A complete list of MC modes used in this analysis is given in Tables A.1-A.6 in Appendix A.

The differences between MC and data due to imperfect simulation of MC events have been corrected for tracking efficiencies, shower leakage and neutral energy resolution and particle identification. These effects are assigned as systematic uncertainties (see Section 3.8).

3.3 Event Reconstruction

B mesons decay dominantly through the Cabbibo favored $b \rightarrow c$ transition, while the charmless B decay involving $b \rightarrow u$ transition is suppressed by the $|V_{ub}/V_{cb}|^2$. The typical branching fraction of charmless B -decays is of the order 10^{-6} . In addition, since the cross section for light quark productions $e^+e^- \rightarrow q\bar{q}$ is almost three times that of $b\bar{b}$ at the $\Upsilon(4S)$, the continuum background needs to be suppressed by roughly a factor of 10^6 in order to study charmless B decays. This requires both B -decay kinematics and event shape differences in different decays to be fully exploited.

We reconstruct our signal $B^0 \rightarrow \rho^- K^{*+}$ with decay chains of $K^{*+} \rightarrow K^+ \pi^0$, $\rho^- \rightarrow \pi^- \pi^0$ and $\pi^0 \rightarrow \gamma\gamma$. The final state consists of two tracks with different charges and two π^0 's. For mainly practical reasons, the event reconstruction is performed in two stages: pre-selection and final event candidate selection.

3.3.1 Discriminating Variables

The most commonly used variables to separate B decays from continuum backgrounds are related to B kinematics.

The variable m_{ES} is the beam-energy-substituted mass, defined as

$$m_{\text{ES}} \equiv \sqrt{(s/2 + \mathbf{p}_0 \cdot \mathbf{p}_B)^2/E_0^2 - |\mathbf{p}_B|^2}, \quad (3.1)$$

where s is the squared CM energy, \mathbf{p} and E are the momentum and energy in the lab frame,

the subscripts 0 and B refer to the $\Upsilon(4S)$ and the B candidate, respectively. The calculation only involves quantities measured in the laboratory frame, thus the distribution of m_{ES} is independent of the particle hypothesis of the tracks reconstructed in the final states. The m_{ES} distribution for real B candidates is expected to peak at its mass central value, 5.279 GeV/ c^2 . The typical resolution of m_{ES} for fully reconstructed B decay is about 2.5 MeV/ c^2 , mainly limited by our knowledge of the e^+e^- beam energy and direction. For continuum background, the distribution is parametrized empirically by the Argus function [30]

$$P_{\text{Argus}}(m_{\text{ES}}; E_{\text{beam}}, \xi) = Ax\sqrt{1-x^2}e^{\xi(1-x^2)}, \quad (3.2)$$

where $x = m_{\text{ES}}/E_{\text{beam}}$, ξ is the Argus exponent, controlling the slope of the shape and A is a normalization factor.

The ΔE is the difference between the energy of the reconstructed B meson and the expected energy of the B meson, defined as

$$\Delta E \equiv E_B^* - E_{\text{CM}}/2 = (E_0 E_B - \mathbf{p}_0 \cdot \mathbf{p}_B - s/2)/\sqrt{s}, \quad (3.3)$$

where E_B^* is the energy of the reconstructed B meson in the CM frame. Its distribution is expected to be centered at zero for real B candidates. The resolution of ΔE varies dramatically depending on how many particles in the final states as well as the type of particles. Normally, the ΔE resolution is much worse if there is one or multiple π^0 s in the final state compared with final states involving only charged tracks.

To exploit the information from the intermediate resonances of B^0 decay, the invariant mass and helicity of vector mesons are very important to distinguish signals from backgrounds. The vector meson's mass is calculated by combining the charged $\pi^-(K^+)$ track with π^0 for $\rho^-(K^{*+})$ meson. The helicity angle of vector meson $\rho^-(K^{*+})$ is defined as the an-

gle between the direction of the charged $\pi^-(K^+)$ track and the parent B^0 candidate direction in the $\rho^-(K^{*+})$ rest frame.

3.3.2 Events Pre-selection

The pre-selection is designed to screen out apparently unrelated background events while keeping signal efficiencies as high as possible. It loops over all the combinations of charged tracks and neutral candidates with the following requirements:

- Charged tracks are selected with the requirements of

1. charge $\neq 0$ and π mass hypothesis;
2. transverse momentum $p_T < 10 \text{ GeV}/c$;
3. $DOCA_{xy} < 1.5 \text{ cm}$;
4. $DOCA_z < 10 \text{ cm}$;

where DOCA is the distance of closest approach to the vertex from track fitting in x - y plane ($DOCA_{xy}$) and z direction ($DOCA_z$).

- Neutral candidates are selected with the requirements of

1. photon energy $E_\gamma > 30 \text{ MeV}$;
2. photon lateral moment [29] $LAT < 0.8$;
3. π^0 energy $E_{\pi^0} > 200 \text{ MeV}$;
4. π^0 mass $115 < M_{\pi^0} < 150 \text{ MeV}/c^2$;

- $|m_{\text{ES}} - \sqrt{s}/2| < 0.1 \text{ GeV}/c^2$;

- $\Delta E < 0.3 \text{ GeV}$;

- at least one track in the rest of the event;
- 3σ mass window selection on the invariant mass of the charged track with $\pi^-(K^+)$ hypothesis and π^0 combination for $\rho^-(K^{*+})$ meson;

where σ denotes the resonance width, $150 \text{ MeV}/c^2$ for ρ^- and $50 \text{ MeV}/c^2$ for K^{*+} .

The event is accepted if at least one B -candidate passes the above selections.

3.3.3 Candidate Selection

To further improve the signal to background ratio, candidates passing the pre-selection must satisfy the following additional requirements:

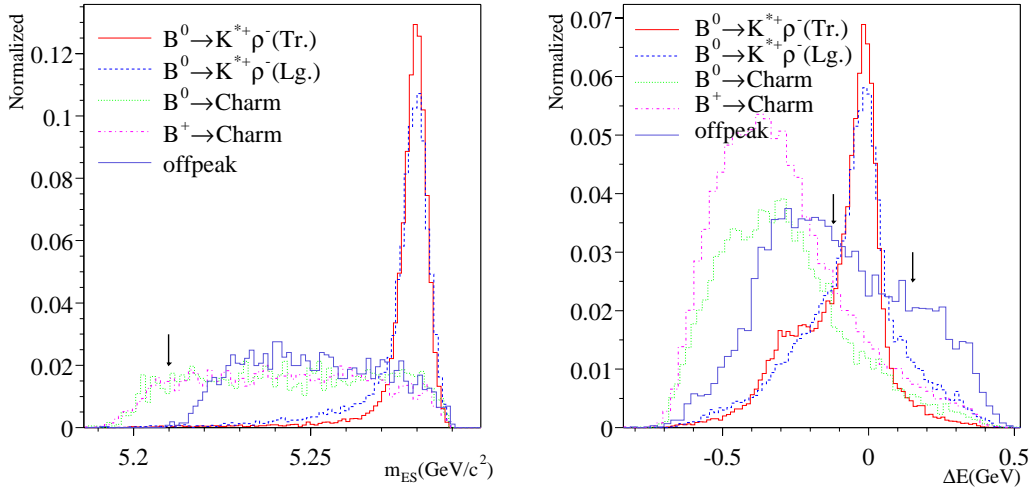


Figure 3.1: *Distributions of m_{ES} (left) and ΔE (right) for signal MC, $b \rightarrow c$ backgrounds MC and offpeak data. The arrows indicate the requirements applied.*

- $5.21 < m_{ES} < 5.29 \text{ GeV}/c^2$, this provides a reasonable fit range for continuum and signal events (see left hand in Figure 3.1);
- $-0.12 < \Delta E < 0.15 \text{ GeV}$, this cut is asymmetric about 0 in order to remove $b \rightarrow c$ backgrounds which rise at negative ΔE (see right hand in Figure 3.1);

- $0.01 < LAT_\gamma < 0.6$ and $E_\gamma > 50$ MeV for two photons from π^0 ;
- Particle identifications are applied to the charged track candidates. The K^+ candidate is selected based on a likelihood function using information from SVT, DCH, and DIRC for different momentum ranges. The π^- candidate is selected by actually vetoing other charged particles. Protons are identified with a likelihood-based selector, similar to kaon selection. Electrons are identified primarily using the shower energy and lateral moments. The π^- is required to fail the electron, proton, and kaon selections. Since muon selection has very high π misidentification rates of about 6-8% and combinatorial backgrounds from muon is very low, no veto on muon is required to keep the high selection efficiency.
- The cuts on the invariant mass of resonance mesons are tightened within 2.5σ as $|m(\pi^-\pi^0) - 0.771| < 0.375$ GeV/ c^2 for ρ^- and $|m(K^+\pi^0) - 0.892| < 0.125$ GeV/ c^2 for K^{*+} (see Figure 3.2);
- The helicity angles of vector mesons are required to satisfy $-0.8 < \cos(\theta_H) < 0.98$ for both ρ^- and K^{*+} mesons to highly suppress B backgrounds which rises sharply at below -0.8 (see Figure 3.3).

3.3.4 Multiple Candidate and Signal Misreconstruction

Some of the events passing the selections have multiple candidates, which occur in both backgrounds and signal events due to combinatorics. Table 3.2 lists the average number of candidates per event for signal MC, onpeak and offpeak data. Approximately 26% of longitudinal and 17% of transverse signal events have more than one candidate.

In the analysis, events with more than one candidate will be counted only once. We select the best candidate using a quantity calculated from both reconstructed π^0 masses relative

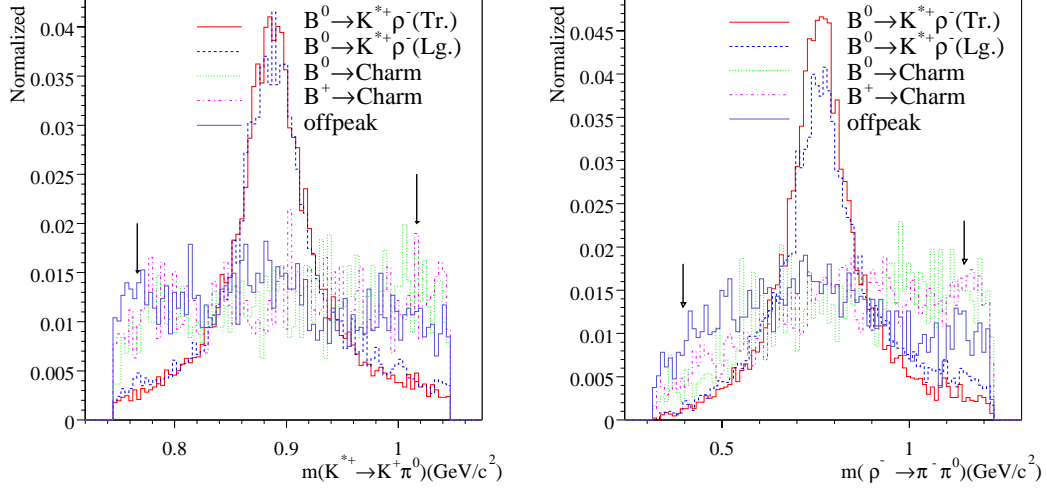


Figure 3.2: Reconstructed invariant mass of $K^{*+}\pi^0$ (left) and $\pi^-\pi^0$ (right) for signal MC, $b \rightarrow c$ backgrounds MC and offpeak data. The arrows indicate the requirements applied.

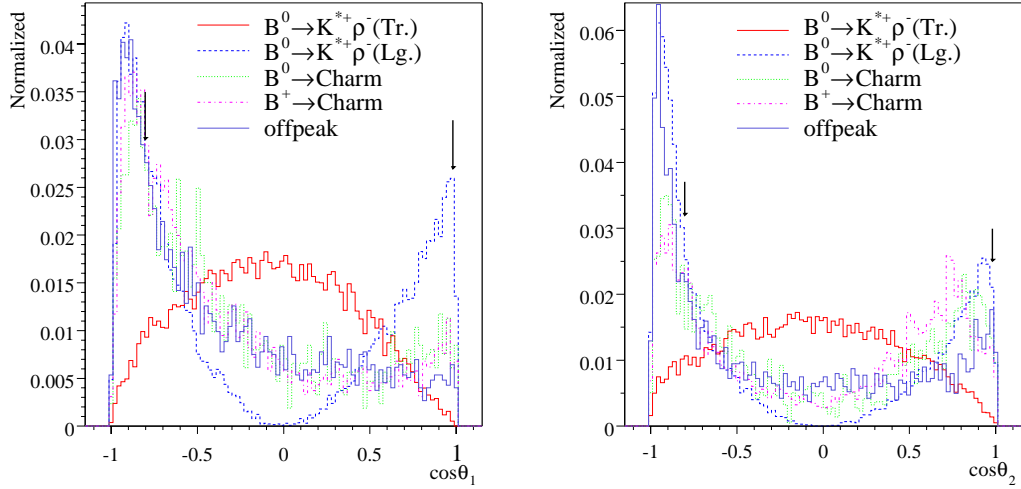


Figure 3.3: The distribution of cosine helicity angle of K^{*+} (left) and ρ^- (right) for signal MC, $b \rightarrow c$ backgrounds MC and offpeak data. The arrows indicate the requirements applied.

Data type	averaged candidates/event
$B^0 \rightarrow \rho^- K^{*+}$ longitudinal signal MC	1.39
$B^0 \rightarrow \rho^- K^{*+}$ transverse signal MC	1.22
onpeak data	1.26
offpeak data	1.25

Table 3.2: *Average number of candidates per event after all selection cuts.*

to nominal PDG [5] value:

$$\delta m^2 = (m_{\pi_1^0} - m_{\pi^0}^{PDG})^2 + (m_{\pi_2^0} - m_{\pi^0}^{PDG})^2 \quad (3.4)$$

The candidate with the lowest δm^2 value is selected. In the case that two or more candidates get the same lowest δm^2 , we randomly pick one within these candidates.

In MC, selected signal events are divided into two categories: truth matched (TM) and self-cross-feed (SCF) signal events. The TM signal events refer to those events where the correct final-state particles are identified in the reconstruction. The SCF signal events, or mis-reconstructed signal events, refer to those signal events with at least one particle not from the signal B decay used in the reconstruction. In most cases, the mis-reconstruction is due to low momentum particles, which are more likely in longitudinal signal events than in transverse signal events. This is consistent with the the SCF fractions we get in the MC signal samples, 37.1% and 21.1% for the longitudinal and transverse signal events respectively.

We have also studied choosing the candidate randomly. The comparison of selecting randomly and choosing the candidate with the lowest δm^2 , as previously described, is summarized in Table 3.3. We find the lowest δm^2 selection keeps more truth-matched events than selecting the candidate randomly, but still loses 36% (13%) of truth-matched candidates in events with multiple candidates for the longitudinal (transverse) signal MC.

Signal MC	Samples	Lowest δm^2 selection	Random selection
Lg.	all events	91%	85%
Lg.	multiple candidates	64%	43%
Tr.	all events	96%	91%
Tr.	multiple candidates	87%	56%

Table 3.3: *The ratio of number of TM signal events after and before best candidate selection.*

3.3.5 Suppression of Continuum Background

Since the energy of the $\Upsilon(4S)$ resonance is just above the $B\bar{B}$ pair production threshold, B mesons are created with little momentum in the $\Upsilon(4S)$ frame, so their decay products are rather isotropic. However, the continuum events ($q\bar{q}$ pairs) are produced with a large boost so their decay products are formed by fragmentation within a small cone; a jetty topology. The commonly used topological variables are the Legendre monomials, L_0 and L_2 , defined as

$$L_0 = \sum_{i=ROE} p_i, \quad (3.5)$$

$$L_2 = \sum_{i=ROE} p_i |\cos(\theta_i)|^2, \quad (3.6)$$

where the sum is over the charged and neutral tracks of the rest of the event, p_i is the momentum of the charged or neutral tracks, θ_i is the angle between the direction of \mathbf{p}_i and the thrust axis of the B candidate, which is defined according to $T = \frac{\sum_{i=1}^N |\mathbf{p}_i \cdot \hat{t}|}{\sum_{i=1}^N |\mathbf{p}_i|}$, where N is the number of tracks for each B candidate, and the thrust axis \hat{t} is adjusted to maximize the thrust T . We combine the monomials into a Fisher discrimination [32], and construct a *Multivariate Analyzer* (MVA), together with some other kinematic variables, to best separate signal from the background.

The MVA used in this analysis is a Neural Network Object [31]. Basically, it combines

some discriminating variables from different species as inputs, and optimizes an output to best separate them. The following variables enter the neural network as inputs:

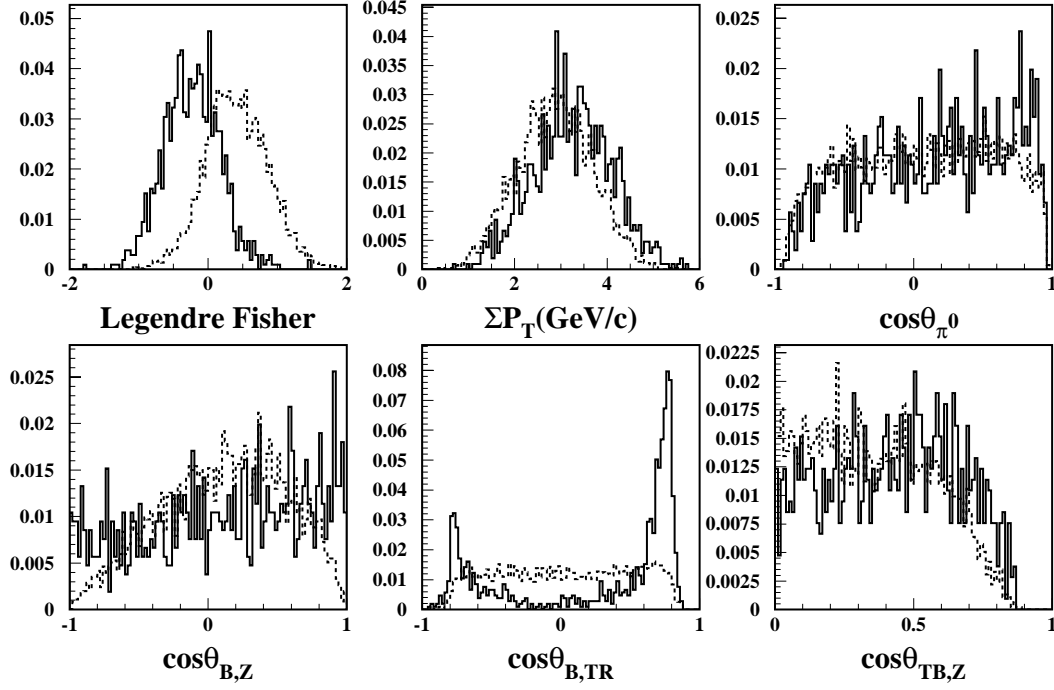


Figure 3.4: *The distribution of input variables used in training the neural network. The dashed line represents the truth-matched signal MC and the solid line is continuum background (offpeak data)*

- Fisher of the Legendre monomials;
- $\sum_{ROE} p_T$: the sum of the transverse momentum of the rest of event in the CM frame;
- $\cos(\theta_{B,z})$: the cosine of the angle between the B momentum and the z axis in the CM frame;
- $\cos(\theta_{B,TR})$: the cosine of the angle between the direction of B and the thrust of the rest of the event;

- $\cos(\theta_{T_B,z})$: the cosine of the angle between the B thrust axis and the z axis in the CM frame.
- $\cos(\theta_{\pi^0})$: the cosine of the decay angle of the π^0 from ρ^- or K^{*+} , defined in the same way as ρ^- or K^{*+} helicity. π^0 is randomly picked up from ρ^- or K^{*+} decay.

The species we want to separate are continuum background events and the truth-matched signal events. The distributions of the input variables for these two species are shown in Figure 3.4.

The neural network used is a multi-layer perception with 6 input nodes corresponding to the above 6 variables, two hidden layers of 5 and 4 nodes respectively and a single output node, NN_{out} , normalized between 0 (continuum background) and 1 (truth-matched signal). For the purpose of modeling the continuum neural network output (nno) with an analytic function, the NN_{out} is transformed with a one-to-one mapping to $nno = 1 - \text{acos}(NN_{out} + \xi)$, where ξ is a small offset (0.0008) that tunes the nno 's maximum to be 1. Figure 3.5 shows the truth-matched signal efficiency versus that of continuum background as different cuts are applied and the nno distribution for the signal MC and continuum background samples. The nno enters the ML fit so the cut is loosely applied.

3.3.6 Classification of B Related Backgrounds

Due to the presence of the broad ρ^- and K^{*+} resonances, as well as the neutral decay product (π^0), this decay mode suffers from cross-feed of other B decay modes. Since the branching ratios of these B -related backgrounds are not always well-known, they are potentially more dangerous than the continuum background. We investigated the effects of this cross-feed and evaluated the systematic biases they can introduce in our measurement.

Using generic B^+B^- and $B^0\bar{B}^0$ MC, we estimate the $b \rightarrow c$ background contribution. The $b \rightarrow c$ decay events are selected at the generator level, *i.e.* at least one of the final state

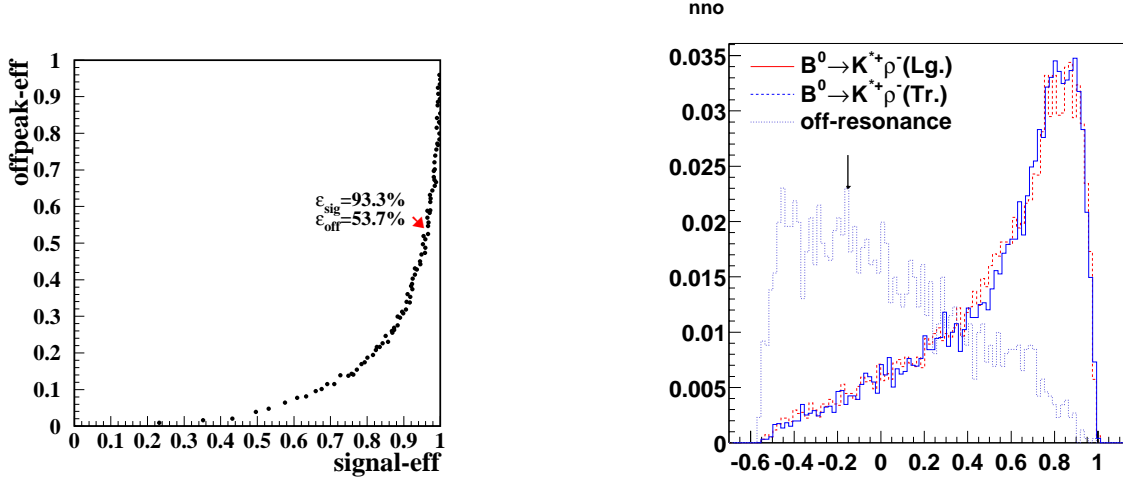


Figure 3.5: *Left: The distribution of continuum efficiencies versus truth-matched signal efficiencies with different cuts applied to the NN_{out} . Right: Distributions of the nno for longitudinal and transverse $B^0 \rightarrow \rho^- K^{*+}$ signal MC and offpeak data. The arrows indicate the requirements applied.*

particles in the whole event is required to originate from a charmed mother or grandmother. The $b \rightarrow c$ decays usually have high multiplicity. Most of these backgrounds do not peak in the signal region for the kinematic variables m_{ES} and ΔE , but they do exhibit a peaking structure for the nno distribution.

Even more dangerous are the charmless B -decays. Though their branching ratios tend to be much lower than the charmed decays, they usually peak in m_{ES} and ΔE . We use the measured branching ratios for the experimentally known decay modes. In cases where only upper limits are given, the limits are translated into branching ratios using the available information from the related studies. For all those modes not yet measured, educated guesswork is needed to deduce their branching ratios. This is done using similar, known modes and, wherever possible, rules based on isospin symmetry and/or form factor arguments, usually assuming naive factorization of the matrix elements. If none of these is available, we rely on ad hoc assumptions that consequently entail large systematic uncertainties.

Cl	Decay mode	Br. ($\times 10^{-6}$)	Eff. (%)	N_{exp}	Total events
0	$B^0 \rightarrow \rho^+ \rho_{[long]}^-$	26.4 ± 6.2	0.16	5.1 ± 1.20	365,000
1	$B^0 \rightarrow a_1^+(\rightarrow \rho^+ \pi^0) \rho_{[long]}^-$	$20 \pm 20^*$	0.07	1.66 ± 1.66	40,000
2	$B^0 \rightarrow (K^{(*)}(\rightarrow [\text{anything}] \pi)^0$	$72 \pm 72^*$	0.14	12.9 ± 12.9	214,000
3	$B^0 \rightarrow (K^{(*)}(\rightarrow [\text{anything}] \rho)^0$	$20 \pm 20^*$	0.20	4.82 ± 4.82	29,000
4	$B^0 \rightarrow \text{charm}$	-	-	309.9 ± 62.0	$187,674,000^\dagger$
5	$B^+ \rightarrow K^{*+}(\rightarrow K^+ \pi^0) \pi^0$	4.4 ± 2.5	1.26	6.82 ± 3.88	101,000
6	$B^+ \rightarrow K^{*+}(\rightarrow K^+ \pi^0) K_{[long]}^{*0}$	$15.8 \pm 15.8^*$	0.20	3.88 ± 3.88	66,000
6	$B^+ \rightarrow K^{*+}(\rightarrow K^+ \pi^0) K_{[tran]}^{*0}$	$15.8 \pm 15.8^*$	0.19	3.73 ± 3.73	66,000
7	$B^+ \rightarrow \omega K^{*+}(\rightarrow K^+ \pi^0)_{[tran]}$	$10 \pm 10^*$	0.23	2.85 ± 2.85	65,000
8	$B^+ \rightarrow K^{*0}(\rightarrow K^+ \pi^-) \rho_{[long]}^+$	14.1 ± 5.1	0.11	1.96 ± 0.71	673,500
9	$B^+ \rightarrow \phi(\rightarrow \pi \pi \pi) K^+$	4.50 ± 0.35	0.36	2.02 ± 0.16	67,000
10	$B^+ \rightarrow K^{*+}(\rightarrow K^+ \pi^0) \rho_{[long]}^0$	3.5 ± 1.3	0.48	2.05 ± 0.76	78,500
10	$B^+ \rightarrow K^{*+}(\rightarrow K^+ \pi^0) \rho_{[tran]}^0$	3.5 ± 1.3	0.33	1.42 ± 0.53	67,000
11	$B^+ \rightarrow \eta'(\rightarrow \rho^0 \gamma) K^+$	22.89 ± 1.36	0.09	2.59 ± 0.15	84,500
12	$B^+ \rightarrow (K^{(*)}(\rightarrow [\text{anything}] \pi)^+$	$40 \pm 40^*$	0.05	2.52 ± 2.52	104,000
13	$B^+ \rightarrow (K^{(*)}(\rightarrow [\text{anything}] \rho)^+$	$15 \pm 15^*$	0.14	2.55 ± 2.55	36,000
14	$B^+ \rightarrow \text{charm}$	-	-	695.8 ± 139.0	$177,600,000^\dagger$

Table 3.4: *Classification of B backgrounds. The errors on the event yields only reflect the uncertainties on the branching fractions. For $b \rightarrow c$ backgrounds, a systematic error of $\pm 20\%$ of total expected events is assigned. The branching ratios with a \star are estimated from theoretical arguments. The total events for $B \rightarrow \text{charm}$ modes, indicated by a \dagger , are for generic $B\bar{B}$ events.*

The full list of B background modes considered is shown in Table A.1-A.6 in Appendix A. Only those background decay modes with more than one event expected to yield after selection cuts are included in the fit model. Some of them with similar distributions of the discriminating variables are grouped into a class. Each background class introduces a term to the likelihood function. There are a total of 15 B background classes (see Table 3.4).

3.3.7 Suppression of Peaking Charm B Backgrounds - D^0 Veto

There are some B^0 decays to charm modes, such as $B^0 \rightarrow \bar{D}^0 \pi^0$ with $\bar{D}^0 \rightarrow K^+ \pi^- \pi^0$ have the same final state as the signal. If the tracks from these B decays are used to reconstruct

the K^{*+} and the ρ^- , these events will have peaking ΔE and m_{ES} distributions. We also find some combinatorial peaking backgrounds with $\bar{D}^0 \rightarrow K^+\pi^-$ in the final state. The invariant masses of decay modes $\bar{D}^0 \rightarrow K^+\pi^-$ and $\bar{D}^0 \rightarrow K^+\pi^-\pi^0$ are calculated with the charged tracks and the π^0 candidates, shown in Figure 3.6. A clear peak at the D^0 mass is observed.

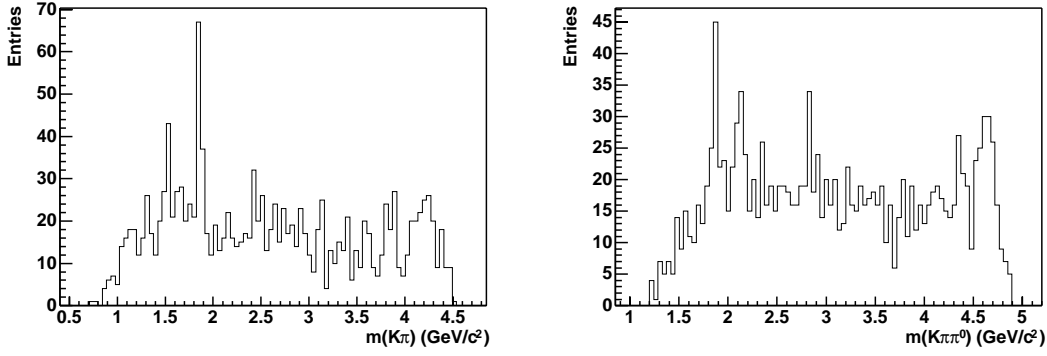


Figure 3.6: *Invariant masses of $D^0 \rightarrow K^+\pi^-$ (left) and $D^0 \rightarrow K^+\pi^-\pi^0$ (right) from $B^0 \rightarrow$ charm MC sample.*

In order to remove this contamination, a D^0 veto is applied after all other selections. Using the PDG value of D^0 mass ($m_{D^0}^{PDG} = 1.8645 \text{ GeV}/c^2$), the following selections are required:

- $|m_{K^-\pi^+} - m_{D^0}^{PDG}| > 0.02 \text{ GeV}/c^2$
- $|m_{K^-\pi^+\pi^0} - m_{D^0}^{PDG}| > 0.04 \text{ GeV}/c^2$

Figure 3.7 shows the m_{ES} distributions for the neutral $b \rightarrow c$ background before D^0 veto and the vetoed D^0 peaking backgrounds. After these cuts are applied, most of the peaking charm-backgrounds are suppressed and m_{ES} shapes for both neutral and charged $b \rightarrow c$

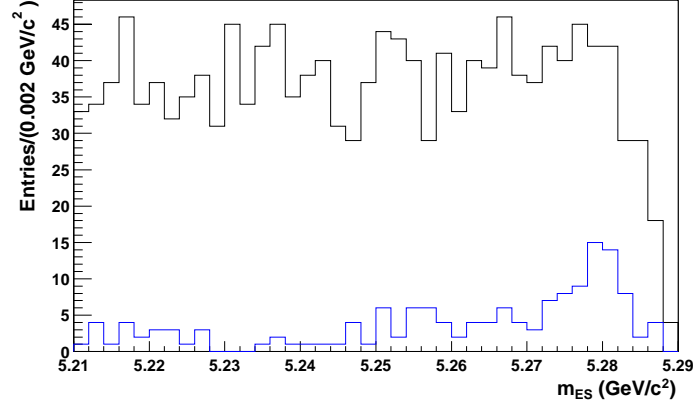


Figure 3.7: m_{ES} distribution of neutral $b \rightarrow c$ background. The upper is before D^0 veto and the lower is the vetoed peaking $B^0 \rightarrow D^0 \pi^0$

backgrounds can be parameterized with an Argus function like that used for the continuum background m_{ES} shape (see Figure 3.8).

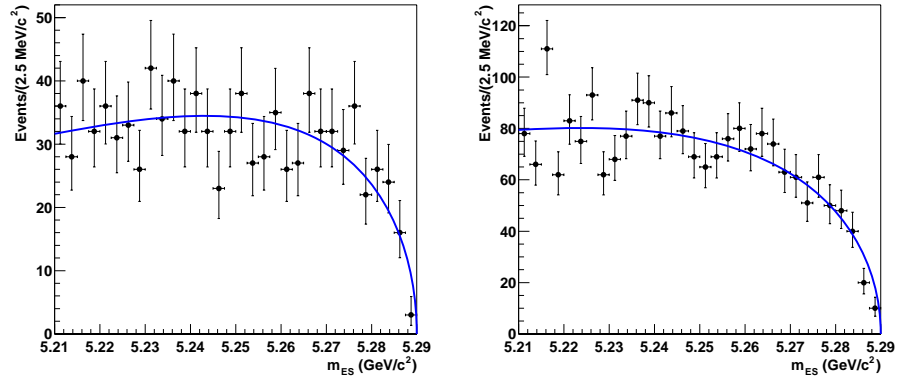


Figure 3.8: The m_{ES} shapes for charm-backgrounds can be described by Argus function after D veto. Left plot is for neutral B ; right for charged B .

3.3.8 Efficiencies

Table 3.5 summarizes the efficiency of each cut when applied to the longitudinal and transverse signal MC, onpeak and offpeak data. For offpeak data, since it's taken 40 MeV below $\Upsilon(4S)$ resonance, m_{ES} cut is shifted by 20 MeV/ c^2 to be $5.19 < m_{\text{ES}} < 5.27 \text{ GeV}/c^2$, as indicated by '★' in the table. The total efficiency is 6.8% for the longitudinal signal MC and 13.9% for the transverse signal MC.

Cut description	$\epsilon_{\text{Lg.MC}}$ (%)	$\epsilon_{\text{Tr.MC}}$ (%)	ϵ_{onpeak} (%)	$\epsilon_{\text{offpeak}}$ (%)
Reconstruction	41.2	39.5	-	-
π^0 quality cuts	83.0	84.2	70.9	70.0
K Selection	77.9	80.1	30.1	28.9
π Selection	96.2	97.2	83.9	82.9
Vector masses cuts	68.8	78.3	10.7	11.3
Vector helicities cuts	60.1	92.3	61.5	61.4
$-0.12 < \Delta E < 0.15 \text{ GeV}$	75.7	82.6	33.0	34.5
$5.21 < m_{\text{ES}} < 5.29 \text{ GeV}/c^2$ ★	99.8	99.9	88.2	99.8
$nno > -0.15$	94.2	94.5	59.0	56.9
D^0 -veto	94.6	98.4	94.4	96.3
Total efficiency	6.8	13.9	-	-

Table 3.5: *Summary of progressive selection efficiencies for signal MC and data samples. The efficiencies for each cut are evaluated relative to the number of events retained after pre-selection, they don't include the loss of events from the other cuts.*

3.4 Maximum Likelihood (ML) Fit

To measure the branching ratio of a B decay mode, \mathcal{B} , we need to know the total number of $B\bar{B}$ pairs in the data sample, $N_{B\bar{B}}$, the number of observed signal events, N_{obs} , and the total efficiency of signal selection, ϵ . The \mathcal{B} is calculated as

$$\mathcal{B} = \frac{N_{\text{obs}}}{\epsilon N_{B\bar{B}}}. \quad (3.7)$$

We know the $N_{B\bar{B}}$ from the integrated luminosity of data sample and the cross section for $e^+e^- \rightarrow \mathcal{R}(4S)$. The ϵ is obtained using signal MC events. For the signal yield N_{obs} , there are two methods to extract it.

A direct *Cut & Count* method applies much tighter cuts on the signal region in order to have a clean signal. As a result, the efficiency will be very low which is not suitable for this decay mode analysis with the branching ratio at an order of 10^{-6} and limited data samples.

The other method is to extract the signal yield by means of an unbinned, extended ML fit to the data. The candidates are selected with relative loose cuts described in previous sections, especially on the discriminating variables used in the fit, to allow sufficient sidebands for parametrization of the background.

The selected onpeak data sample is assumed to consist of the TM and SCF signal events, both longitudinal and transverse, the continuum background ($q\bar{q}$ events), and the charm and charmless B backgrounds (See Table 3.4). Each component is modeled with a Probability Density Function (PDF) of seven discriminating variables: m_{ES} , ΔE , nno , the mass of the two vector mesons, M_{V1} and M_{V2} , and the helicity of the two vector mesons, $\cos\theta_1$ and $\cos\theta_2$, which determine the polarization fraction of signal events.

3.4.1 The Likelihood Function

For the sample of N events, the extended likelihood function is built as

$$\mathcal{L} = e^{-N'} \prod_{i=1}^N \left(n_{sig} P_{sig,i}^{total} + \sum_{backgrounds,j} n_j P_{j,i} \right) \quad (3.8)$$

where $N'(N)$ is the expected (observed) number of events, n_{sig} is the number of signal events, n_j is the number of events for background component j , P is the PDF for each component

with the generic form:

$$P_j = P_j(m_{\text{ES}}, \Delta E, nno, \cos\theta_1, M_{V1}, \cos\theta_2, M_{V2}). \quad (3.9)$$

The TM and SCF signal components have two parts, longitudinal and transverse, defined as

$$P_k = (1 - f_{SCF,k})P_{sig,k} + f_{SCF,k}P_{SCF,k} \quad (3.10)$$

where $f_{SCF,k}$ is the SCF fraction for the polarization k , longitudinal or transverse. Since we have different efficiencies for the longitudinal and transverse signal events, the observed longitudinal polarization fraction F_L is introduced and related to f_L by

$$F_L = \frac{f_L R}{1 - f_L(1 - R)} \quad (3.11)$$

where $R = \epsilon_{long}/\epsilon_{tran} = 0.492$ is the ratio of the efficiencies for longitudinal and transverse signal events.

The total signal PDF is given by

$$P_{sig}^{total} = F_L[(1 - f_{SCF,L})P_{TM,L} + f_{SCF,L}P_{SCF,L}] + (1 - F_L)[(1 - f_{SCF,T})P_{TM,T} + f_{SCF,T}P_{SCF,T}] \quad (3.12)$$

The helicity distribution for $B \rightarrow VV$ modes is shown in (1.10). However, we need to take the detector acceptance effects into account for final signal PDFs. Regardless of the normalization, the total helicity signal PDF can be written as:

$$\mathcal{P}_{sig}^{hel}(\theta_1, \theta_2, f_L) = \left[f_L \cos^2\theta_1 \cos^2\theta_2 + \frac{1}{4}(1 - f_L) \sin^2\theta_1 \sin^2\theta_2 \right] \mathcal{G}(\theta_1) \mathcal{G}(\theta_2), \quad (3.13)$$

where f_L is the true physics longitudinal polarization fraction, $\mathcal{G}(\theta_1)$ and $\mathcal{G}(\theta_2)$ (see Table 3.6)

are parametrizations of the detector acceptance effects for the two helicity angles. We assume the acceptance effects for the two vector mesons are independent so that the parametrization can be written as the product of function of θ_1 and function of θ_2 .

The signal yields n_{sig} and the longitudinal polarization fraction f_L are obtained by maximizing the likelihood, \mathcal{L} .

3.4.2 PDF Definitions

component	m_{ES}	ΔE	nno	$cos\theta_1$	M_{V1}	$cos\theta_2$	M_{V2}
TM (long/tran)	CB	CB+G	K	H	BW	H	BW
SCF (long/tran)	CB+G	GG	K	K	K	K	K
$q\bar{q}$	<u>Argus</u>	<u>P1</u>	<u>P3</u>	<u>P4</u>	K	<u>P4</u>	K
charm B-backgrounds	<u>K</u>	K	K	K	K	K	K
charmless B-backgrounds	K	K	K	K	K	K	K

Table 3.6: *The types of PDFs to model the different variables for each component in the likelihood fit. The underlined continuum PDFs have their parameters floated in the nominal fit.*

All the shapes for signal PDFs and B backgrounds PDFs are taken from MC (see Figure B.1-B.20). Most of the continuum parameters are floated in the fit to onpeak data (See Section 3.5 for all the floated parameters). Table 3.6 summarizes all the PDFs used in the fit. The abbreviations in the table are defined as: Argus - Argus function; BW - Breit-Wigner; CB - Crystal Ball [35]; G - Gaussian; K - KEYS; P_n - Polynomial of order n ; H - $cos^2\theta_H \times P_2$ for transverse polarization or $sin^2\theta_H \times P_2$ for longitudinal polarization.

The KEYS [36] PDF is a non-analytic parametrization and particularly useful to adjust complicated shapes that are too difficult to be described by a simple analytic function. All the PDFs for B backgrounds use KEYS.

3.4.3 PDF Correlations

The seven discriminating variables in the PDFs are assumed to be uncorrelated. The linear correlations for the TM and SCF signal MC, offpeak data and B backgrounds MC are given in Appendix C. The profile plots of the mass and helicity of vector mesons for the TM, SCF signal, and continuum background are shown in Figure 3.9-3.11. No significant correlations are seen except for a small one in the SCF signal events. Detailed studies of the effects of these correlations are in Section 3.6.

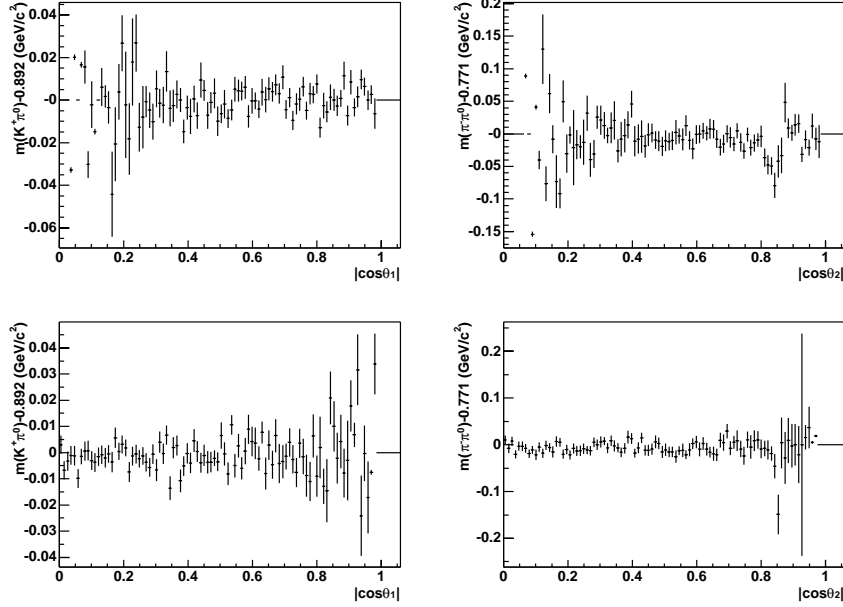


Figure 3.9: *The profile plots of the mass and helicity of vector mesons for the TM signal events. Upper two plots are for longitudinal, lower two for transverse. Left plots are for K^* , right for ρ .*

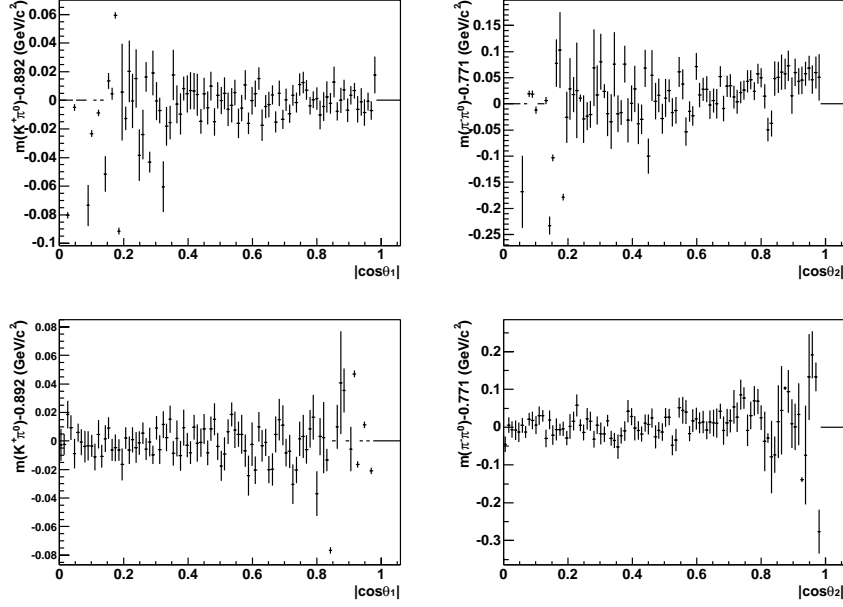


Figure 3.10: *The profile plots of the mass and helicity of vector mesons for SCF signal events. Upper two plots are for longitudinal, lower two for transverse. Left plots are for K^* , right for ρ .*

3.5 Fit Validations

The ML fitter is built with the assumption that the discriminating variables are uncorrelated. In the blind analysis stage, we need to check that this assumption is correct and make sure the fitter is fully validated before unblinding our results. We model the signal and B -background PDFs from MC samples. For continuum background, the parameters are taken from the blind fit to onpeak data. We validate the fitter with PDF-generated (toy) MC samples and a mixture of toy MC for backgrounds and fully simulated MC for signal.

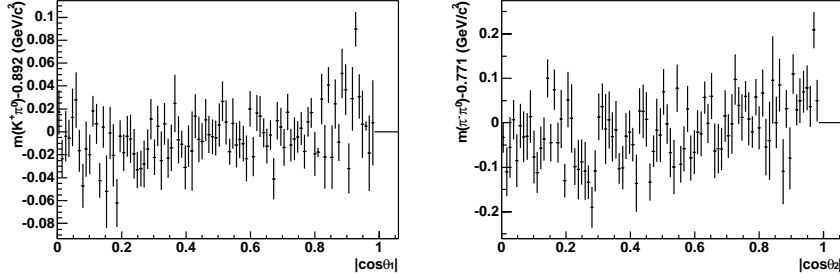


Figure 3.11: *The profile plots of the mass and helicity of vector mesons for continuum background from offpeak data. Left plot is for K^* , right for ρ .*

3.5.1 Fits to Toy MC Samples - Pull Distributions

The toy MC samples are generated using PDF parameters from the nominal fit, which by definition don't include any correlations among the discriminating variables. Fitting on these samples will help to show the integrity of the fitting code. A total of 300 toy experiments were generated for each of three different generated f_L 's, 0.4, 0.7, 0.9, and the same generated signal yields of $n_{sig} = 60$. The "pull" distribution of n_{sig} and f_L , is defined as $pull = \frac{x_{fit} - x_{gen.}}{\sigma_x}$, where $x_{fit}(x_{gen.})$ is the fitted (generated) value of x , and σ_x is the fitted error for each toy experiment. For a good fit, it is expected to have a normal Gaussian distribution (see Figure 3.12).

Table 3.7 shows the mean and width of pull, and the mean value of fitted error, for n_{sig} and f_L . No significant bias is found in this study. The mean error we expect for 60 signal events is ~ 16.5 events.

3.5.2 Fits to the Mixture of Signal MC Events and Toy Samples

The performance of the fitter is also studied with fits to samples composed of signal MC events and the PDF-generated toy samples for B backgrounds and continuum background.

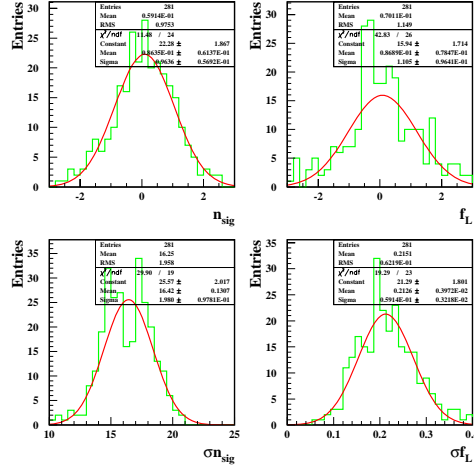


Figure 3.12: Pull distribution for fit on toy samples. The generated values are taken from the nominal fit result.

This test will reveal if there is any bias introduced by ignoring correlations in the signal discriminating variables. The proper proportions of signal, B -backgrounds and continuum background are determined from what is expected in the selected onpeak data. Limited by the availability of signal MC events, we perform 145 experiments with fits to samples containing signal MC events only; signal MC events embedded with the toy continuum background; and the signal MC events plus the toy B -backgrounds and continuum background. The signal components are generated with 60 signal yields and $f_L = 0.7$. The fit results are sum-

Generated	μ_{Pull}	σ_{Pull}	$\bar{\sigma}_{fit}$
$n_{sig} = 60$	0.02 ± 0.06	0.921 ± 0.056	16.13 ± 0.12
$f_L = 0.4$	0.05 ± 0.06	0.925 ± 0.060	0.19 ± 0.003
$n_{sig} = 60$	0.01 ± 0.05	0.862 ± 0.042	16.97 ± 0.09
$f_L = 0.7$	0.02 ± 0.06	0.933 ± 0.045	0.14 ± 0.003
$n_{sig} = 60$	-0.02 ± 0.06	0.884 ± 0.054	16.72 ± 0.15
$f_L = 0.9$	-0.09 ± 0.07	0.912 ± 0.060	0.10 ± 0.0002

Table 3.7: Summary of toy fit studies for the three different generated f_L 's, and the generated signal yields of 60.

marized in Table 3.8. No bias is seen on the fitted yields and f_L for the fits on the signal MC events only. The fits on samples of the signal MC events mixed with the toy B -backgrounds and continuum background show a bias of 4.2 events on the signal yield, which is assigned as systematic uncertainty.

Mode	n_{sig}	f_{long}
Generated value	60	0.7
signal MC events	61.0 ± 1.1	0.708 ± 0.010
signal MC events + toy $q\bar{q}$	64.2 ± 1.2	0.698 ± 0.009
signal MC events + toy $q\bar{q}$ + toy B -backgrounds	64.2 ± 1.2	0.691 ± 0.010

Table 3.8: *Results from fits on the mixture of the signal MC events, and toy B -backgrounds and continuum background samples.*

3.5.3 Fits to MC Samples and Offpeak Data

To test the quality of PDF parametrization and the influence of possible correlations between the discriminating variables in the likelihood fit, we have performed fits on high statistics control samples: offpeak data, longitudinal and transverse signal MC, $B^0\bar{B}^0$ generic MC with signal removed, B^+B^- generic MC and $B^0/B^+ \rightarrow charm$ MC samples. The signal yields, continuum yields and charm backgrounds yields are floated in the fit. The f_L is floated for fits on the signal MC but fixed to 0.7 for fits on other samples because it's meaningless to fit samples without signal while leaving f_L free, which would also lead to fits failing to converge. What value is f_L fixed to doesn't affect the results too much. In all cases we find reasonable agreement with the expectations. There is relatively large cross-feeds between B -backgrounds and continuum yield due to the weak discrimination between them. The results are shown in Table 3.9.

Samples	Events	n_{sig}	N_{cont}	$N_{B \rightarrow charm}$	f_L
Lg. signal MC	6084	6073.7 ± 78.3	9.8 ± 11.1	0.5 ± 10.1	1.001 ± 0.0004
Tr. signal MC	9656	9561.7 ± 98.6	27.3 ± 16.7	62.7 ± 20	-0.005 ± 0.003
Offpeak data	1235	4.7 ± 4.9	1222.5 ± 44.5	7.8 ± 2.9	0.7 (fixed)
$B^0\bar{B}^0$ MC (No Signal)	1251	13.4 ± 6.9	0.0 ± 13.7	1154.8 ± 35.4	0.7 (fixed)
$B^0 \rightarrow charm$	963	2.29 ± 5.28	17.0 ± 20.6	959.1 ± 33.9	0.7(fixed)
B^+B^- generic MC	2550	-5.3 ± 6.2	27.8 ± 19.0	2433.4 ± 53.6	0.7(fixed)
$B^+ \rightarrow charm$ MC	2168	-2.0 ± 8.3	14.4 ± 17.6	2155.6 ± 50.4	0.7 (fixed)

Table 3.9: *Fit results on offpeak data and different MC samples.*

3.6 Fit Stability Tests

Fits to the onpeak data with different PDFs parametrizations are also studied to test the stability of the ML fit. We have performed fits to onpeak data with two-dimensional (2D) mass-helicity PDFs for B backgrounds, continuum background, the SCF signal and the TM signal. These fits are done with the fit results still blind. There is a decrease of 6.2 events and an increase of 8 events on the signal yield if 2D mass-helicity PDFs are used for B backgrounds and the TM signal, respectively. There are no large changes on f_L except a shift of +0.14 when 2D mass-helicity PDFs are used for the TM signal model. To understand this effect, the toy samples with 2D mass-helicity PDFs for the TM signal are generated and fit back with both 2D PDFs and one-dimension (1D) PDFs. The differences on the signal yields and f_L between the two fits are shown in Figure 3.13, which does show a shift on f_L at the toy level. We have also studied the fits with 2D $m_{ES}-\Delta E$ PDFs model for B -backgrounds in the ML fit. All these results are given in Table 3.10 and show a good stability of the fitter.

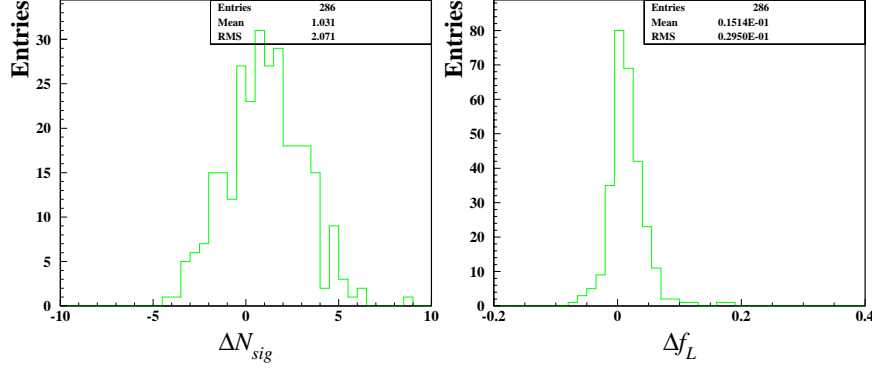


Figure 3.13: *Left plot: $\Delta n_{sig} = N_{2D} - N_{1D}$, right plot: $\Delta f_L = f_{L,2D} - f_{L,1D}$, where 2D means the two-dimension mass-helicity PDFs for the TM signal, 1D means one-dimension PDFs of mass and helicity of vector mesons for the TM signal in the nominal fit.*

Fit models	n_{sig}	f_L
2D $m_{ES} - \Delta E$ PDFs for B backgrounds	$(xx - 1.3) \pm (x - 0.7)$	$(xx - 0.019) \pm (x - 0.03)$
2D mass-helicity PDFs for B backgrounds	$(xx - 6.2) \pm (x - 6.1)$	$(xx + 0.10) \pm (x - 0.06)$
2D mass-helicity PDFs for continuum	$(xx - 5.0) \pm (x + 7.0)$	$(xx + 0.02) \pm (x + 0.01)$
2D mass-helicity PDFs for SCF signal	$(xx + 3.5) \pm (x + 3.3)$	$(xx + 0.05) \pm (x + 0.02)$
2D mass-helicity PDFs for truth signal	$(xx + 8.0) \pm (x + 7.0)$	$(xx + 0.14) \pm (x + 0.03)$

Table 3.10: *Stability fits tests on the onpeak data with different PDFs parametrization modeled.*

3.7 Fit Result

3.7.1 Nominal Fit to Onpeak data

Following the fit validation tests presented in previous sections, the signal yield n_{sig} and the longitudinal polarization fraction f_L were unblinded. The results are shown in Table 3.11, along with 10 other parameters for continuum PDFs parametrization and the continuum

Parameter	Description	Value
n_{sig}	Number of $B^0 \rightarrow \rho^- K^{*+}$ events	55.8 ± 16.1
f_L	Longitudinal polarization fraction	0.267 ± 0.310
ξ	Continuum Argus slope parameter	-19.6 ± 1.15
ΔE_{p1}	First term of the continuum ΔE PDF	-1.51 ± 0.14
ΔE_{p2}	Second term of the continuum ΔE PDF	3.55 ± 1.68
a_1	Continuum NN parameter	1.82 ± 0.38
a_2	Continuum NN parameter	0.04 ± 0.09
a_3	Continuum NN parameter	0.95 ± 0.03
$V1_{contp2}$	Continuum helicity parameter for K^* meson	-0.21 ± 0.08
$V1_{contp3}$	Continuum helicity parameter for K^* meson	-2.75 ± 0.07
$V2_{contp2}$	Continuum helicity parameter for ρ meson	-0.29 ± 0.07
$V2_{contp3}$	Continuum helicity parameter for ρ meson	-1.24 ± 0.06
N^{qq}	Number of continuum events	13089 ± 120

Table 3.11: *Summary of the onpeak data fit result.*

background yield. The fitted values of the signal yield and f_L are

$$\begin{aligned}
 n_{sig} &= 55.8 \pm 16.1 \\
 f_L &= 0.267 \pm 0.310.
 \end{aligned}
 \tag{3.14}$$

Using the difference between the $-2\ln(\mathcal{L})$ values obtained in the nominal fit and in a fit with the signal yield fixed to zero, and assuming a parabolic behaviour of $-2\ln(\mathcal{L})$ around its minimum, the significance of the fitted signal yield relative to zero is found to be 4.2σ .

3.7.2 Goodness of Fit

One test of the overall fitting procedure is to check the goodness-of-fit by plotting the distribution of the $-\ln(\mathcal{L})$ values, obtained from fits on the nominal toy MC samples and comparing it to the value obtained from the nominal fit to onpeak data (see Figure 3.14), which is expected to lie within a few sigma of the mean of the distributions of the nominal

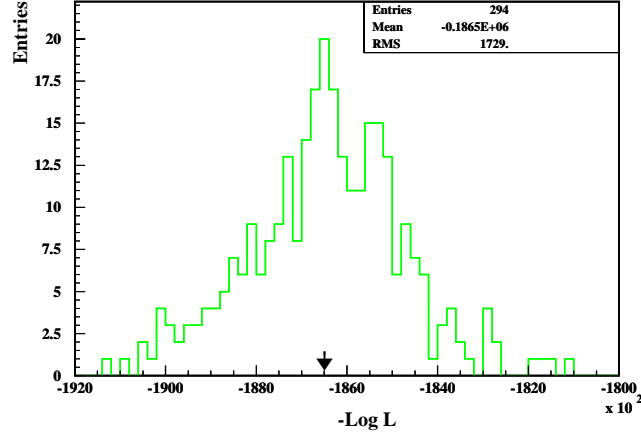


Figure 3.14: *Distribution of the $-\ln(\mathcal{L})$ values from the fits on the toy MC samples. The arrow indicates the value obtained from the nominal fit to onpeak data.*

toy MC samples for a good fit. The value for the nominal fit to onpeak data is in good agreement with the distribution from the fit to the toy samples.

3.7.3 Projection Plots

The fit performance can be further illustrated by means of the likelihood ratio [34, 37]

$$r_i = \frac{P_{sig}^{total}}{P_{sig}^{total} + P_{q\bar{q},i}}, \quad (3.15)$$

for all selected events $i = 1, \dots, N$. Its distribution for the selected onpeak data samples entering the ML fit is shown by the dots with error bars in Figure 3.15. The expectations from high statistics toy samples are shown as the histogram normalized to the total number of events in the data sample. The left is for the whole range on a logarithmic scale. The right is zoomed into the signal region on a linear scale. A signal excess and an agreement between data and expectations are observed.

Figure 3.16 shows the projection plots of the discriminating variables used in the fit. To

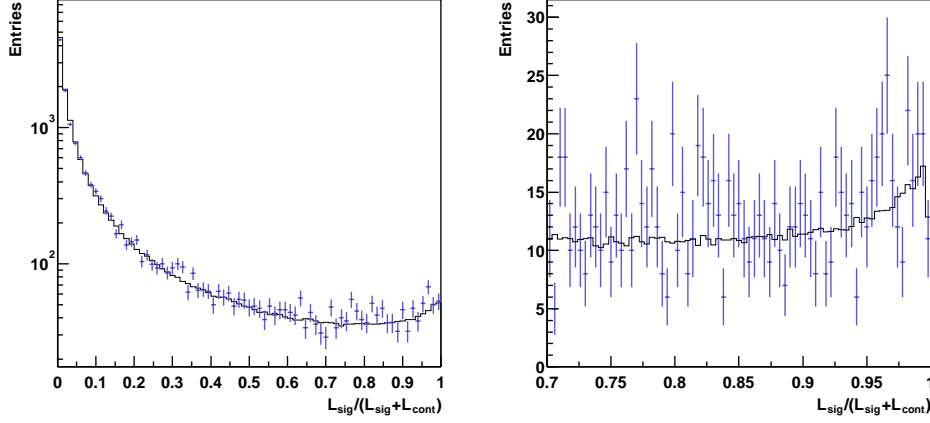


Figure 3.15: *Distributions of the likelihood projections (3.15) for data and toy MC expectation (Left plot: logarithmic scale, right plot: linear scale with zoom into the signal region). The high statistics toy MC distributions are normalized to the fit results given in Table 3.11.*

see clearly the signal, data samples have been signal-enhanced by applying tight cuts on the ratio of likelihood for signal and continuum. The likelihood is calculated with the plotted variable excluded.

3.8 Systematic Uncertainties

Besides the statistical uncertainties, the measurement receives the systematic uncertainties from various sources.

3.8.1 Branching Ratio of B -Backgrounds

We estimate the systematic uncertainty due to the uncertainties on the branching ratio of B backgrounds by varying the corresponding expected yields in the fit to onpeak data. For a specific B background, if its branching ratio has been measured, the yield will be varied within one standard deviation; if its branching ratio has not been measured, the variation

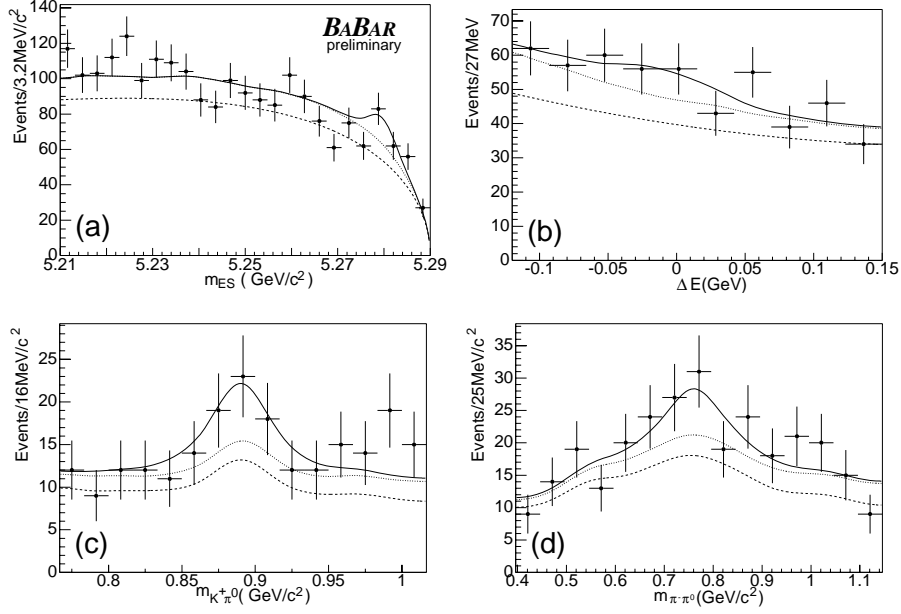


Figure 3.16: *Distributions of m_{ES} , ΔE , K^{*+} mass and ρ^- mass for samples enhanced in signal range using likelihood ratio cuts. The bottom line is the projection of continuum background, the middle line the projection of the sum of backgrounds and the top line the projection of the total likelihood.*

of the yield will be conservatively within the estimated valid range (usually $\pm 100\%$). The resulting systematics are divided by $\sqrt{3}$ to take into account the smaller r.m.s. of a uniform Bayesian prior compared to a Gaussian standard deviation. For the $b \rightarrow c$ backgrounds, the variation is $\pm 20\%$ of the expected yields. The resulting systematic errors are summarized in Table 3.12.

3.8.2 SCF Fraction

Following the systematic study performed in the $B^0 \rightarrow \rho^\pm \pi^\mp$ analysis [38], where the control sample of $B^0 \rightarrow D^+ \rho^-$ data and the MC events are used to determine how well the SCF is described by the MC and a systematic uncertainty of $\pm 5\%$ on the SCF fraction is calculated. We draw on this study and vary the SCF in the fit by $\pm 5\%$ per π^0 to evaluate the systematic

Cl	Mode	Δn_{sig}	Δf_L
0	$B^0 \rightarrow \rho^+ \rho^-_{[Lg.]}$	0.58	0.0079
1	$B^0 \rightarrow a_1^+(\rightarrow \rho^+ \pi^0) \rho^-_{[Lg.]}$	0.05	0.0023
2	$B^0 \rightarrow (K^{(**)}(\rightarrow [anything] \pi)^0$	0.42	0.0092
3	$B^0 \rightarrow (K^{(**)}(\rightarrow [anything] \rho)^0$	0.19	0.0039
4	$B^0 \rightarrow charm$	0.34	0.0053
5	$B^+ \rightarrow K^{*+}(\rightarrow K^+ \pi^0) \pi^0$	1.18	0.0166
6	$B^+ \rightarrow K^{*+}(\rightarrow K^+ \pi^0) K^{*0}(\rightarrow K^+ \pi^-)$	0.39	0.0057
7	$B^+ \rightarrow \omega K^{*+}(\rightarrow K^+ \pi^0)_{[Tr.]}$	0.10	0.0031
8	$B^+ \rightarrow K^{*0}(\rightarrow K^+ \pi^-) \rho^+_{[Lg.]}$	0.03	0.0035
9	$B^+ \rightarrow \phi(\rightarrow \pi \pi \pi) K^+$	0.27	0.0040
10	$B^+ \rightarrow K^{*+}(\rightarrow K^+ \pi^0) \rho^0$	0.47	0.0088
11	$B^+ \rightarrow \eta'(\rightarrow \rho^0 \gamma) K^+$	0.01	0.0002
12	$B^+ \rightarrow (K^{(**)}(\rightarrow [anything] \pi)^+$	0.17	0.0031
13	$B^+ \rightarrow (K^{(**)}(\rightarrow [anything] \rho)^+$	0.14	0.0025
14	$B^+ \rightarrow charm$	0.48	0.0087
	Total uncertainty	1.67	0.0293

Table 3.12: *Summary of the systematic uncertainties due to uncertainties on the branching ratio of B backgrounds.*

uncertainties.

3.8.3 Ratio of Longitudinal and Transverse Signal Efficiencies

The ratio of selection efficiencies of the longitudinal and transverse signal, R , is taken from the signal MC samples for the nominal fit. Using the data control sample $B^0 \rightarrow D^+ \rho^-$, an uncertainty of 4.0% is estimated and the systematic uncertainties due to the R is obtained by varying the R within its error.

3.8.4 Uncertainties Relating to the ML Fit

Fitting Procedure

The fitter has been validated with fits to the toy MC samples and the fit model has been tested with fits to high statistics MC event samples, as well as the toy-substituted MC samples that contain the signal MC and toy backgrounds components. The differences found between the fitted value and the generated values in these validation studies are assigned as systematic uncertainties.

PDF Parametrizations

The fixed parameters of PDFs are varied according to their uncertainties in the parametrizations that are taken from MC events.

- **PDFs for m_{ES} and ΔE**

For the continuum, the ξ parameter of the Argus function and the slope and second order coefficient of the ΔE polynomial are floated in the fit. Their statistical uncertainties are properly propagated among the fit parameters, so no additional systematic uncertainties are assigned to the m_{ES} and ΔE continuum parameterizations. The fixed parameters of m_{ES} and ΔE for both TM and SCF signal are varied according to their uncertainties and the fit is repeated to take the difference from the nominal fit as systematic uncertainties.

- **PDFs for mass and helicity of vector mesons**

The fixed parameters of mass and helicity of vector mesons for the TM signal are varied in the fit by the uncertainties in the parametrizations to obtain the systematic uncertainties.

- **PDFs for nno**

For the continuum, the nno PDF is obtained from the nominal onpeak data fit and no separate systematic uncertainties are assigned. For the TM and SCF signal, we again follow the validation results in the $B^0 \rightarrow \rho^\pm \pi^\mp$ analysis and a correction function for the MC distribution is got from the fully reconstructed $B^0 \rightarrow D^+ \rho^-$ control samples. The PDFs are re-weighted according to this correction function and the fit is repeated to obtain the associated systematics.

3.8.5 Particle Identification

The performance of particle identification is not the same for data and MC because the MC is not optimally tuned to the data. Using the data control samples, the efficiency and misidentification of particle selectors are tabulated in PID tables, from which we build new particle selectors to substitute those used in this analysis. The fit is repeated to obtain the associated systematic uncertainty.

3.8.6 Neutral Correction

The selection efficiency of photons is overestimated in the MC and we have to smear the MC to match data [39]. For each π^0 , there is a correlated systematic error of 5% and also an additional 2.5% uncorrelated error. This uncertainty contributes to the branching ratio only. Thus the correlated error is dominant here. The total uncertainty due to neutral correction is 10.3%.

3.8.7 Tracking Efficiency

There is also a slight disagreement between MC and data for detecting charged tracks. An efficiency correction is computed at the reconstruction level [40]. A flat correction of 0.5%

is applied to each of the tracks used in this analysis. The total correction value is quoted as a systematic uncertainty.

3.8.8 B Counting

The number of $B\bar{B}$ pairs in the sample is determined by selecting inclusive hadronic events in both onpeak and offpeak data, assuming the increase in the ratio of hadronic events to muon pairs between on and off resonance running is due to $\Upsilon(4S)$ production. The uncertainty of this measurement is 1.1% and is included as a systematic error in the branching ratio.

3.8.9 Longitudinal Polarization Fraction f_L

If we calculate the branching ratio from the signal yield, we need know the efficiencies, which is determined by the fitted value of f_L . Or we can extract the branching ratio directly from the ML fit so that the uncertainty on f_L is properly propagated among the floated fit parameters with their correlations taken into account. No additional systematic error is assigned to the f_L .

3.8.10 Non-resonance Contributions

In this analysis, we do not include a fit component for other B decays with the same final-state particles selected within the K^* or ρ resonance mass window, such as the non-resonant decays $B^0 \rightarrow K^+\pi^-\pi^0\pi^0$, $B^0 \rightarrow \rho^-K^+\pi^0$ and $B^0 \rightarrow K^{*+}\pi^-\pi^0$. The contribution of these decays to the fit results is significantly suppressed by the selection requirements on the masses and by the mass and helicity-angle information in the fit. To check the sensitivity of our results to the presence of nonresonant $B^0 \rightarrow K^+\pi^-\pi^0\pi^0$, $B^0 \rightarrow \rho^-K^+\pi^0$ and $B^0 \rightarrow K^{*+}\pi^-\pi^0$ decays, we explicitly include a fit component for each of them, assuming a phase-space decay model. The selection requirements alone suppress the $B^0 \rightarrow K^+\pi^-\pi^0\pi^0$ ($B^0 \rightarrow \rho^-K^+\pi^0$ and

$B^0 \rightarrow K^{*+}\pi^-\pi^0$) efficiency by two(one) orders of magnitude relative to $B^0 \rightarrow \rho^- K^{*+}$. After the full selection, the efficiencies for $B^0 \rightarrow K^+\pi^-\pi^0\pi^0$, $B^0 \rightarrow \rho^- K^+\pi^0$ and $B^0 \rightarrow K^{*+}\pi^-\pi^0$ are 0.22%, 0.55% and 1.2% respectively.

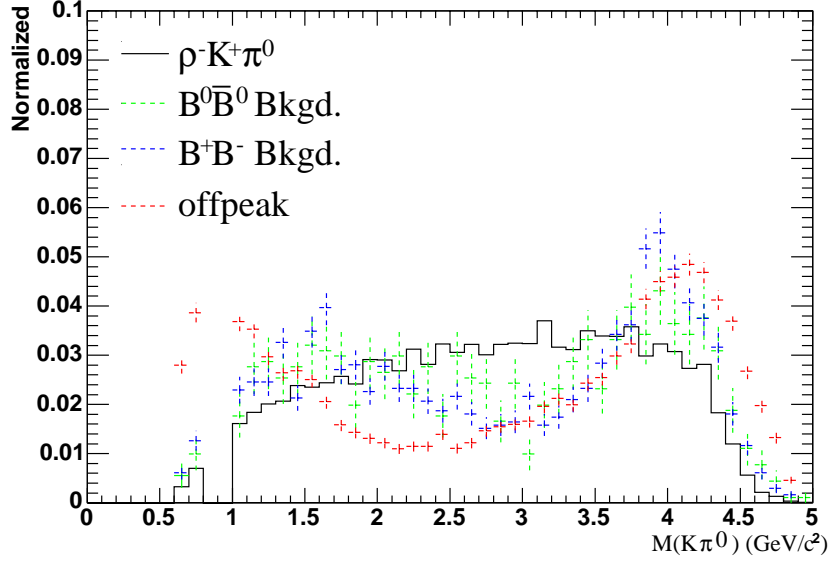


Figure 3.17: $m(K^+\pi^-)$ distributions for $B^0 \rightarrow \rho^- K^+\pi^0$ non-resonance, $B^0 \rightarrow \text{Charm}$, $B^+ \rightarrow \text{Charm}$ and offpeak data. An anti-cut has been applied to remove the $K^*(892)$ mass region.

An estimation of the contribution from $B^0 \rightarrow \rho^- K^+\pi^0$ non-resonance has been done by applying an anti-cuts on $m(K^+\pi^0)$ invariant mass. As shown in Figure 3.17, the $m(K^+\pi^0)$ distribution from $B^0 \rightarrow \rho^- K^+\pi^0$ non-resonance MC simulation ranges from 0.5 GeV/ c^2 to 4.5 GeV/ c^2 . We made a 3σ anti-cut on $m(K^+\pi^0)$ to remove the $K^*(892)$ mass region. To further remove possible $B\bar{B}$ and $q\bar{q}$ backgrounds, we select the invariant mass range of $2.0 < m(K^+\pi^0) < 3.5$ GeV/ c^2 as the signal range for $B^0 \rightarrow \rho^- K^+\pi^0$. The total efficiency is about 5.3%. In the ML fit, we use only m_{ES} , ΔE , and nno to separate $B^0 \rightarrow \rho^- K^+\pi^0$ non-resonance from continuum and B backgrounds and float all of the parameters related to the PDFs for continuum background. We get a fitted yield of $117 \pm 81(\text{stat.})$ and obtain an upper limit as $\mathcal{B}(B^0 \rightarrow \rho^- K^+\pi^0) < 14 \times 10^{-6}$ at 90% C.L.

Now back to the nominal fit, we include this non-resonance as a new class of background with the yield fixed to the value calculated from the above upper limit and selection efficiency, which is 10 events. The signal yield changes by less than one event. Thus we conclude that the non-resonance contribution from $B^0 \rightarrow \rho^- K^+ \pi^0$ is negligible. The contributions of other non-resonances are much smaller than $B^0 \rightarrow \rho^- K^+ \pi^0$.

In this study, we have ignored the interference effects between the resonance and non-resonance in the fit.

3.8.11 Summary of the Systematic Uncertainties

Table 3.13 summarizes the systematic uncertainties contributing to the $B^0 \rightarrow \rho^- K^{*+}$ signal yield and f_L measurement in the fit. Numbers shown in bold face represent the largest single contributions.

Source	N_{signal}	f_L
Fit systematics (in Events)		
SCF fraction	+1.98 -1.48	+0.028 -0.027
PDFs Parametrizations	1.23	0.046
R (Efficiency ratio)	0.29	0.012
B background uncertainties	1.67	0.029
Fit bias	4.2	0.009
Subtotal	5.1	0.06
Scaling systematics [%]		
Tracking Corrections	2.4	-
Neutral Corrections	10.3	-
$N_{B\bar{B}}$	1.1	-
PID	1.1	-
Subtotal	10.7%	-

Table 3.13: *A Summary of the systematic uncertainties contributing to N_{signal} and f_L .*

3.9 Results and Summary

We have presented the preliminary measurement of the branching ratio and the longitudinal polarization fraction for the decay $B^0 \rightarrow \rho^- K^{*+}$ using a ML fit technique and a total integrated luminosity of 112.5 fb^{-1} data samples, corresponding to ~ 122.7 million $B\bar{B}$ pairs, taken on the $\Upsilon(4S)$ peak during the 1999–2003 period. We obtain $n_{sig} = 55.8 \pm 16.1(\text{stat}) \pm 5.1(\text{syst})$ and $f_L = 0.27 \pm 0.31(\text{stat}) \pm 0.06(\text{syst})$.

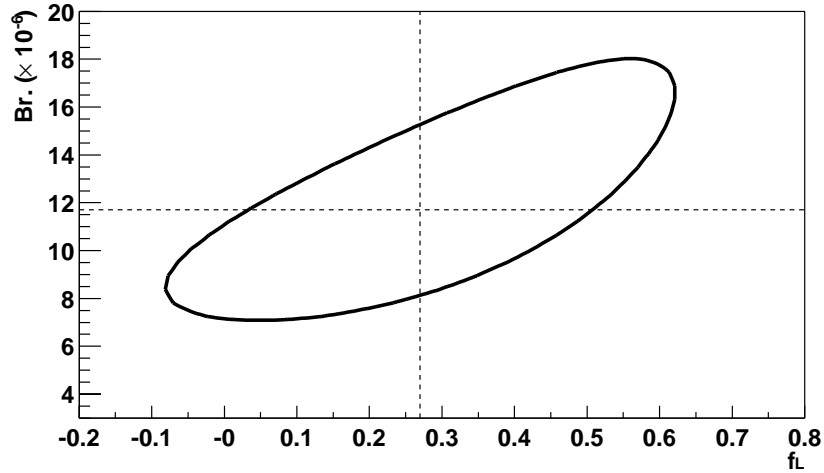


Figure 3.18: *Contour at 1σ level showing the correlated statistical uncertainties on the branching ratio and the longitudinal polarization fraction.*

From the fitted signal yield, the fraction of longitudinal polarization, the selection efficiencies for the longitudinal and transverse polarization components, and the branching ratios $\mathcal{B}(K^{*+} \rightarrow K^+ \pi^0)$, $\mathcal{B}(\pi^0 \rightarrow \gamma\gamma)$, we may calculate the branching ratio for the decay $B^0 \rightarrow \rho^- K^{*+}$, or we may extract it directly from the ML fit, taking the correlation between the branching ratio and f_L into account. We get

$$\mathcal{B} = [11.8_{-4.3}^{+5.0}(\text{stat}) \pm 1.7(\text{syst})] \times 10^{-6}. \quad (3.16)$$

Figure 3.18 shows the error ellipse for the longitudinal polarization fraction and the branching

ratio at one σ level.

The significance of the signal yield relative to zero is 4.2σ . Taking the systematic uncertainty and the correlation between the signal yield and the f_L into account, we quote the measurement of the branching ratio as an upper limit. Figure 3.19 shows the likelihood scan curve to extract the 90% confidence level upper limit, taken to be the branching ratio below which lies 90% of the likelihood integral over the positive branching ratio region. We get

$$\mathcal{B} < 17.2 \times 10^{-6} \quad (90\% \text{ C.L.}). \quad (3.17)$$

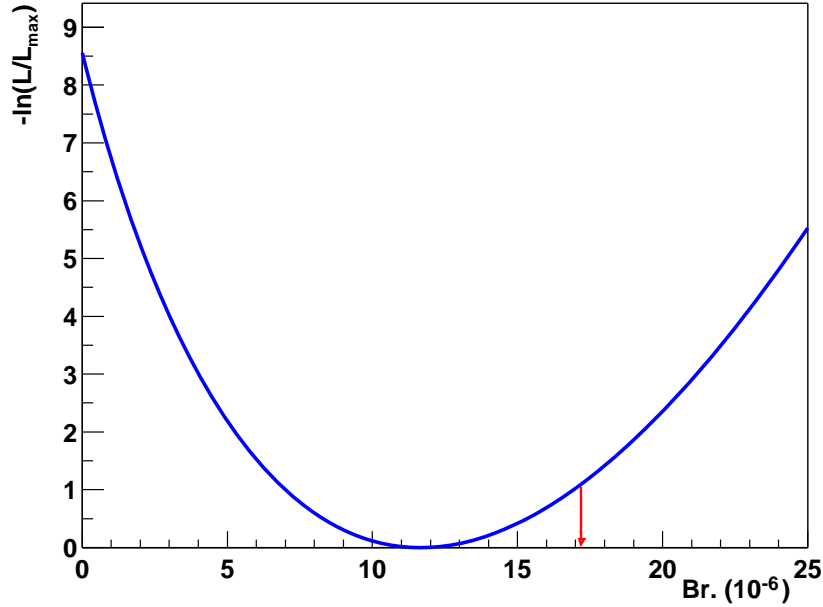


Figure 3.19: *Plot of likelihood curve to extract the upper limit of the branching ratio, indicated by the arrow.*

Our fit result shows the longitudinal polarization fraction of $B^0 \rightarrow \rho^- K^{*+}$ decay differs from one but with larger errors, which is different from other $B \rightarrow \rho K^*$ modes [16]. The upper limit of the branching ratio we get is consistent with theoretical predictions [8]. With more data available in the near future, as well as by including the other signal decay modes,

where $K^{*+} \rightarrow K_S^0 \pi^+$ and $K_S^0 \rightarrow \pi^+ \pi^-$, a definite measurement can be achieved for both the branching ratio and the longitudinal polarization fraction.

Appendix A

Charmless B Decay modes

Decay mode	Br. ($\times 10^{-6}$)	Eff. (%)	Expected yields	Total events
$B^0 \rightarrow K^{*+}(K^+\pi^0)\rho^-_{[\text{Lg.}]}$	$3.3 \pm 3.3\star$	6.84	$27.69 \pm 27.69^\dagger$	89,500
$B^0 \rightarrow K^{*+}(K^+\pi^0)\rho^-_{[\text{Tr.}]}$	$3.3 \pm 3.3\star$	13.88	$56.20 \pm 56.20^\dagger$	70,000
$B^0 \rightarrow K^{*+}(K_s\pi^+)\rho^-_{[\text{Lg.}]}$	$3.3 \pm 3.3\star$	0.006	0.02 ± 0.02	67,000
$B^0 \rightarrow K^{*+}(K_s\pi^+)\rho^-_{[\text{Tr.}]}$	$3.3 \pm 3.3\star$	0.002	0.01 ± 0.01	67,000
$B^0 \rightarrow K^{*0}(K^+\pi^-)\rho^0_{[\text{Lg.}]}$	$3.3 \pm 3.3\star$	0.040	0.16 ± 0.16	85,500
$B^0 \rightarrow K^{*0}(K^+\pi^-)\rho^0_{[\text{Tr.}]}$	$3.3 \pm 3.3\star$	0.027	0.11 ± 0.11	67,000
$B^0 \rightarrow K^{*0}(K^+\pi^-)K^{*0}(K^+\pi^-)_{[\text{Lg.}]}$	9.8 ± 9.8	0.009	0.11 ± 0.11	63,000
$B^0 \rightarrow K^{*0}(K^+\pi^-)K^{*0}(K^+\pi^-)_{[\text{Tr.}]}$	0 ± 0	0.009	0.0 ± 0.0	64,000
$B^0 \rightarrow K^{*0}(K^+\pi^-)\pi^0$	$2.3 \pm 2.3\star$	0.115	0.32 ± 0.32	191,000
$B^0 \rightarrow K^{*0}(K_s\pi^0)\pi^0$	$0.6 \pm 0.6\star$	0.019	0.01 ± 0.01	114,000
$B^0 \rightarrow K^{*+}(K^+\pi^0)\pi^-$	$5.1^{+1.4}_{-1.2}$	0.067	$0.42^{+0.11}_{-0.10}$	191,000
$B^0 \rightarrow K^{*+}(K_s\pi^+)\pi^-$	$5.1^{+1.4}_{-1.2}$	0.012	0.07 ± 0.02	85,500
$B^0 \rightarrow K^{*-}(K^-\pi^0)K^+$	$0 \pm 10\star$	0.070	0.86 ± 0.86	61,000
$B^0 \rightarrow K^{*-}(K_s\pi^-)K^+$	$0 \pm 10\star$	0.219	0.0 ± 2.69	62,000
$B^0 \rightarrow K^{*+}(K^+\pi^0)K^-$	$0 \pm 10\star$	0.085	0.0 ± 1.04	54,000
$B^0 \rightarrow K^{*+}(K_s\pi^+)K^-$	$0 \pm 10\star$	0.194	0.0 ± 2.38	66,000
$B^0 \rightarrow K^{*0}(K^+\pi^-)K_s$	$20 \pm 20\star$	0.027	0.67 ± 0.67	66,000
$B^0 \rightarrow K^{*0}(K_s\pi^0)K_s$	$5.0 \pm 5.0\star$	0.006	0.04 ± 0.04	116,000
$B^0 \rightarrow K^{*0}(K^+\pi^-)f_0(980)(\pi^+\pi^-)$	$22 \pm 22\star$	0.031	0.84 ± 0.84	16,000
$B^0 \rightarrow (K^{**})([\text{anything}])\pi^0$	$72 \pm 72\star$	0.146	$12.89 \pm 12.89^\dagger$	214,000
$B^0 \rightarrow (K^{**})([\text{anything}])\rho^0$	$20 \pm 20\star$	0.196	$4.82 \pm 4.82^\dagger$	29,000

Table A.1: *The first part of the exclusive B decay modes list studied in this analysis. Those modes with a \dagger on the expected yield are included in our fit. The branching ratios with a \star are estimated from theoretical arguments.*

Decay mode	Br. ($\times 10^{-6}$)	Eff. (%)	Expected yields	Total events
$B^0 \rightarrow \rho^+ \rho^-_{[\text{Lg.}]}$	$26.6^{+8.2}_{-8.9}$	0.156	$5.10^{+1.57}_{-1.70}$	365,000
$B^0 \rightarrow \rho^+ \rho^-_{[\text{Tr.}]}$	0 ± 0	0.333	0.0 ± 0.0	63,000
$B^0 \rightarrow \rho^0 \rho^0_{[\text{Lg.}]}$	2.1 ± 2.1	0.007	0.02 ± 0.02	82,500
$B^0 \rightarrow \rho^0 \rho^0_{[\text{tran}]}$	0 ± 0	0.008	0.0 ± 0.0	64,000
$B^0 \rightarrow a_1^+ ((\rho\pi)^+) \pi^-$	$35 \pm 35^*$	0.005	0.20 ± 0.20	107,000
$B^0 \rightarrow a_1^+ (\rho^0 \pi^+) \rho^-_{[\text{Lg.}]}$	$20 \pm 20^*$	0.005	0.12 ± 0.12	40,000
$B^0 \rightarrow a_1^+ (\rho^+ \pi^0) \rho^-_{[\text{Lg.}]}$	$20 \pm 20^*$	0.067	$1.66 \pm 1.66^\dagger$	40,000
$B^0 \rightarrow a_1^+ (\rho^+ \pi^0) \rho^-_{[\text{Tr.}]}$	$20 \pm 20^*$	0.020	0.49 ± 0.49	40,000
$B^0 \rightarrow K^{*0} (K^+ \pi^-) \pi^0 \pi^0_{[\text{nonres}]}$	$0 \pm 10^*$	0.123	0.0 ± 1.51	30,000
$B^0 \rightarrow K^{*0} (K^+ \pi^-) \pi^+ \pi^-_{[\text{nonres}]}$	$0 \pm 10^*$	0.017	0.0 ± 0.20	54,000
$B^0 \rightarrow K^{*0} (K^+ \pi^-) \rho^0 \pi^0_{[\text{nonres}]}$	$0 \pm 10^*$	0.007	0.0 ± 0.08	30,000
$B^0 \rightarrow K^{*0} (K^+ \pi^-) \rho^- \pi^+_{[\text{nonres}]}$	$0 \pm 10^*$	0.013	0.0 ± 0.16	30,000
$B^0 \rightarrow \rho^0 a_0^0 (\eta \pi^0)$	$20 \pm 20^*$	0.001	0.04 ± 0.04	63,000
$B^0 \rightarrow \rho^- a_0^+ (\eta \pi^+)$	$20 \pm 20^*$	0.023	0.57 ± 0.57	65,000
$B^0 \rightarrow \rho^+ a_0^- (\eta \pi^-)$	$20 \pm 20^*$	0.015	0.38 ± 0.38	64,000
$B^0 \rightarrow \rho^0 K_s$	6.0 ± 6.0	0.009	0.07 ± 0.07	64,000
$B^0 \rightarrow \rho^+ \pi^-$	24.0 ± 2.5	0.007	0.20 ± 0.02	540,000
$B^0 \rightarrow \rho^0 \pi^0$	2.5 ± 2.5	0.010	0.03 ± 0.03	486,500
$B^0 \rightarrow \eta (\gamma \gamma) \eta (\pi^0 \pi^+ \pi^-)$	$1.0 \pm 1.0^*$	0.0	0.0 ± 0.0	67,000
$B^0 \rightarrow \eta (\text{anything}) K^+ K^-_{[\text{nonres}]}$	$0 \pm 10^*$	0.028	0.0 ± 0.34	65,000
$B^0 \rightarrow \eta (\text{anything}) K^+ \pi^-_{[\text{nonres}]}$	$0 \pm 10^*$	0.068	0.0 ± 0.84	63,000
$B^0 \rightarrow \eta (\text{anything}) \pi^+ \pi^-_{[\text{nonres}]}$	$0 \pm 10^*$	0.001	0.0 ± 0.02	64,000
$B^0 \rightarrow \eta (3\pi) \rho^0$	3.0 ± 3.0	0.003	0.01 ± 0.01	64,000
$B^0 \rightarrow \eta (\gamma \gamma) \rho^0$	2.2 ± 2.2	0.003	0.01 ± 0.01	65,000
$B^0 \rightarrow \eta' (\eta \pi \pi) \eta (\gamma \gamma)$	$1.0 \pm 1.0^*$	0.0	0.0 ± 0.0	56,000
$B^0 \rightarrow \eta' (\rho^0 \gamma) \eta (3\pi)$	$1.0 \pm 1.0^*$	0.001	0.0 ± 0.0	64,000
$B^0 \rightarrow \eta' (\rho^0 \gamma) \eta (\gamma \gamma)$	$1.0 \pm 1.0^*$	0.003	0.0 ± 0.0	70,000

Table A.2: The second part of the exclusive B decay modes list (see caption of Table A.1).

Decay mode	Br. ($\times 10^{-6}$)	Eff. (%)	Expected yields	Total events
$B^0 \rightarrow \omega(\pi^+\pi^-\pi^0)\eta$ [anything]	$0.0 \pm 3.3\star$	0.0	0.0 ± 0.0	67,000
$B^0 \rightarrow \omega(\pi^+\pi^-\pi^0)\omega(\pi^+\pi^-\pi^0)$ [Lg.]	$0.0 \pm 3.3\star$	0.001	0.0 ± 0.01	67,000
$B^0 \rightarrow \omega(\pi^+\pi^-\pi^0)\omega(\pi^+\pi^-\pi^0)$ [Tr.]	$0.0 \pm 3.3\star$	0.001	0.0 ± 0.01	67,000
$B^0 \rightarrow \omega(\pi^+\pi^-\pi^0)\phi(K^+K^-)$ [Tr.]	$0.0 \pm 3.3\star$	0.0	0.0 ± 0.0	67,000
$B^0 \rightarrow \omega(\pi^+\pi^-\pi^0)\pi^+\pi^-$ [nonres]	$0.0 \pm 3.3\star$	0.003	0.0 ± 0.01	30,000
$B^0 \rightarrow \omega(\pi^+\pi^-\pi^0)\rho^0$ [Lg.]	$11.0 \pm 11.0\star$	0.001	0.02 ± 0.02	66,000
$B^0 \rightarrow \phi(K^+K^-)K^{*0}(K^+\pi^-)$ [Lg.]	3.6 ± 0.4	0.001	0.01 ± 0.00	65,000
$B^0 \rightarrow \phi(K^+K^-)\pi^0$	$0.0 \pm 3.0\star$	0.058	0.0 ± 0.21	67,000
$B^0 \rightarrow \phi(K^+K^-)\rho^0$ [Lg.]	$0.0 \pm 3.0\star$	0.009	0.0 ± 0.03	66,000
$B^0 \rightarrow K^+K^-\pi^0$ [nonres]	$0 \pm 10\star$	0.132	0.0 ± 1.62	66,000
$B^0 \rightarrow K^+\pi^-\pi^0$ [nonres]	$10 \pm 10\star$	0.097	1.19 ± 1.19	152,000
$B^0 \rightarrow K_s K^+ K^-$ [nonres]	$0 \pm 10\star$	0.034	0.0 ± 0.41	1,346,000
$B^0 \rightarrow K_s K^+ \pi^-$ [nonres]	$0 \pm 10\star$	0.069	0.0 ± 0.85	1,218,000
$B^0 \rightarrow K_s K^- \pi^+$ [nonres]	$0 \pm 10\star$	0.069	0.0 ± 0.85	1,215,000
$B^0 \rightarrow (K_s K_s K_s)$ [nonres]	$0 \pm 10\star$	0.001	0.0 ± 0.01	120,000
$B^0 \rightarrow K_s \pi^+ \pi^-$ [nonres]	$0 \pm 10\star$	0.003	0.0 ± 0.04	972,000
$B^0 \rightarrow \pi^+ \pi^- \pi^0$ [nonres]	$0 \pm 10\star$	0.006	0.0 ± 0.08	987,000
$B^0 \rightarrow \pi^+ \pi^- \pi^0 \pi^0$ [nonres]	$0 \pm 10\star$	0.021	0.0 ± 0.26	14,000
$B^0 \rightarrow \rho^0 \pi^0 \pi^0$ [nonres]	$0 \pm 10\star$	0.003	0.0 ± 0.04	30,000
$B^0 \rightarrow \rho^0 \pi^+ \pi^-$ [nonres]	$0 \pm 10\star$	0.0	0.0 ± 0.0	54,000
$B^0 \rightarrow \rho^0 \rho^- \pi^+$ [nonres]	$0 \pm 10\star$	0.003	0.0 ± 0.04	30,000
$B^0 \rightarrow \rho^0 \rho^+ \pi^-$ [nonres]	$0 \pm 10\star$	0.0	0.0 ± 0.0	30,000
$B^0 \rightarrow \rho^+ \pi^- \pi^0$ [nonres]	$0 \pm 10\star$	0.022	0.0 ± 0.27	54,000
$B^0 \rightarrow \rho^+ \rho^- \pi^0$ [nonres]	$0 \pm 10\star$	0.010	0.0 ± 0.12	30,000

Table A.3: *The third part of the exclusive B decay modes list (see caption of Table A.1).*

Decay mode	Br. ($\times 10^{-6}$)	Eff. (%)	Expected yields	Total events
$B^+ \rightarrow \rho^+ \rho_{[\text{Lg.}]}^0$	26.4 ± 6.2	0.018	0.60 ± 0.14	232,000
$B^+ \rightarrow \rho^+ \rho_{[\text{Tr.}]}^0$	0 ± 0	0.009	0.0 ± 0.0	64,000
$B^+ \rightarrow a_1^+ ((\rho\pi)^+) \pi^0$	$17.5 \pm 17.5^*$	0.024	0.51 ± 0.51	20,000
$B^+ \rightarrow a_1^0 ((\rho\pi)^0) \pi^+$	$17.5 \pm 17.5^*$	0.011	0.24 ± 0.24	44,000
$B^+ \rightarrow a_1^0 ((\rho\pi)^0) \rho_{[\text{Lg.}]}^+$	$20 \pm 20^*$	0.027	0.67 ± 0.67	40,000
$B^+ \rightarrow a_1^0 ((\rho\pi)^0) \rho_{[\text{Tr.}]}^+$	$20 \pm 20^*$	0.020	0.49 ± 0.49	40,000
$B^+ \rightarrow (K^{(**)} ([\text{anything}]) \pi)^+$	$40 \pm 40^*$	0.051	$2.52 \pm 2.52^\dagger$	104,000
$B^+ \rightarrow (K^{(**)} ([\text{anything}]) \rho)^+$	$15 \pm 15^*$	0.139	$2.55 \pm 2.55^\dagger$	36,000
$B^+ \rightarrow \eta(\gamma\gamma) K^+$	1.28 ± 0.28	0.009	0.01 ± 0.0	67,000
$B^+ \rightarrow \eta(\gamma\gamma) \pi^+$	1.68 ± 0.36	0.0	0.0 ± 0.0	67,000
$B^+ \rightarrow \eta(3\pi) \rho^+$	4.89 ± 1.54	0.003	0.02 ± 0.01	67,000
$B^+ \rightarrow \eta(\gamma\gamma) \rho^+$	3.56 ± 1.12	0.009	0.04 ± 0.01	67,000
$B^+ \rightarrow \eta(3\pi) K^{*+} (K^+ \pi^0)$	4.75 ± 0.64	0.026	0.15 ± 0.02	61,000
$B^+ \rightarrow \eta(3\pi) K^{*+} (K_s \pi^+)$	4.75 ± 0.64	0.0	0.0 ± 0.0	63,000
$B^+ \rightarrow \eta(\gamma\gamma) K^{*+} (K^+ \pi^0)$	3.45 ± 0.47	0.130	0.55 ± 0.07	67,000
$B^+ \rightarrow \eta(\gamma\gamma) K^{*+} (K_s \pi^+)$	3.45 ± 0.47	0.001	0.01 ± 0.00	67,000
$B^+ \rightarrow \eta'(\eta\pi^+ \pi^-) K^+$	13.66 ± 0.81	0.031	0.52 ± 0.03	67,000
$B^+ \rightarrow \eta'(\rho^0 \gamma) K^+$	22.89 ± 1.36	0.092	$2.59 \pm 0.15^\dagger$	84,500
$B^+ \rightarrow \eta'(\eta\pi^+ \pi^-) K^{*+} (K^+ \pi^0)$	0.7 ± 0.7	0.012	0.01 ± 0.01	65,000
$B^+ \rightarrow \eta'(\rho^0 \gamma) K^{*+} (K^+ \pi^0)$	1.16 ± 1.16	0.314	0.45 ± 0.45	64,000
$B^+ \rightarrow \eta'(\rho^0 \gamma) K^{*+} (K_s \pi^+)$	1.16 ± 1.16	0.0	0.0 ± 0.0	65,000
$B^+ \rightarrow \eta'(\eta\pi^+ \pi^-) \pi^+$	1.16 ± 1.16	0.0	0.0 ± 0.0	67,000
$B^+ \rightarrow \eta'(\rho^0 \gamma) \pi^+$	1.3 ± 1.3	0.002	0.00 ± 0.00	67,000
$B^+ \rightarrow \eta'(\eta\pi^+ \pi^-) \rho^+$	2.34 ± 0.89	0.006	0.02 ± 0.01	63,000
$B^+ \rightarrow \eta'(\rho^0 \gamma) \rho^+$	3.86 ± 1.50	0.014	0.06 ± 0.02	65,000
$B^+ \rightarrow \rho^0 a_0^+ (\eta\pi^+)$	$20 \pm 20^*$	0.005	0.12 ± 0.12	63,000
$B^+ \rightarrow \rho^0 K^+$	4.1 ± 0.8	0.021	0.10 ± 0.02	135,000
$B^+ \rightarrow \rho^0 \pi^+$	9.1 ± 1.1	0.0	0.0 ± 0.0	121,000
$B^+ \rightarrow \rho^+ K_s$	$4.0 \pm 3.0^*$	0.019	0.09 ± 0.07	347,000
$B^+ \rightarrow \rho^+ \pi^0$	11.0 ± 2.7	0.019	0.25 ± 0.06	711,000

Table A.4: The fourth part of the exclusive B decay modes list (see caption of Table A.1).

Decay mode	Br. ($\times 10^{-6}$)	Eff. (%)	Expected yields	Total events
$B^+ \rightarrow K^{*+}(K^+\pi^0)K_s$	$0 \pm 3.0^*$	0.376	0.0 ± 1.39	64,000
$B^+ \rightarrow K^{*+}(K_s\pi^+)K_s$	$0 \pm 3.0^*$	0.003	0.0 ± 0.01	62,000
$B^+ \rightarrow K^{*+}(K^+\pi^0)\bar{K}^{*0}(K^-\pi^+)$ [Lg.]	$15.8 \pm 15.8^*$	0.200	$3.88 \pm 3.88^\dagger$	66,000
$B^+ \rightarrow K^{*+}(K^+\pi^0)\bar{K}^{*0}(K^-\pi^+)$ [Tr.]	$15.8 \pm 15.8^*$	0.192	$3.73 \pm 3.73^\dagger$	66,000
$B^+ \rightarrow K^{*+}(K_s\pi^+)\bar{K}^{*0}(K^-\pi^+)$ [Lg.]	$15.8 \pm 15.8^*$	0.035	0.69 ± 0.69	62,000
$B^+ \rightarrow K^{*0}(K^+\pi^-)a_0^+(\eta\pi^+)$	$0 \pm 5^*$	0.009	0.06 ± 0.06	65,000
$B^+ \rightarrow \bar{K}^{*0}(\bar{K}_s\pi^0)K^+$	$2.6 \pm 2.6^*$	0.003	0.01 ± 0.01	64,000
$B^+ \rightarrow K^{*+}(K^+\pi^0)\pi^0$	$4.4 \pm 2.5^*$	1.263	$6.82 \pm 3.87^\dagger$	101,000
$B^+ \rightarrow K^{*+}(K_s\pi^+)\pi^0$	$4.4 \pm 2.5^*$	0.022	0.12 ± 0.07	66,000
$B^+ \rightarrow K^{*0}(K^+\pi^-)\pi^+$	6.00 ± 0.87	0.001	0.01 ± 0.00	123,000
$B^+ \rightarrow K^{*0}(K_s\pi^0)\pi^+$	1.5 ± 0.22	0.006	0.01 ± 0.00	62,000
$B^+ \rightarrow K^{*0}(K^+\pi^-)\rho^+$ [Lg.]	$14.1 \pm 5.1^*$	0.113	$1.96 \pm 0.71^\dagger$	673,500
$B^+ \rightarrow K^{*0}(K^+\pi^-)\rho^+$ [Tr.]	$14.1 \pm 5.1^*$	0.020	0.34 ± 0.12	65,000
$B^+ \rightarrow K^{*+}(K^+\pi^0)\rho^0$ [Lg.]	3.5 ± 1.3	0.478	$2.05 \pm 0.76^\dagger$	78,500
$B^+ \rightarrow K^{*+}(K^+\pi^0)\rho^0$ [Tr.]	3.5 ± 1.3	0.331	$1.42 \pm 0.53^\dagger$	67,000
$B^+ \rightarrow K^{*+}(K_s\pi^+)\rho^0$ [Lg.]	3.5 ± 1.3	0.0	0.0 ± 0.0	67,000
$B^+ \rightarrow K^{*+}(K_s\pi^+)\rho^0$ [Tr.]	3.5 ± 1.3	0.001	0.01 ± 0.00	66,000
$B^+ \rightarrow K^{*+}(K^+\pi^0)f_0(980)(\pi^+\pi^-)$	$0 \pm 3.0^*$	0.306	0.0 ± 1.12	50,000
$B^+ \rightarrow K^{*0}(K^+\pi^-)\pi^+\pi^-$ [nonres]	$0 \pm 10^*$	0.015	0.0 ± 0.18	54,000
$B^+ \rightarrow K^{*+}(K^+\pi^0)\pi^+\pi^-$ [nonres]	$0 \pm 10^*$	0.126	0.0 ± 1.55	53,000
$B^+ \rightarrow K^{*+}(K_s\pi^+)\pi^+\pi^-$ [nonres]	$0 \pm 10^*$	0.002	0.0 ± 0.02	52,000
$B^+ \rightarrow K^{*+}(K^+\pi^0)\rho^0\pi^-$ [nonres]	$0 \pm 10^*$	0.047	0.0 ± 0.57	30,000
$B^+ \rightarrow K^{*+}(K^+\pi^0)\rho^+\pi^-$ [nonres]	$0 \pm 10^*$	0.070	0.0 ± 0.86	30,000
$B^+ \rightarrow K^{*+}(K^+\pi^0)\rho^-\pi^+$ [nonres]	$0 \pm 10^*$	0.053	0.0 ± 0.65	30,000
$B^+ \rightarrow a_0^0(\eta(\gamma\gamma)\pi^0)K^+$	$0.0 \pm 3.0^*$	0.041	0.0 ± 0.15	58,000
$B^+ \rightarrow a_0^0(\eta(\pi\pi\pi^0)\pi^0)K^+$	$0.0 \pm 3.0^*$	0.052	0.0 ± 0.0	59,000
$B^+ \rightarrow a_0^0(\eta(\gamma\gamma)\pi^0)\pi^+$	$0.0 \pm 3.0^*$	0.005	0.0 ± 0.02	58,000
$B^+ \rightarrow a_0^0(\eta(\pi\pi\pi^0)\pi^0)\pi^+$	$0.0 \pm 3.0^*$	0.007	0.0 ± 0.0	58,000
$B^+ \rightarrow a_0^+(\eta(\pi\pi\pi^0)\pi^+)K_s$	$0.0 \pm 3.0^*$	0.0	0.0 ± 0.0	58,000
$B^+ \rightarrow a_0^+(\eta(\gamma\gamma)\pi^+)\pi^0$	$0.0 \pm 3.0^*$	0.010	0.0 ± 0.04	59,000
$B^+ \rightarrow a_0^+(\eta(\pi\pi\pi^0)\pi^+)\pi^0$	$0.0 \pm 3.0^*$	0.008	0.0 ± 0.0	59,000
$B^+ \rightarrow K^{*+}(K^+\pi^0)\mu^+\mu^-$	$0.92^{+0.70}_{-0.58}$	0.061	$0.07^{+0.05}_{-0.04}$	28,000

Table A.5: The fifth part of the exclusive B decay modes list (see caption of Table A.1).

Decay mode	Br. ($\times 10^{-6}$)	Eff. (%)	Expected yields	Total events
$B^+ \rightarrow \omega(\pi^+\pi^-\pi^0)K^+$	4.79 ± 0.71	0.175	1.03 ± 0.15	65,000
$B^+ \rightarrow \omega(\pi^+\pi^-\pi^0)K^{*+}(K^+\pi^0)$ [Lg.]	$10 \pm 10^*$	0.063	0.77 ± 0.77	65,000
$B^+ \rightarrow \omega(\pi^+\pi^-\pi^0)K^{*+}(K^+\pi^0)$ [Tr.]	$10 \pm 10^*$	0.232	$2.85 \pm 2.85^\dagger$	65,000
$B^+ \rightarrow \omega(\pi^+\pi^-\pi^0)K^{*+}(K_s\pi^+)$ [Lg.]	$10 \pm 10^*$	0.0	0.0 ± 0.0	65,000
$B^+ \rightarrow \omega(\pi^+\pi^-\pi^0)K^{*+}(K_s\pi^+)$ [Tr.]	$10 \pm 10^*$	0.001	0.02 ± 0.02	67,000
$B^+ \rightarrow \omega(\pi^+\pi^-\pi^0)\pi^+$	5.23 ± 0.79	0.009	0.06 ± 0.01	65,000
$B^+ \rightarrow \omega(\pi^+\pi^-\pi^0)\rho^+$ [Lg.]	$61 \pm 61^*$	0.009	0.67 ± 0.67	67,000
$B^+ \rightarrow \omega(\pi^+\pi^-\pi^0)\rho^+$ [Tr.]	$61 \pm 61^*$	0.014	1.03 ± 1.03	65,000
$B^+ \rightarrow \omega(\pi^+\pi^-\pi^0)\pi^+\pi^0$ [nonres]	$0 \pm 10^*$	0.007	0.0 ± 0.08	30,000
$B^+ \rightarrow \phi(\pi^+\pi^-\pi^0)K^+$	4.50 ± 0.35	0.366	$2.02 \pm 0.16^\dagger$	67,000
$B^+ \rightarrow \phi(K^+K^-)\pi^+$	$0 \pm 3.0^*$	0.006	0.0 ± 0.02	63,000
$B^+ \rightarrow \phi(K^+K^-)\rho^+$ [Lg.]	$0 \pm 3.0^*$	0.029	0.0 ± 0.11	65,000
$B^+ \rightarrow \phi(K^+K^-)\rho^+$ [Tr.]	$0 \pm 3.0^*$	0.008	0.0 ± 0.03	65,000
$B^+ \rightarrow K^+K^-K^+$ [nonres]	$0 \pm 10^*$	0.020	0.0 ± 0.25	1,190,000
$B^+ \rightarrow K^+K^-\pi^+$ [nonres]	$0 \pm 10^*$	0.036	0.0 ± 0.44	1,214,000
$B^+ \rightarrow K^+K^+\pi^-$ [nonres]	$0 \pm 10^*$	0.100	0.0 ± 1.23	29,000
$B^+ \rightarrow K^+\pi^0\pi^0$ [nonres]	$0 \pm 10^*$	0.216	0.0 ± 2.66	643,000
$B^+ \rightarrow K^+\pi^+\pi^-\pi^0$ [nonres]	$0 \pm 10^*$	0.044	0.0 ± 0.54	29,500
$B^+ \rightarrow K^+\pi^+\pi^-$ [nonres]	$0 \pm 10^*$	0.029	0.0 ± 0.35	1,221,000
$B^+ \rightarrow K_sK^+\pi^0$ [nonres]	$0 \pm 10^*$	0.125	0.0 ± 1.53	64,000
$B^+ \rightarrow K_sK_s\pi^+$ [nonres]	$0 \pm 10^*$	0.002	0.0 ± 0.02	116,000
$B^+ \rightarrow K_s\pi^+\pi^0$ [nonres]	$0 \pm 10^*$	0.003	0.0 ± 0.04	114,000
$B^+ \rightarrow \pi^+\pi^0\pi^0$ [nonres]	$0 \pm 10^*$	0.008	0.0 ± 0.10	542,000
$B^+ \rightarrow \pi^+\pi^-\pi^+\pi^0$ [nonres]	$0 \pm 10^*$	0.003	0.0 ± 0.04	30,000
$B^+ \rightarrow \pi^+\pi^-\pi^+$ [nonres]	$0 \pm 10^*$	0.0	0.0 ± 0.0	55,000
$B^+ \rightarrow \rho^0\pi^+\pi^0$ [nonres]	$0 \pm 10^*$	0.007	0.0 ± 0.09	54,000
$B^+ \rightarrow \rho^-\pi^+\pi^0$ [nonres]	$0 \pm 10^*$	0.126	0.0 ± 1.54	54,000
$B^+ \rightarrow \rho^+\pi^-\pi^+\pi^0$ [nonres]	$0 \pm 10^*$	0.003	0.0 ± 0.04	30,000
$B^+ \rightarrow \rho^+\rho^-\pi^+$ [nonres]	$0 \pm 10^*$	0.004	0.0 ± 0.05	24,000
$B^+ \rightarrow \rho^-\pi^+\pi^+$ [nonres]	$0 \pm 10^*$	0.175	0.0 ± 2.14	4,000
$B^+ \rightarrow \rho^+K^+\pi^-$ [nonres]	$0 \pm 10^*$	0.144	0.0 ± 1.77	54,000
$B^+ \rightarrow \rho^+\pi^+\pi^-$ [nonres]	$0 \pm 10^*$	0.017	0.0 ± 0.20	54,000
$B^+ \rightarrow \rho^+\rho^+\pi^-$ [nonres]	$0 \pm 10^*$	0.003	0.0 ± 0.04	30,000

Table A.6: The sixth part of the exclusive B decay modes list (see caption of Table A.1).

Appendix B

Distributions of the Discriminating Variables

This appendix shows the distributions of the discriminating variables that enter the fit as defined in Section 3.4, with the PDFs overlaid. All B -background shapes are parametrized by KEYS. See Figure 3.6 for more information.

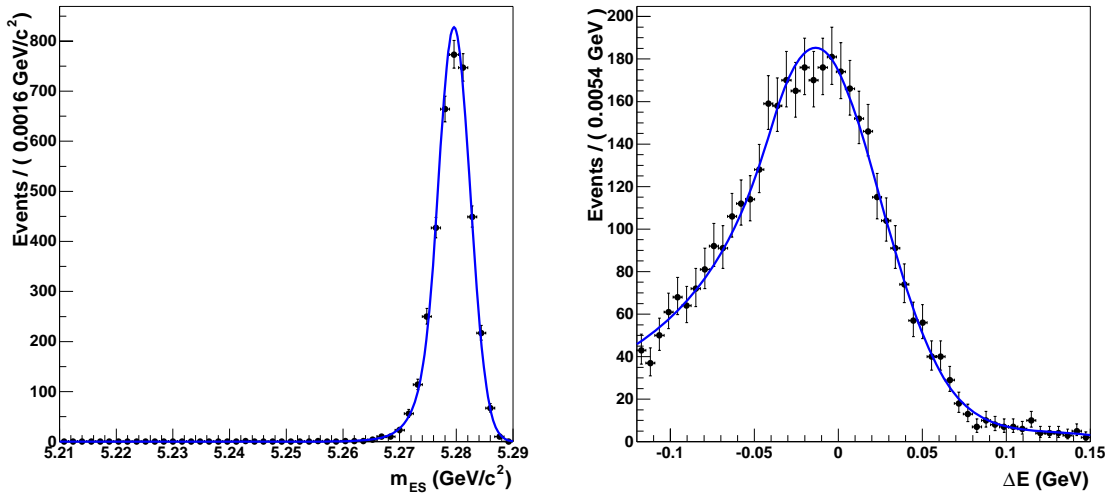


Figure B.1: m_{ES} and ΔE PDFs for TM signal $B^0 \rightarrow \rho^- K^{*+}$.

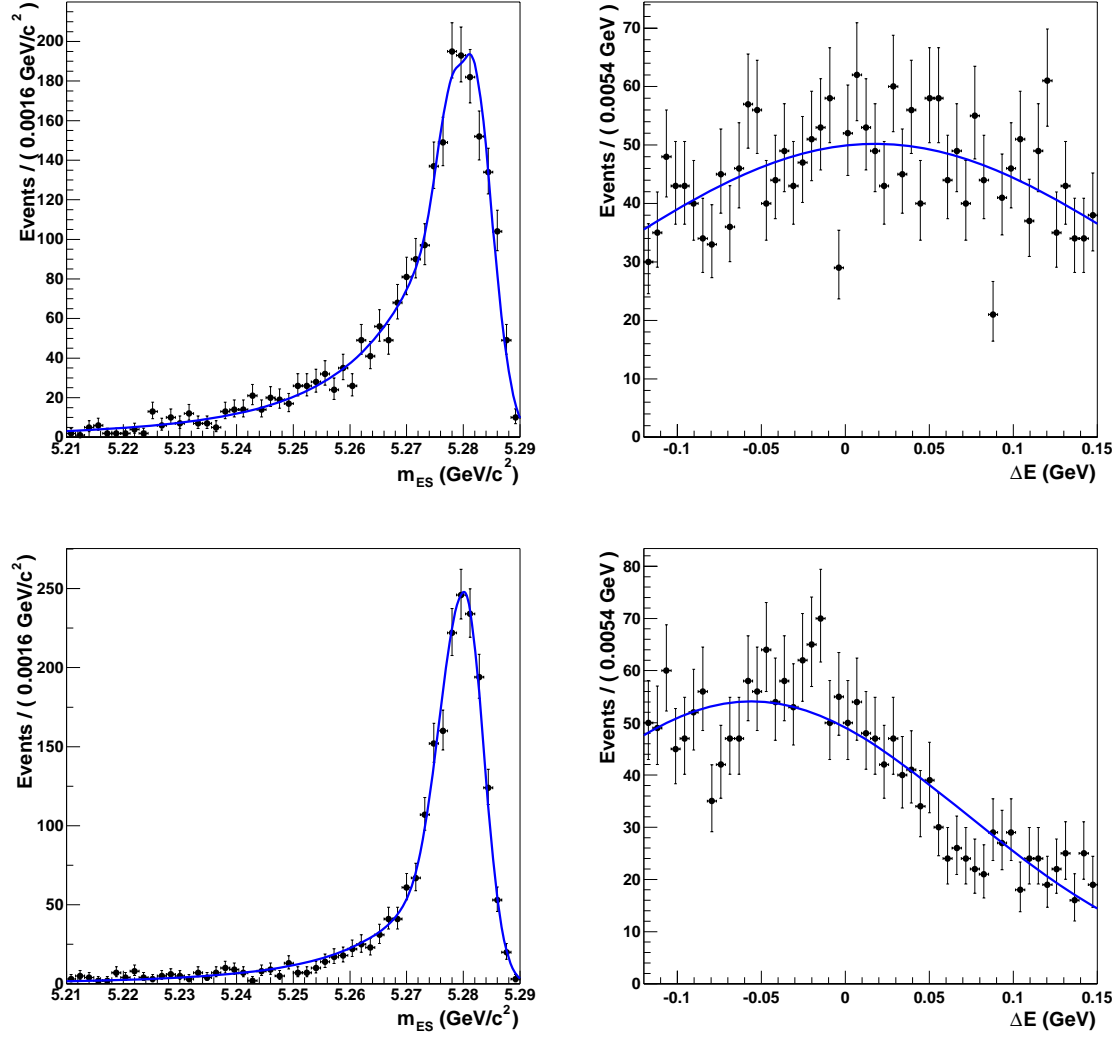


Figure B.2: m_{ES} and ΔE PDFs for SCF signal MC, longitudinal (upper) and transverse (lower) respectively.

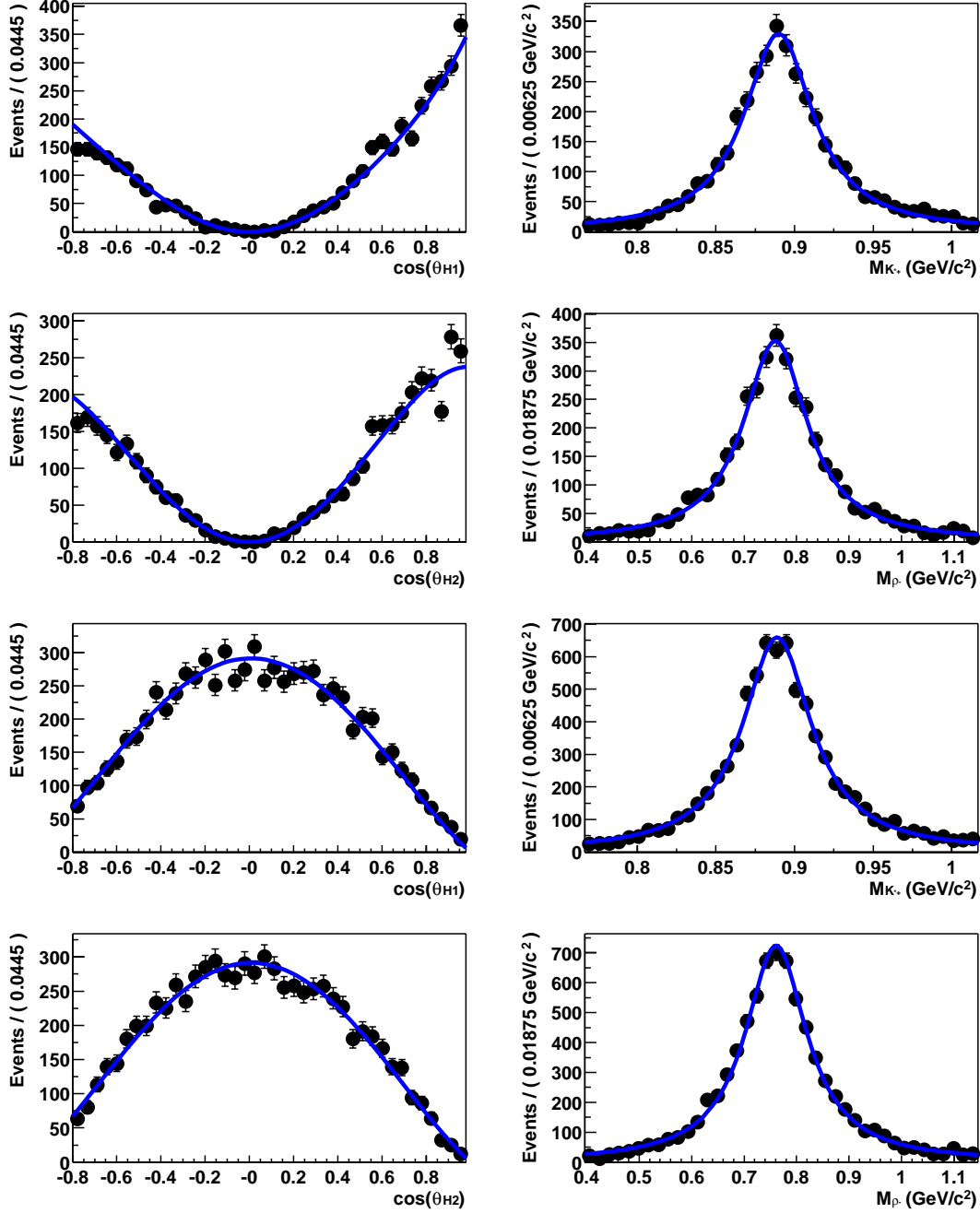


Figure B.3: *TM* signal PDFs for helicities (left) and vector masses (right), longitudinal (upper two) and transverse (lower two) respectively.

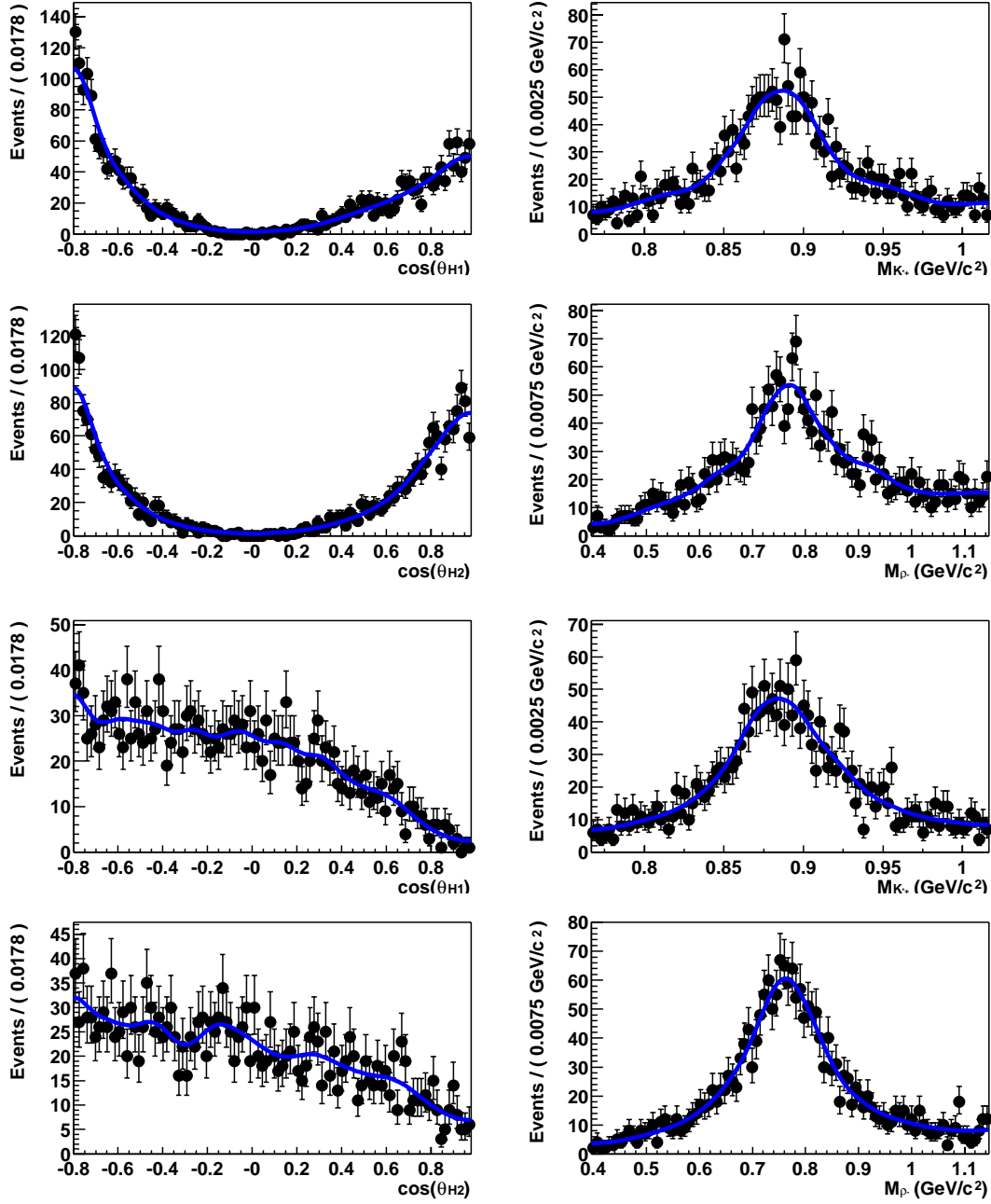


Figure B.4: The SCF PDFs for helicities (left) and vector masses (right), longitudinal (upper two) and transverse (lower two) respectively.

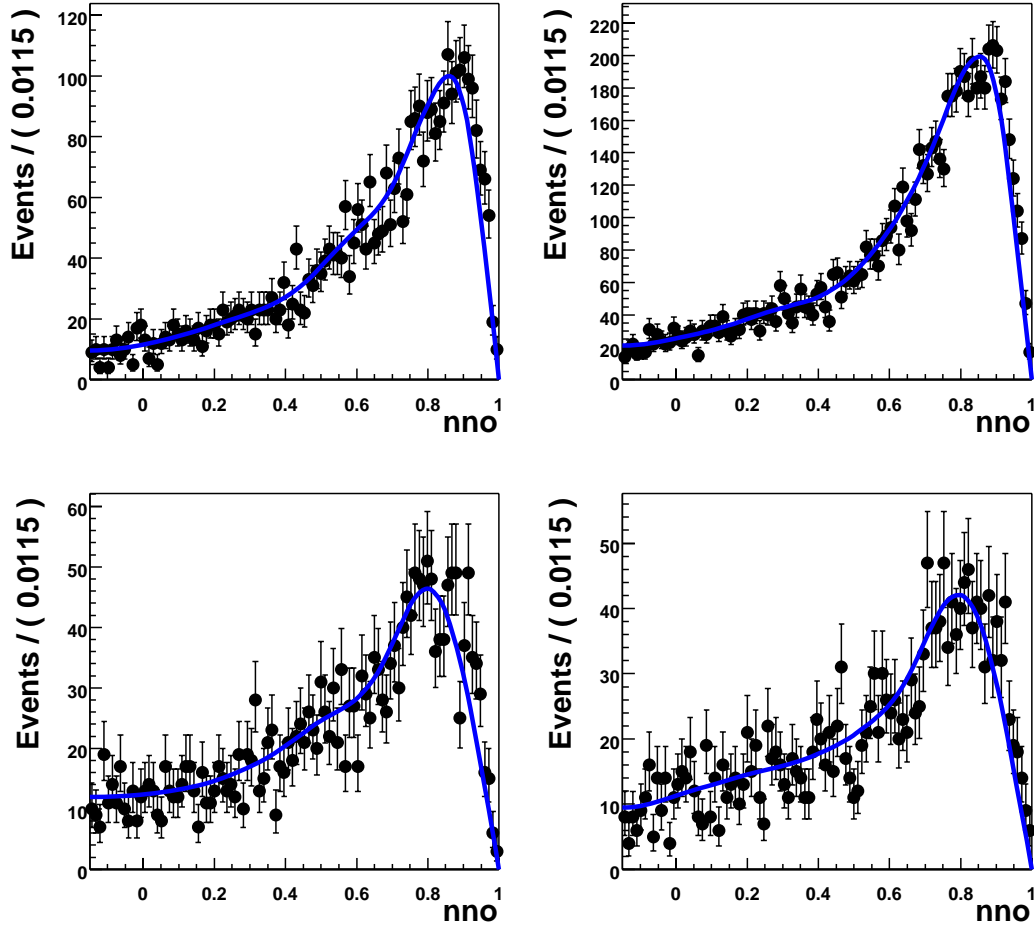


Figure B.5: NN PDFs for the longitudinal (left) and transverse (right) signal, TM (upper) and SCF (lower) respectively. They are parameterized by KEYs.

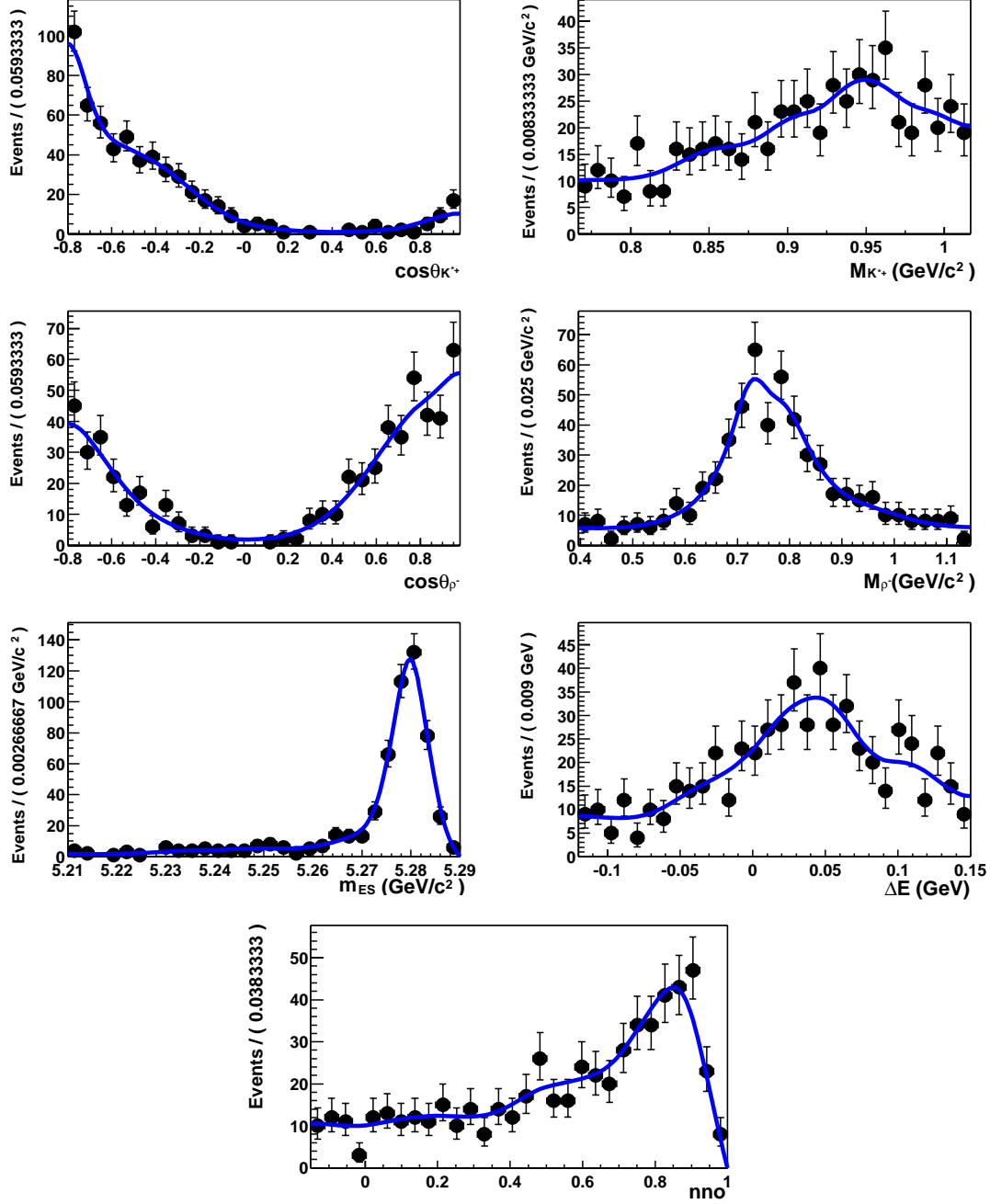


Figure B.6: Distributions of discriminating variables for the B -background class 0, $B^0 \rightarrow \rho^+ \rho^-_{[long]}$. Upper 2 plots are K^* helicity and mass PDFs. The 2 plots in second row are ρ helicity and mass PDFs. The lower three plots are m_{ES} , ΔE and nno PDFs respectively.

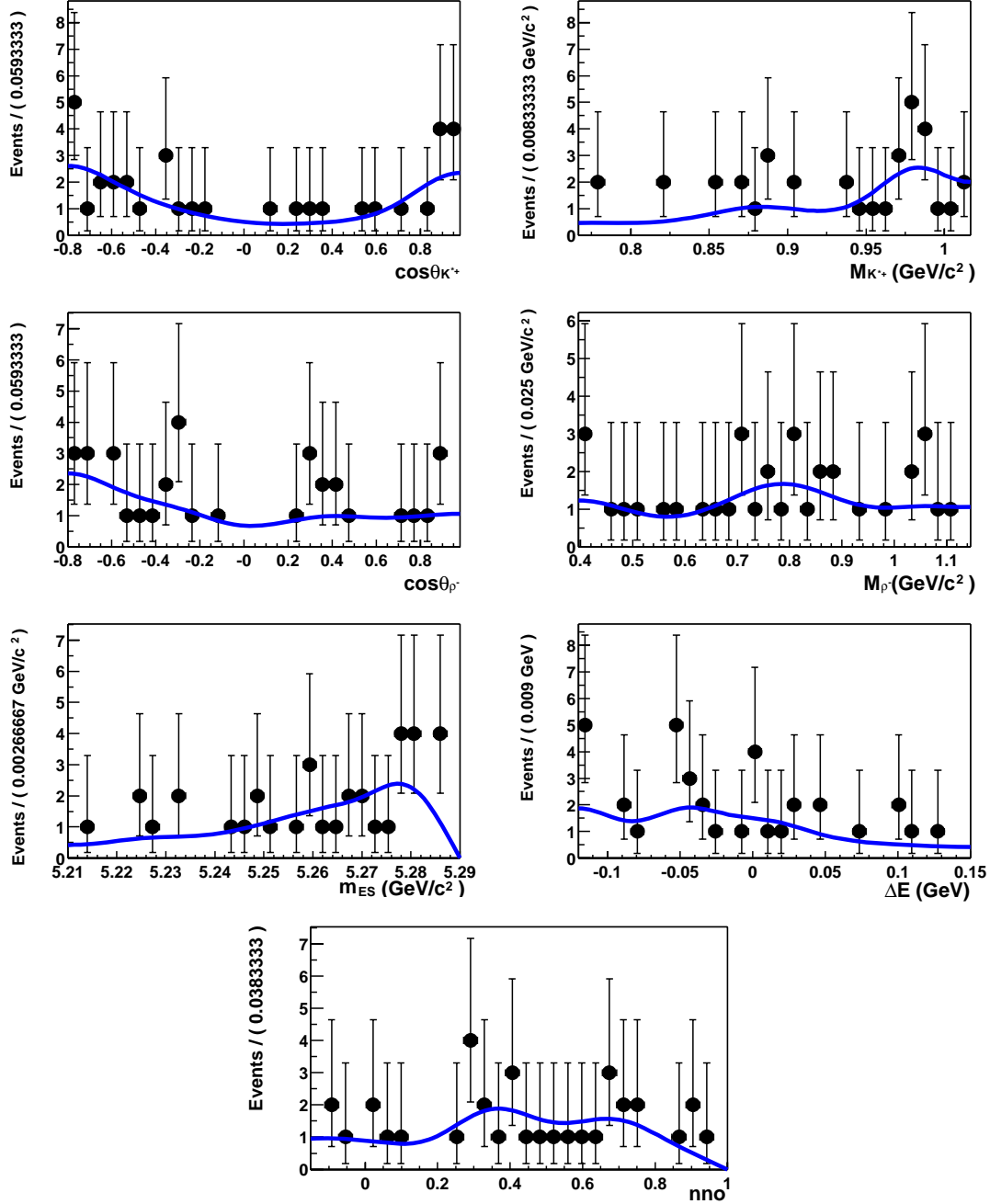


Figure B.7: *Distributions of discriminating variables for the B -background class 1, $B^0 \rightarrow a_1^+ \rho^-$. See Figure B.6 for description.*

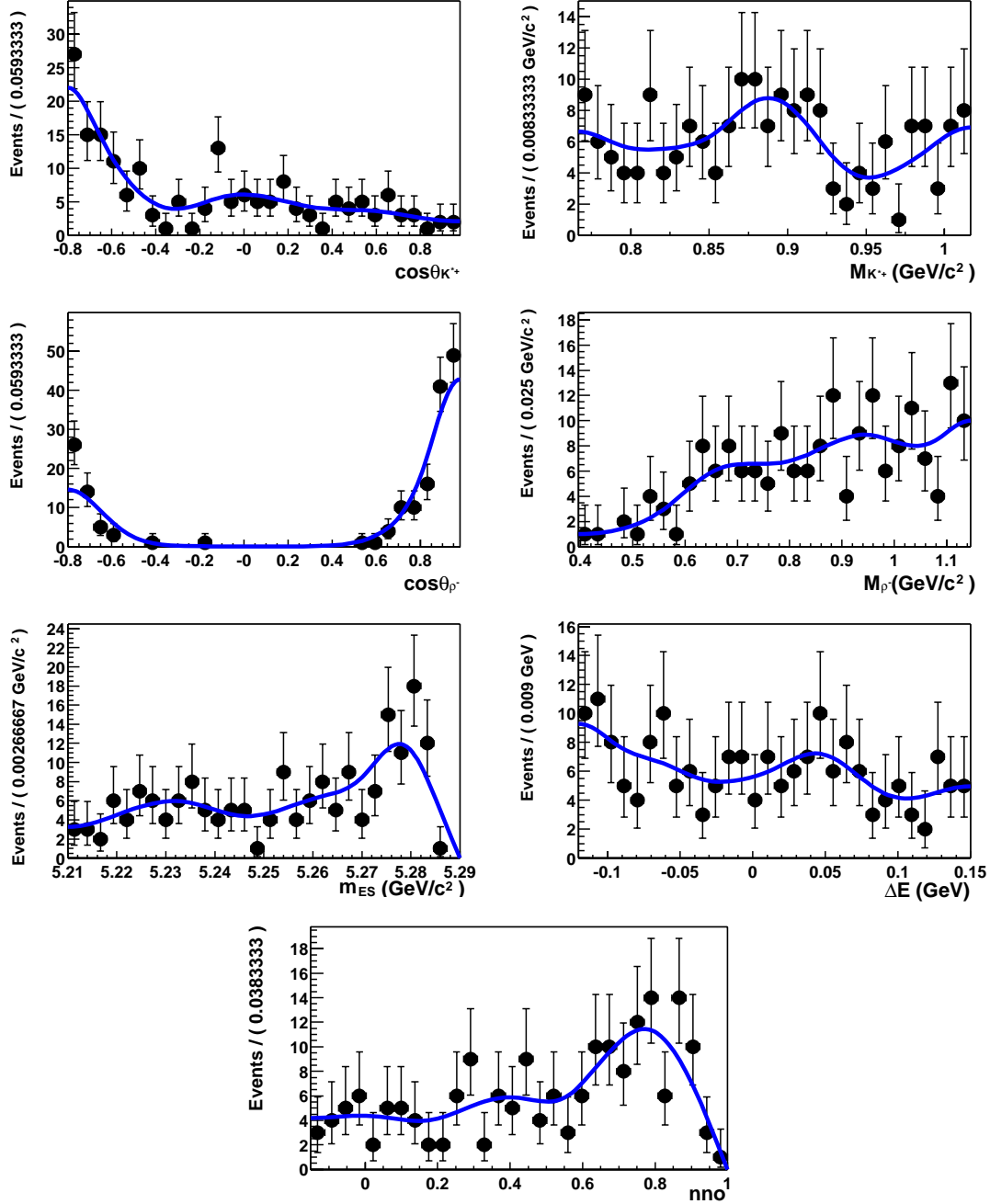


Figure B.8: *Distributions of discriminating variables for the B -background class 2, $B^0 \rightarrow (K^{**}\pi)^0$. See Figure B.6 for description.*

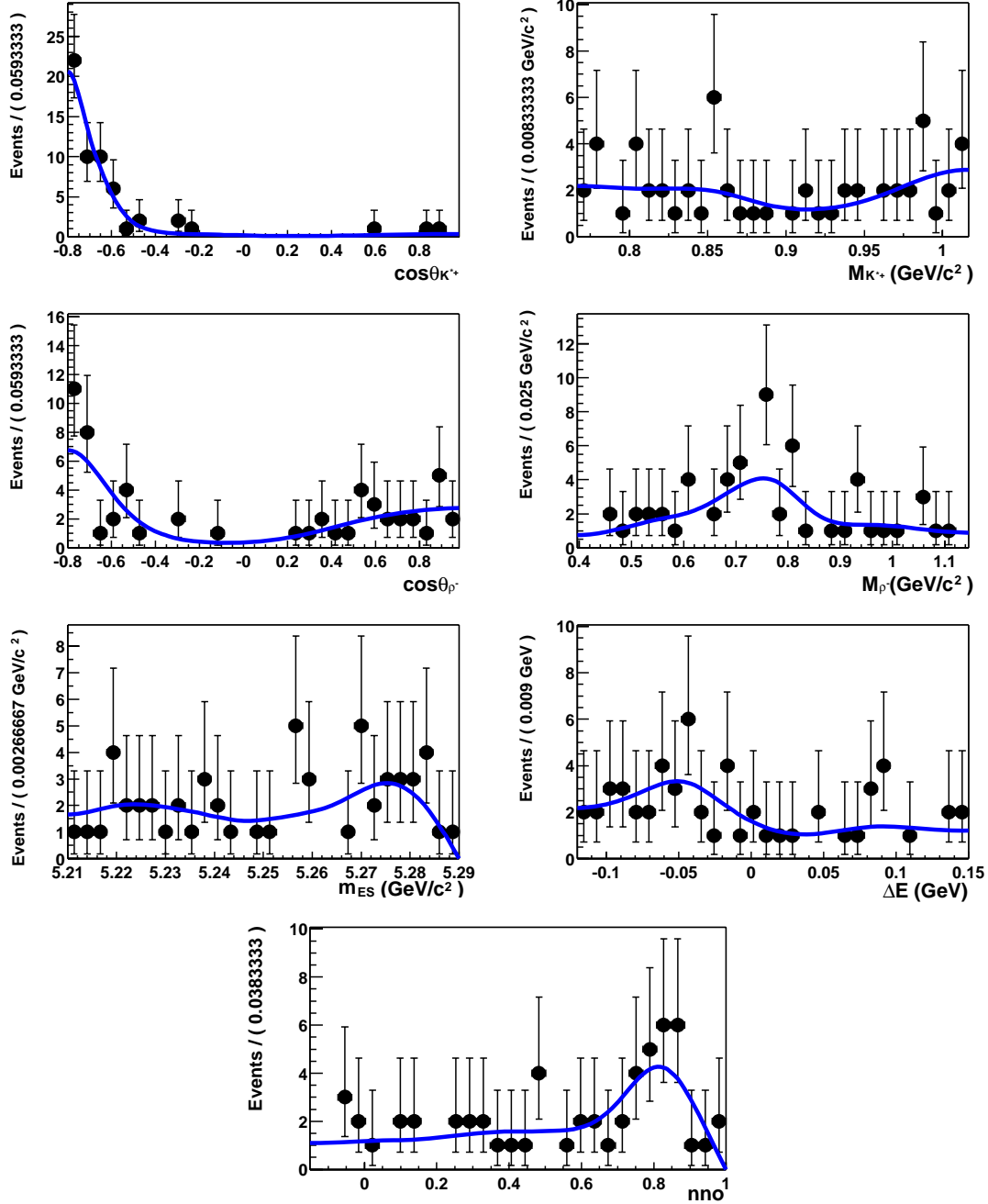


Figure B.9: *Distributions of discriminating variables for the B -background class 3, $B^0 \rightarrow (K^{**}\rho)^0$. See Figure B.6 for description.*

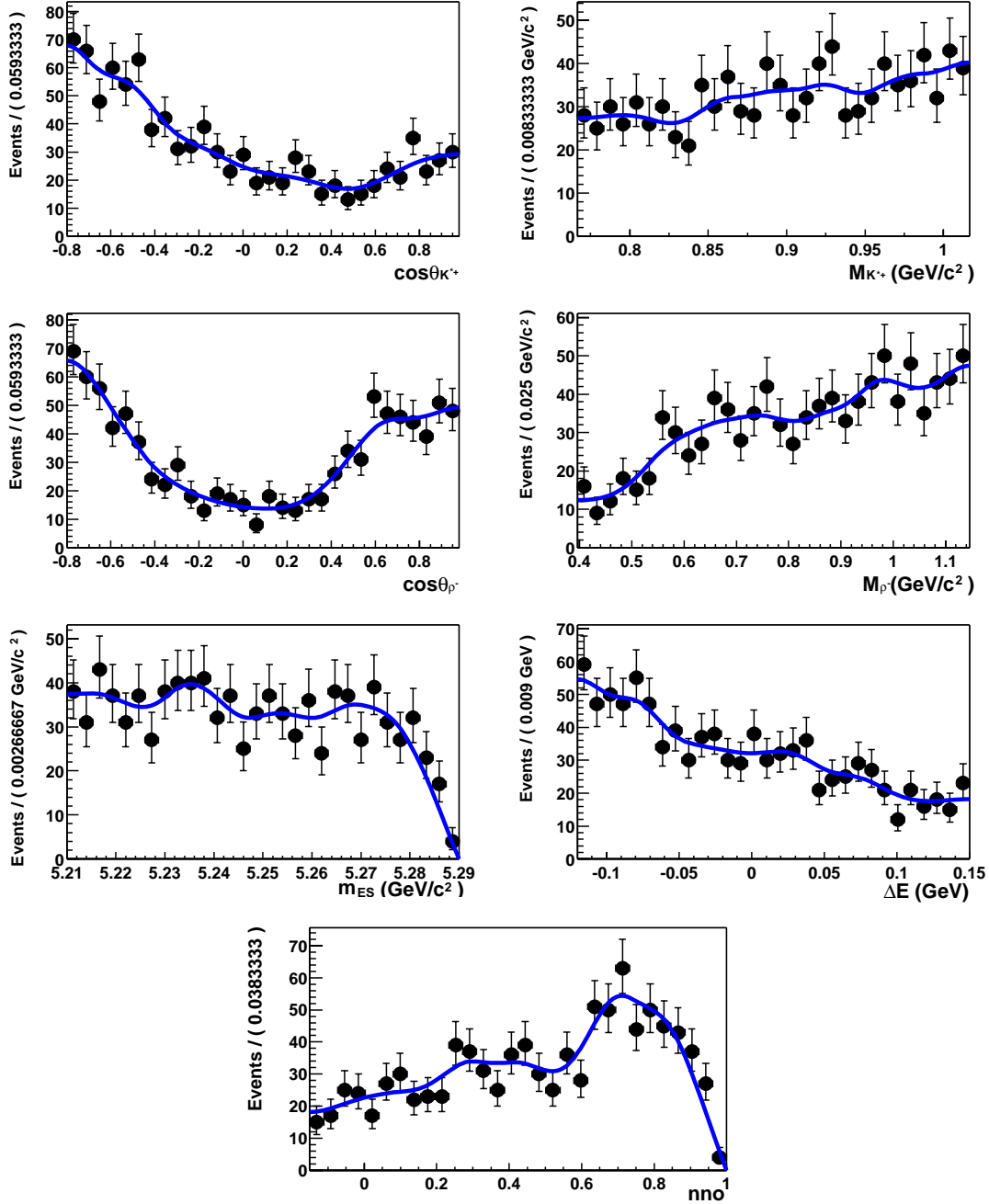


Figure B.10: Distributions of discriminating variables for the B -background class 4, $B^0 \rightarrow \text{Charm}$. See Figure B.6 for description.

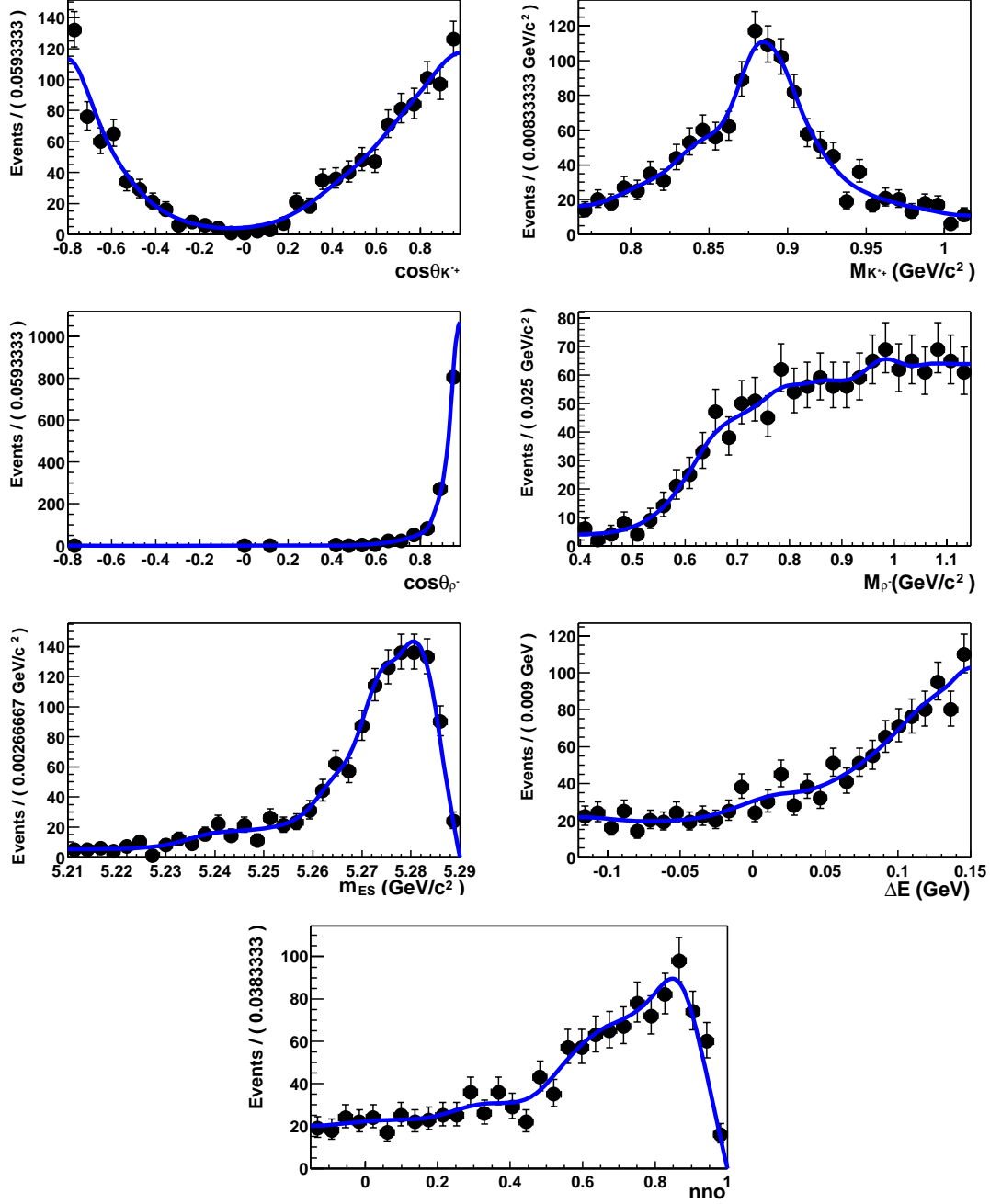


Figure B.11: Distributions of discriminating variables for the B -background class 5, $B^0 \rightarrow K^{*+}\pi^0$. See Figure B.6 for description.

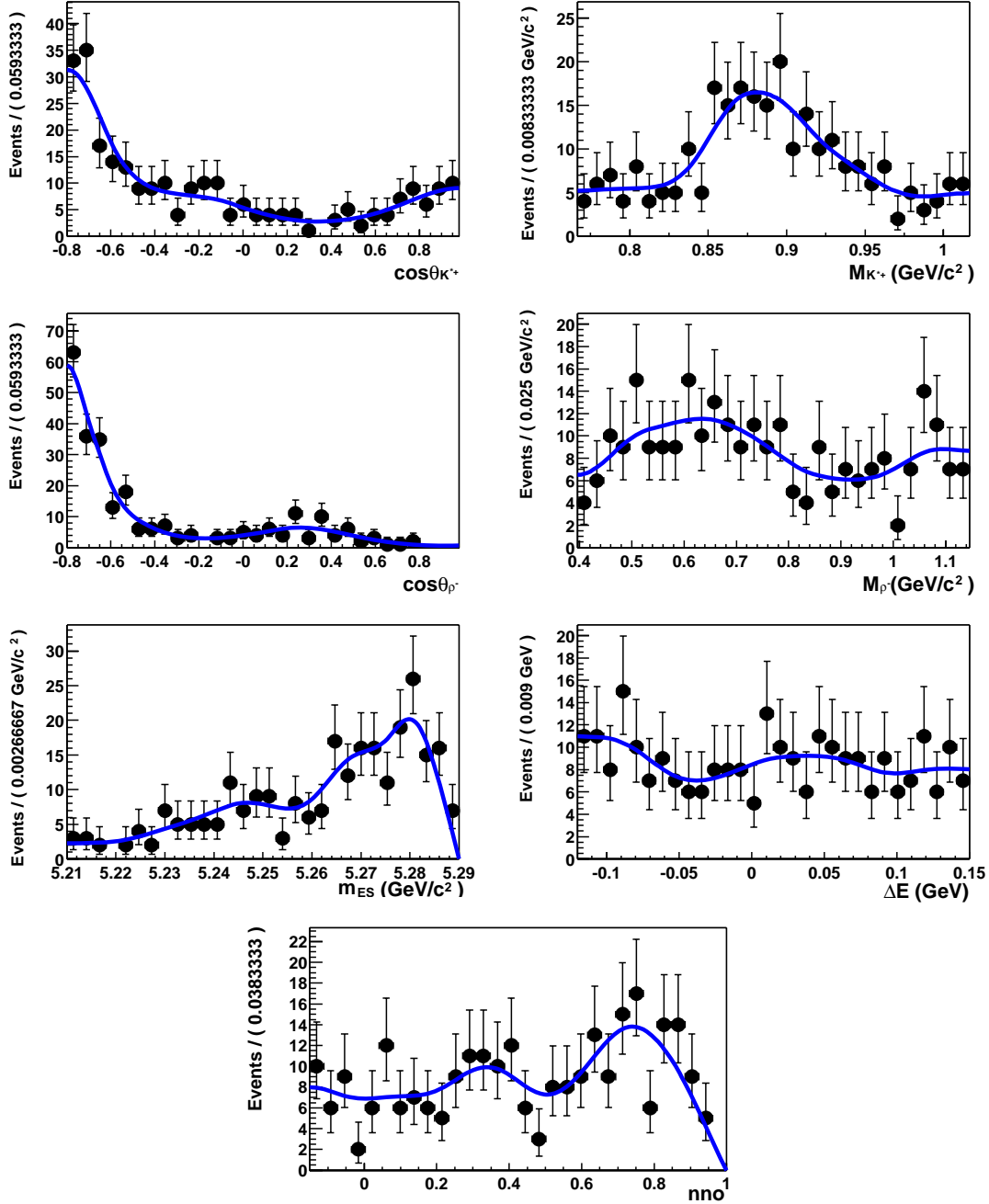


Figure B.12: *Distributions of discriminating variables for the B -background class 6, $B^+ \rightarrow K^{*+} K^{*0}$. See Figure B.6 for description.*

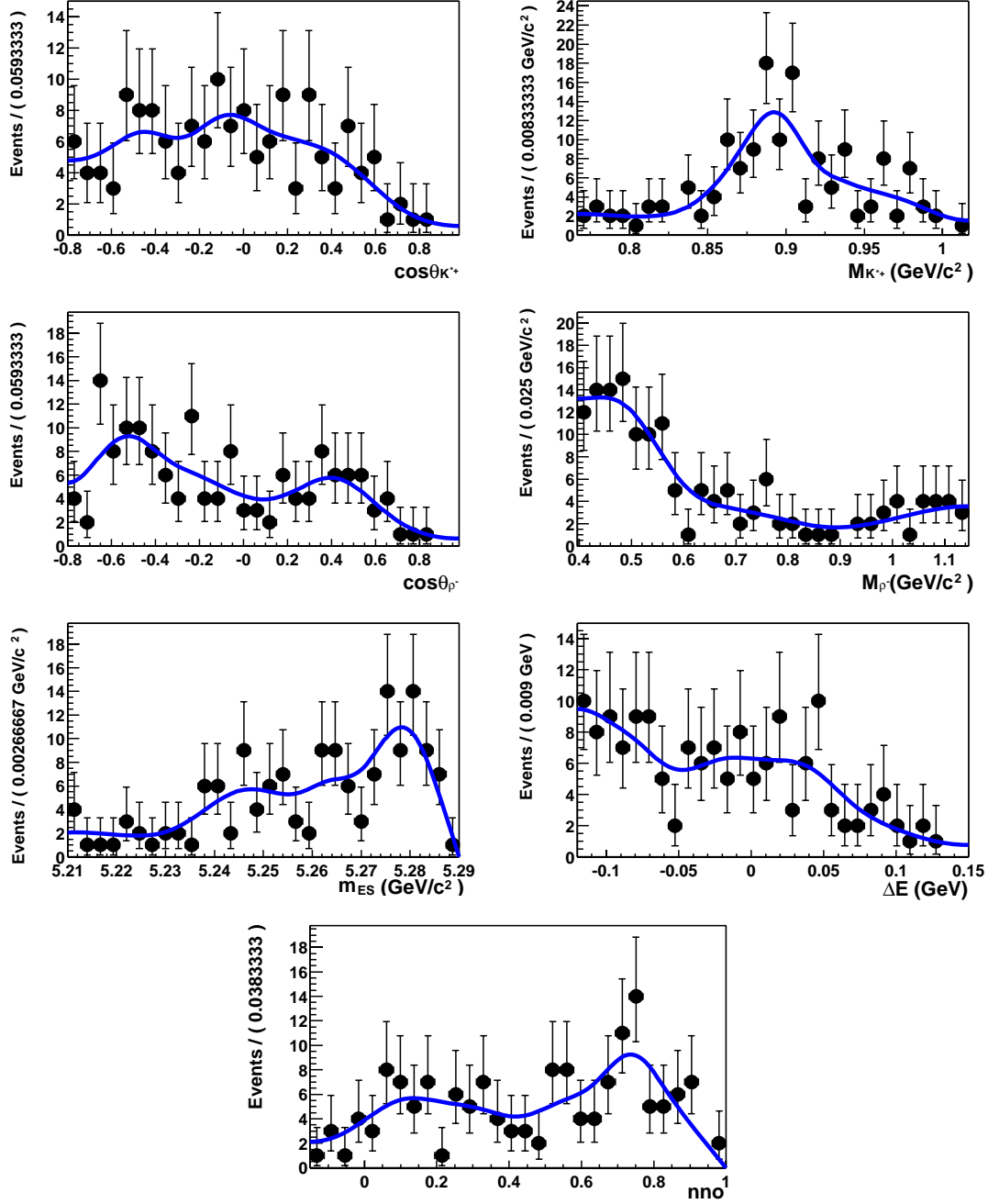


Figure B.13: Distributions of discriminating variables for the B -background class 7, $B^+ \rightarrow \omega K_{[tran]}^{*+}$. See Figure B.6 for description.

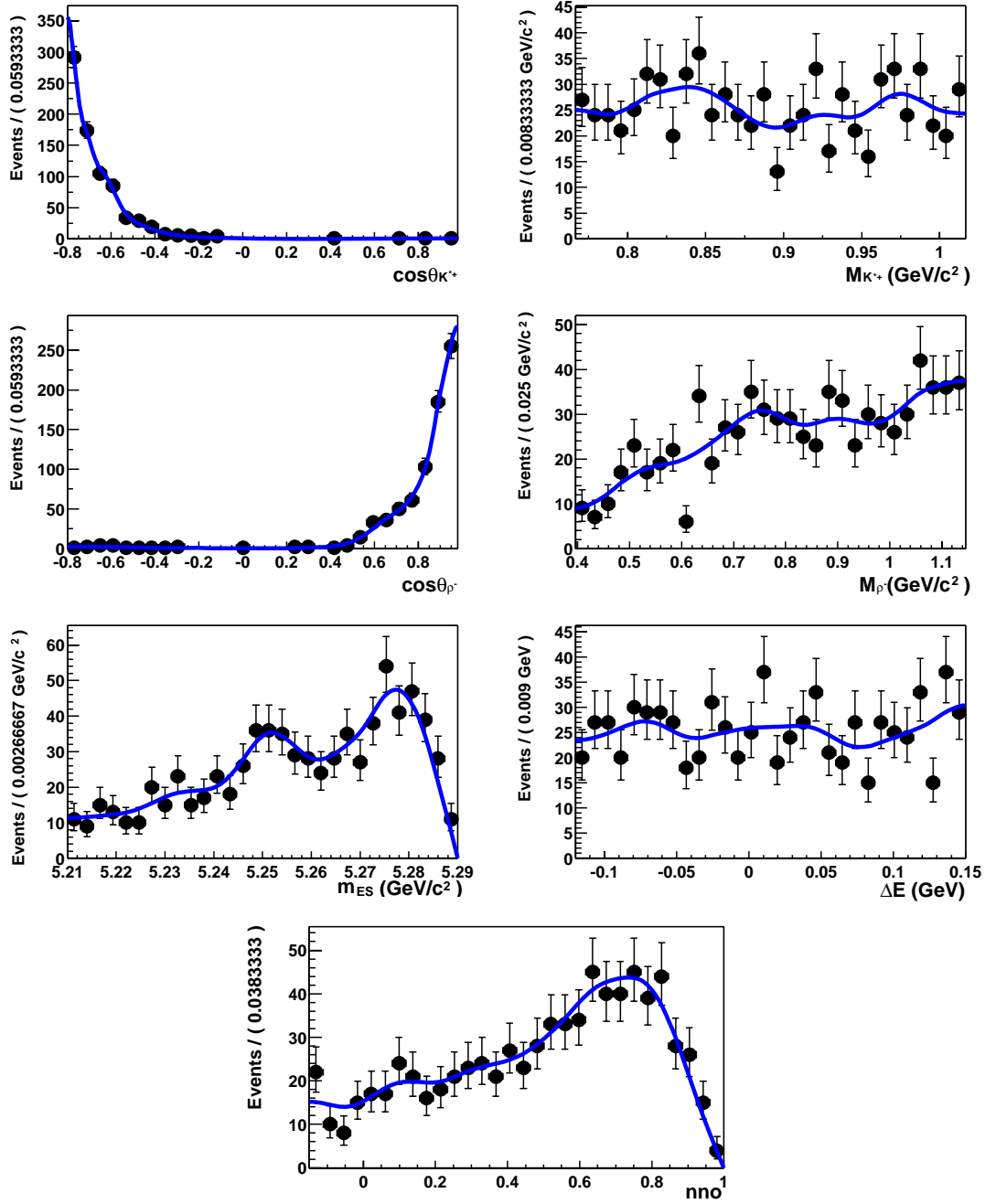


Figure B.14: Distributions of discriminating variables for the B -background class 8, $B^+ \rightarrow K^{*0} \rho_{[long]}^+$. See Figure B.6 for description.

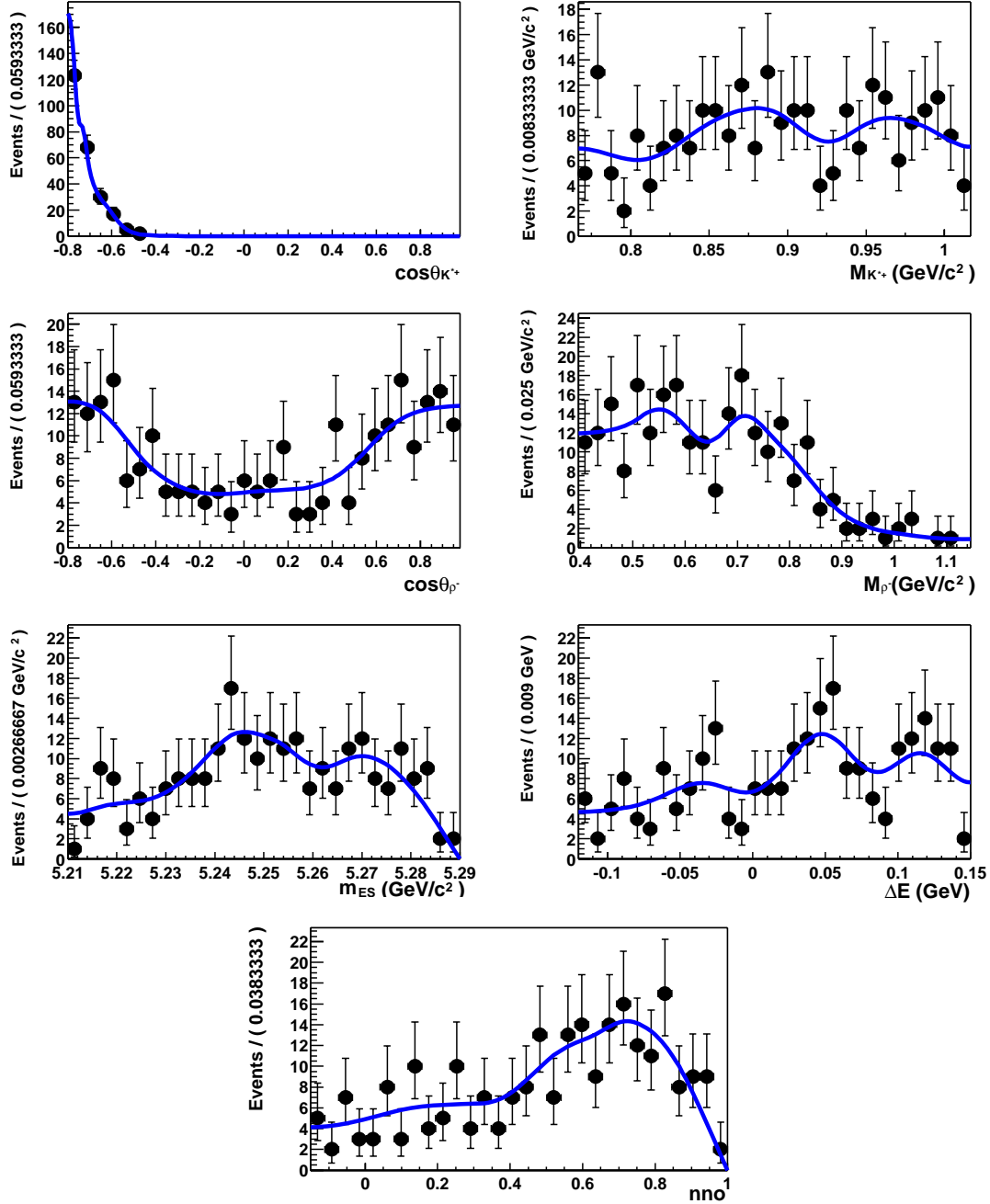


Figure B.15: Distributions of discriminating variables for the B -background class 9, $B^+ \rightarrow \phi K^+$. See Figure B.6 for description.

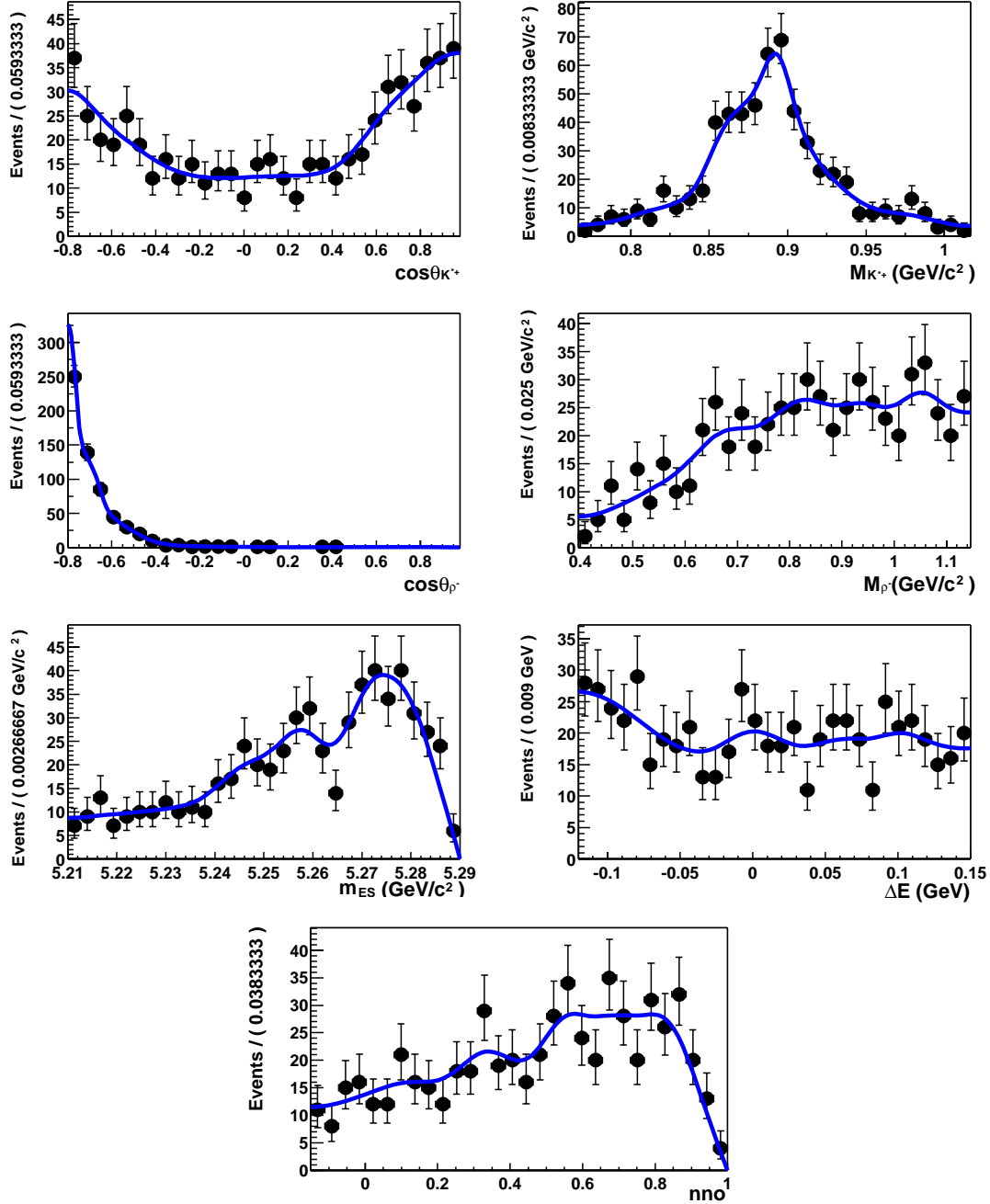


Figure B.16: Distributions of discriminating variables for the B -background class 10, $B^+ \rightarrow K^{*+} \rho^0$. See Figure B.6 for description.

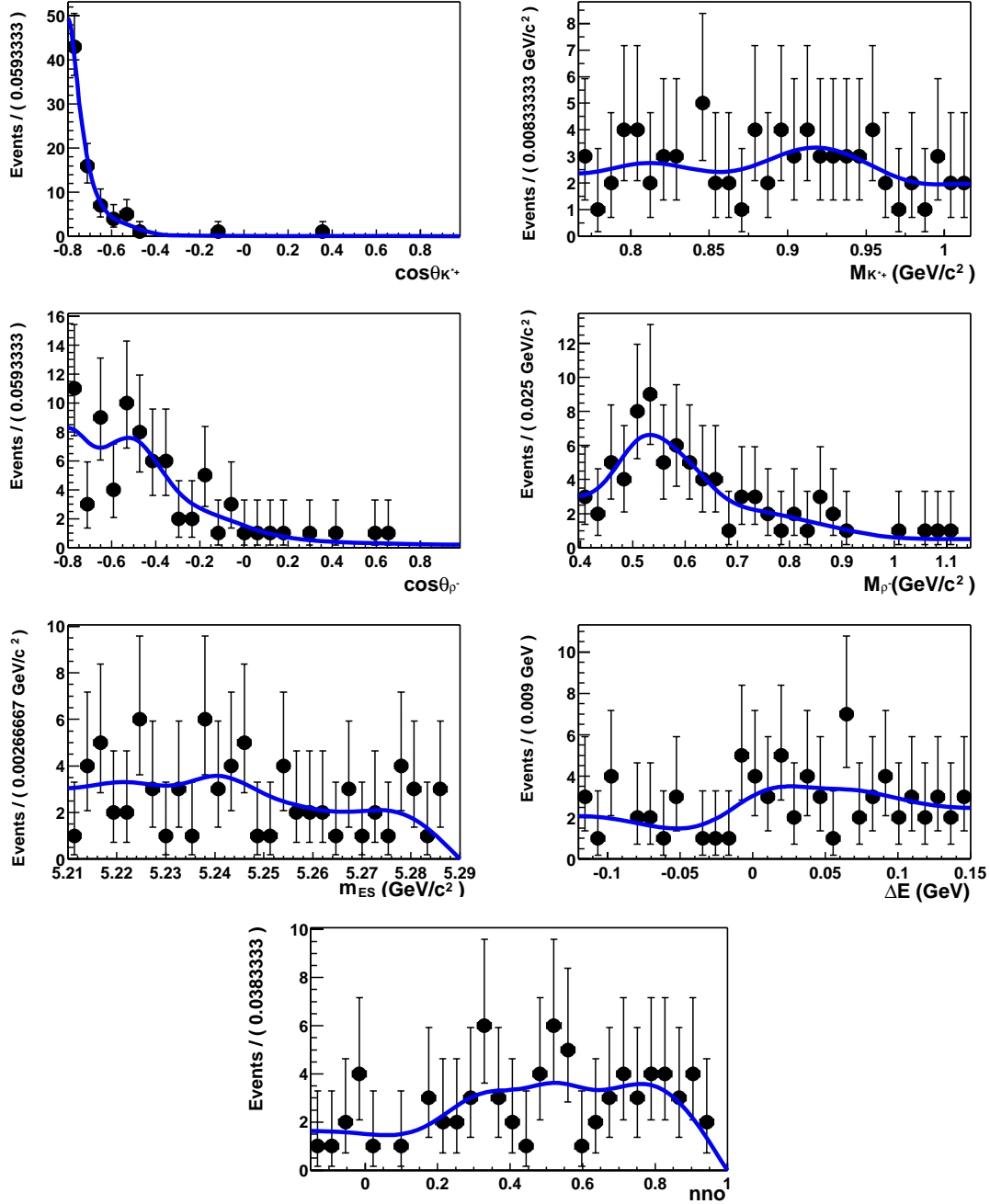


Figure B.17: Distributions of discriminating variables for the B -background class 11, $B^+ \rightarrow \eta' K^+$. See Figure B.6 for description.

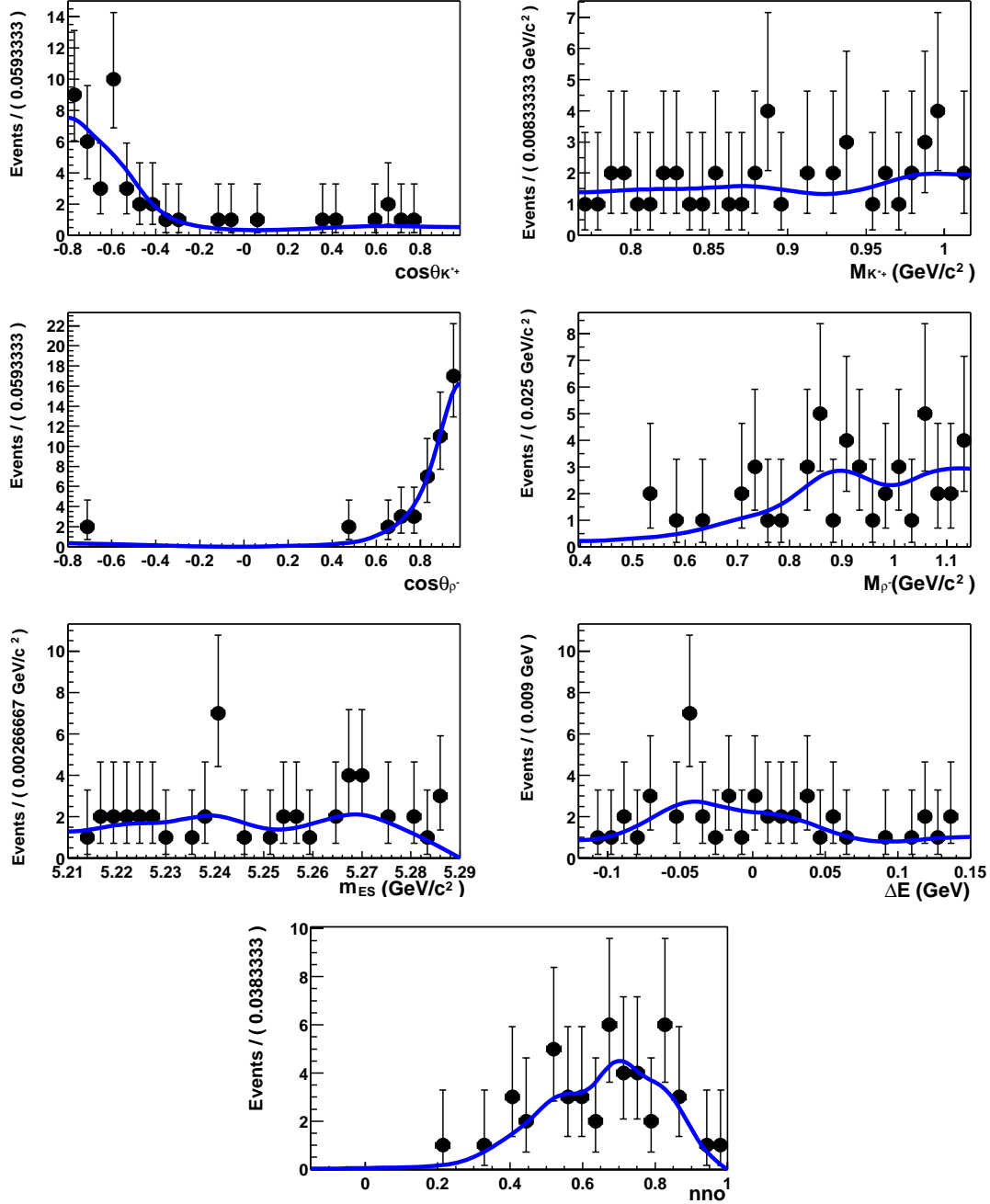


Figure B.18: Distributions of discriminating variables for the B -background class 12, $B^+ \rightarrow (K^{**}\pi)^+$. See Figure B.6 for description.

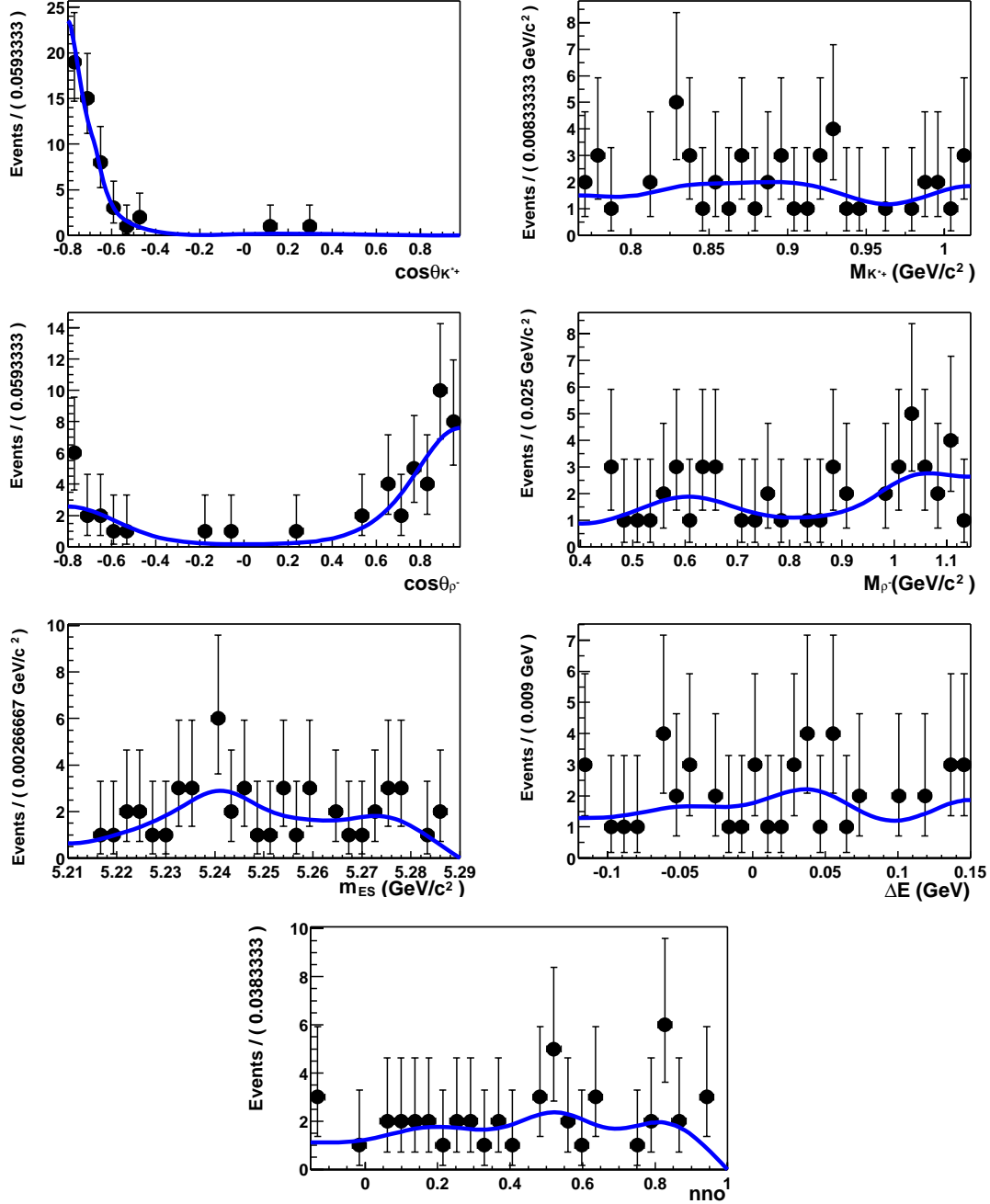


Figure B.19: Distributions of discriminating variables for the B -background class 13, $B^+ \rightarrow (K^{**}\rho)^+$. See Figure B.6 for description.

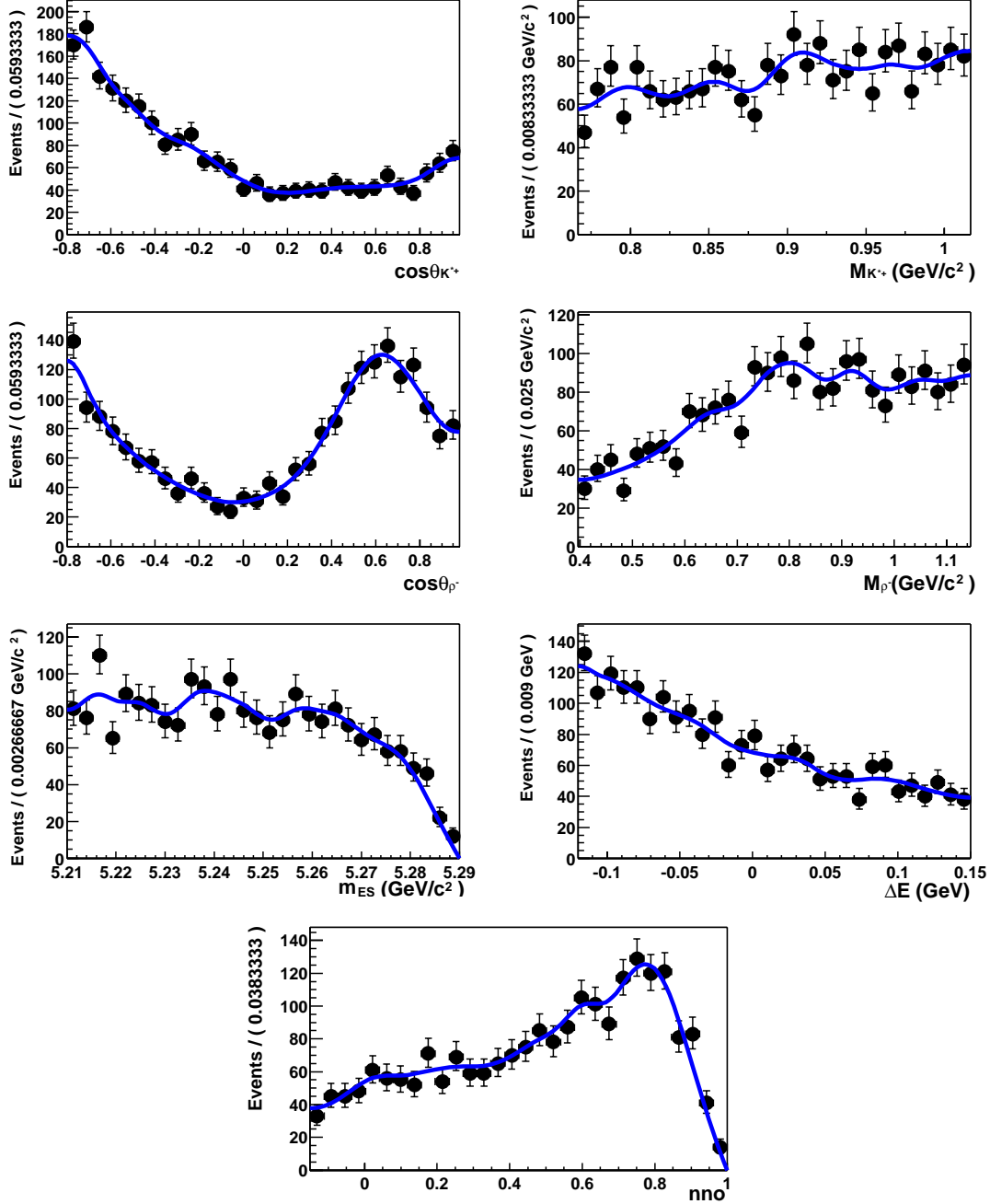


Figure B.20: Distributions of discriminating variables for the B -background class 14, $B^+ \rightarrow \text{Charm}$. See Figure B.6 for description.

Appendix C

Correlations Between Discriminating Variables

The linear correlations between the discriminating variables for signal MC, offpeak data and B backgrounds MC are calculated and presented in this appendix. These linear correlations for longitudinal signal events and transverse events are shown in Figures C.1 and C.2 respectively. Figure C.3 shows the linear correlation for offpeak events. The linear correlations for all B backgrounds events are shown from Figures C.3 to Figures C.10 class by class.

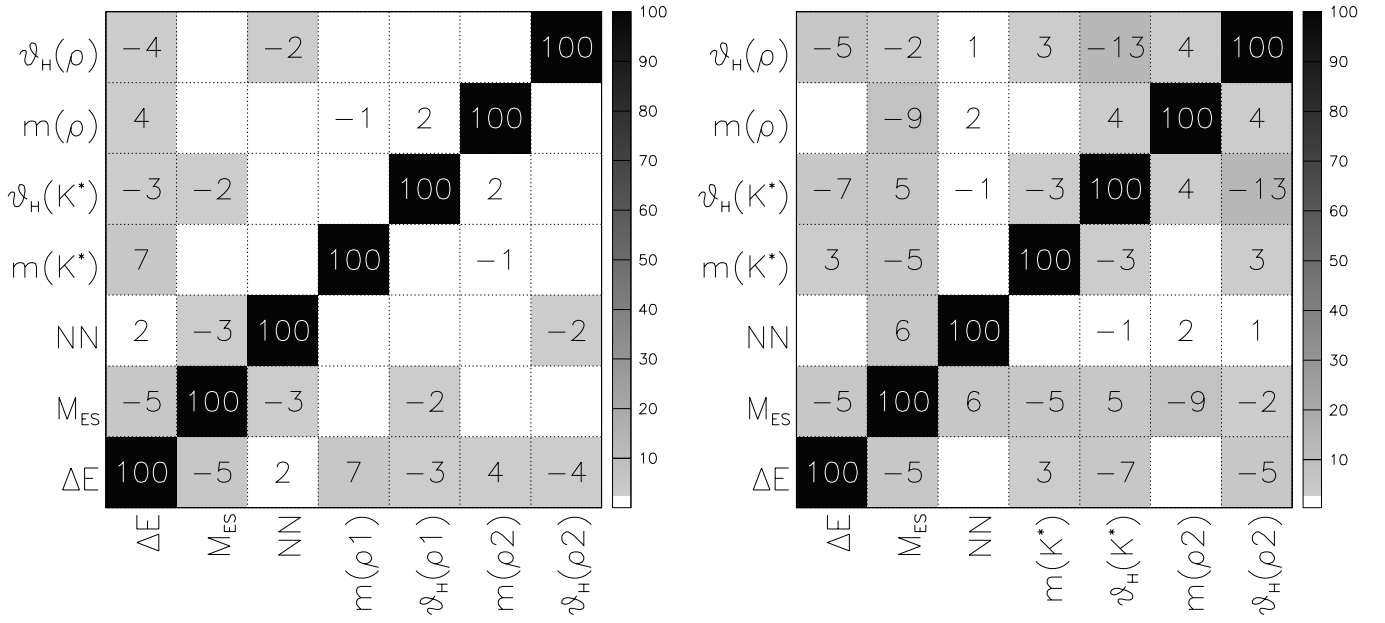


Figure C.1: Linear correlation coefficients between discriminating variables for TM longitudinal signal MC (left) and SCF longitudinal MC (right).

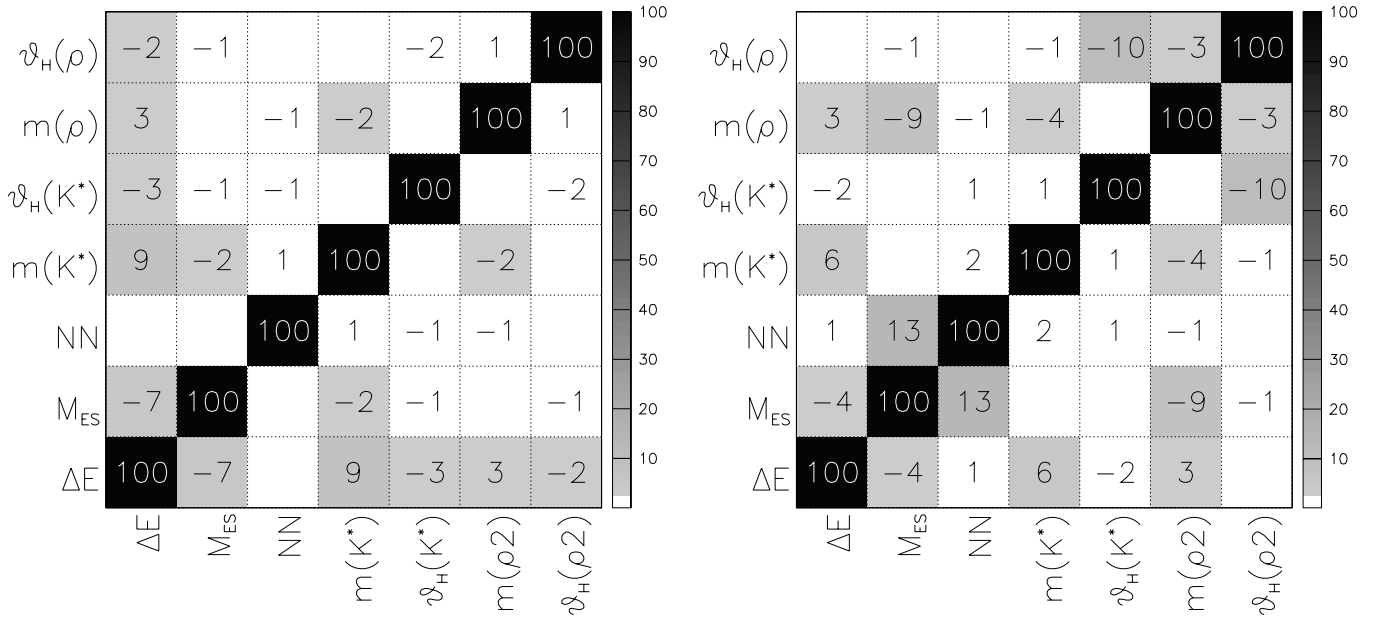


Figure C.2: Linear correlation coefficients between discriminating variables for TM transverse signal MC (left) and SCF transverse MC (right).

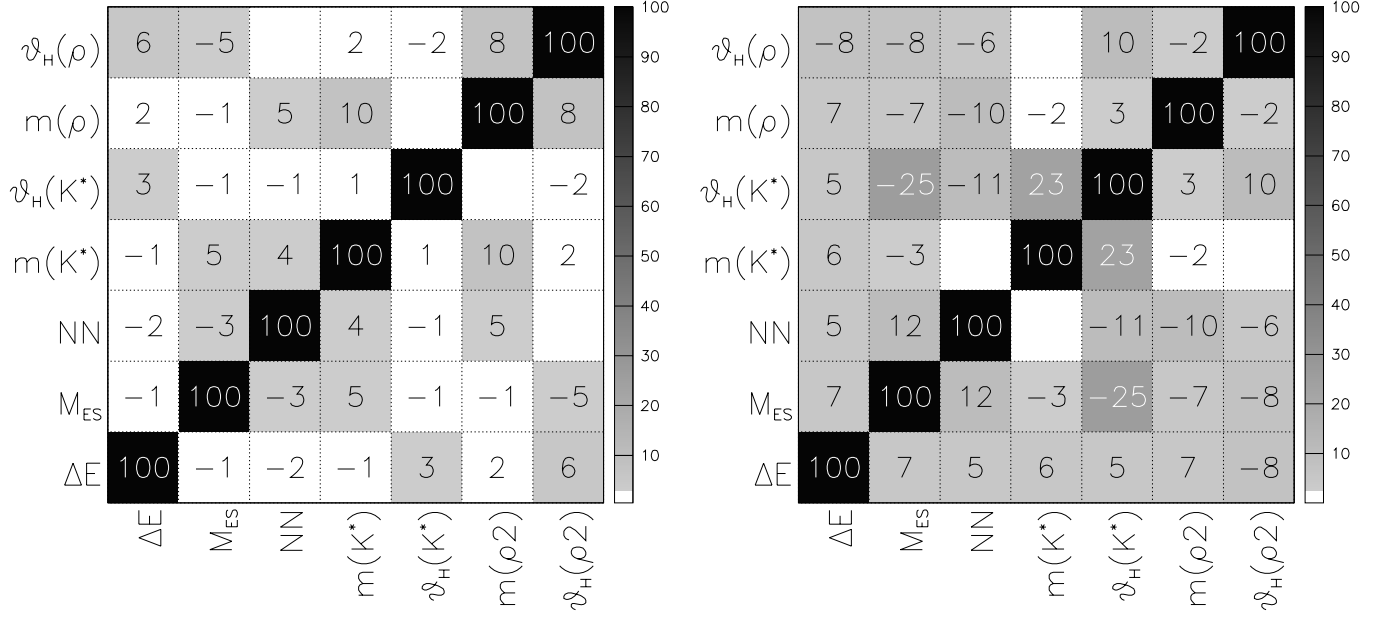


Figure C.3: Linear correlation coefficients between the discriminating variables for offpeak data (left) and B background class 0 ($B^0 \rightarrow \rho^+ \rho_{[long]}^-$) as defined in Table 3.4 (right)

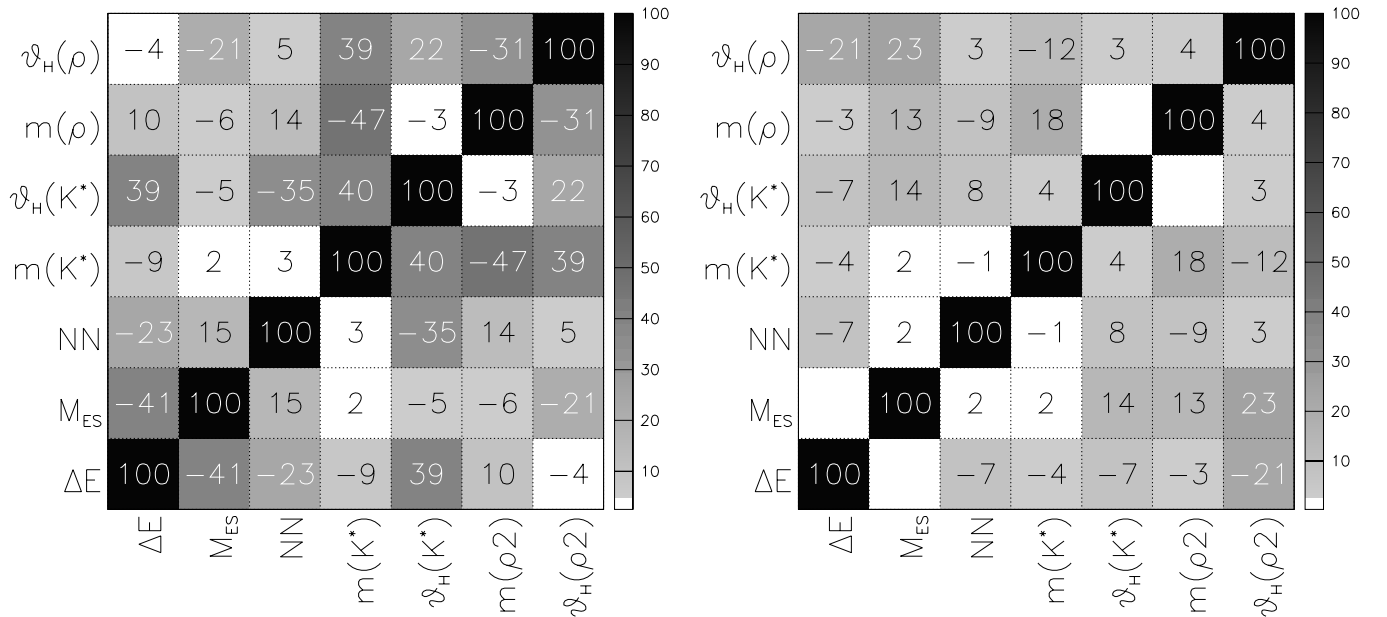


Figure C.4: Linear correlation coefficients between discriminating variables for B background class 1 ($B^0 \rightarrow a_1^+ (\rightarrow \rho^+ \pi^0) \rho_{[long]}^-$) (left) and B background class 2 ($B^0 \rightarrow (K^{**}) (\rightarrow [anything] \pi)^0$) (right) as defined in Table 3.4.

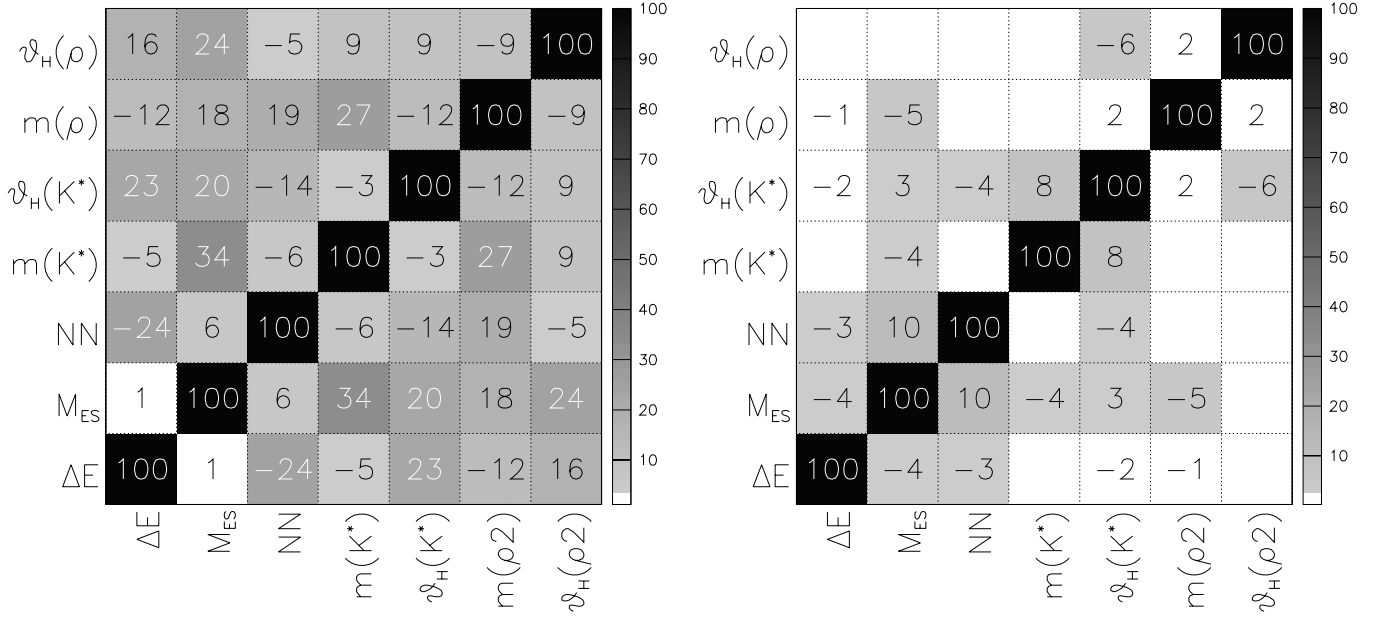


Figure C.5: Linear correlation coefficients between discriminating variables for B background class 3 ($B^0 \rightarrow (K^{**})(\rightarrow [\text{anything}]\rho)^0$) (left) and B background class 4 ($B^0 \rightarrow \text{charm}$) (right) as defined in Table 3.4.

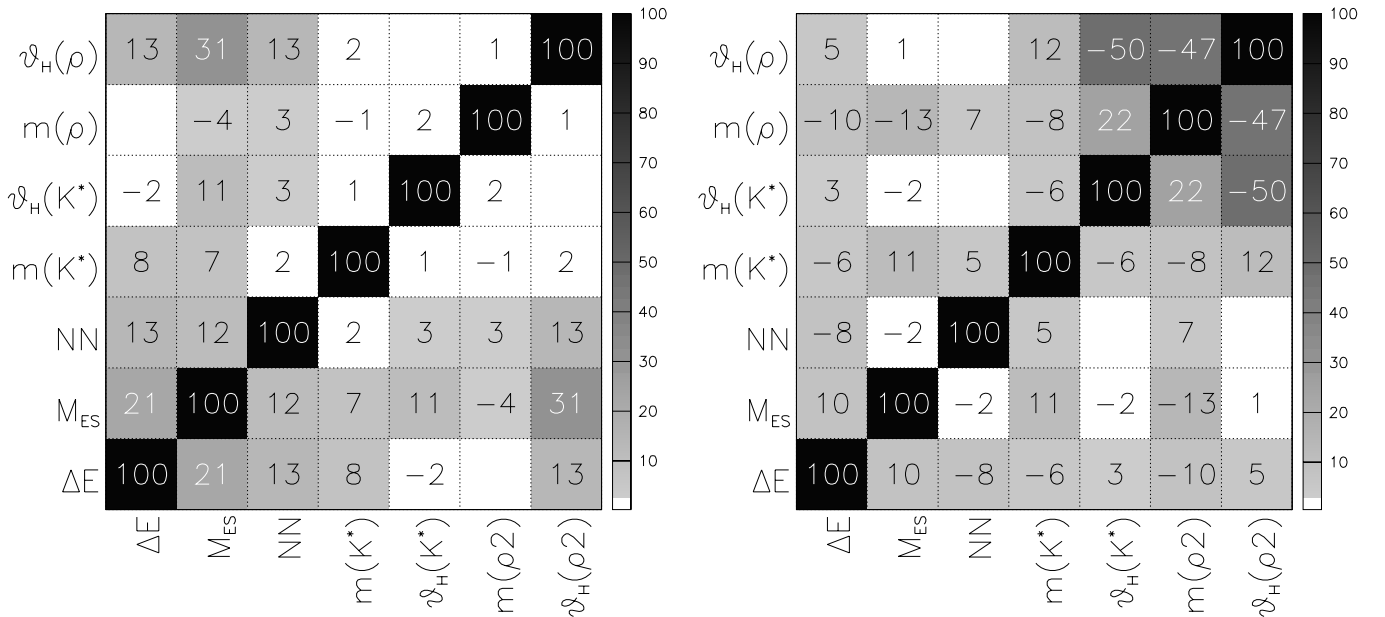


Figure C.6: Linear correlation coefficients between discriminating variables for B background class 5 ($B^+ \rightarrow K^{*+}(\rightarrow K^+\pi^0)\pi^0$) (left) and B background class 6 ($B^+ \rightarrow K^{*+}(\rightarrow K^+\pi^0)K^{*0}(\rightarrow K^+\pi^-)$) (right) as defined in Table 3.4.

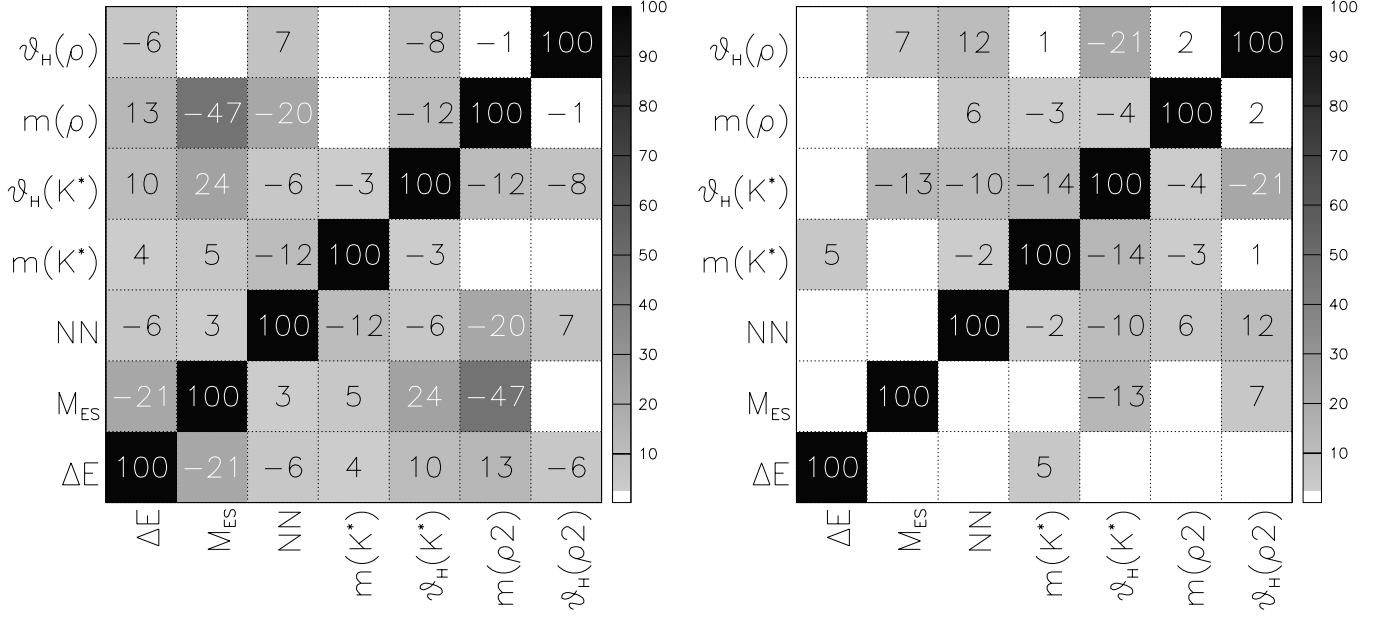


Figure C.7: Linear correlation coefficients between discriminating variables for B background class 7 ($B^+ \rightarrow \omega K^{*+}(\rightarrow K^+\pi^0)_{[tran]}$) (left) and B background class 8 ($B^+ \rightarrow K^{*0}(\rightarrow K^+\pi^-)\rho^+_{[long]}$) (right) as defined in Tables 3.4.

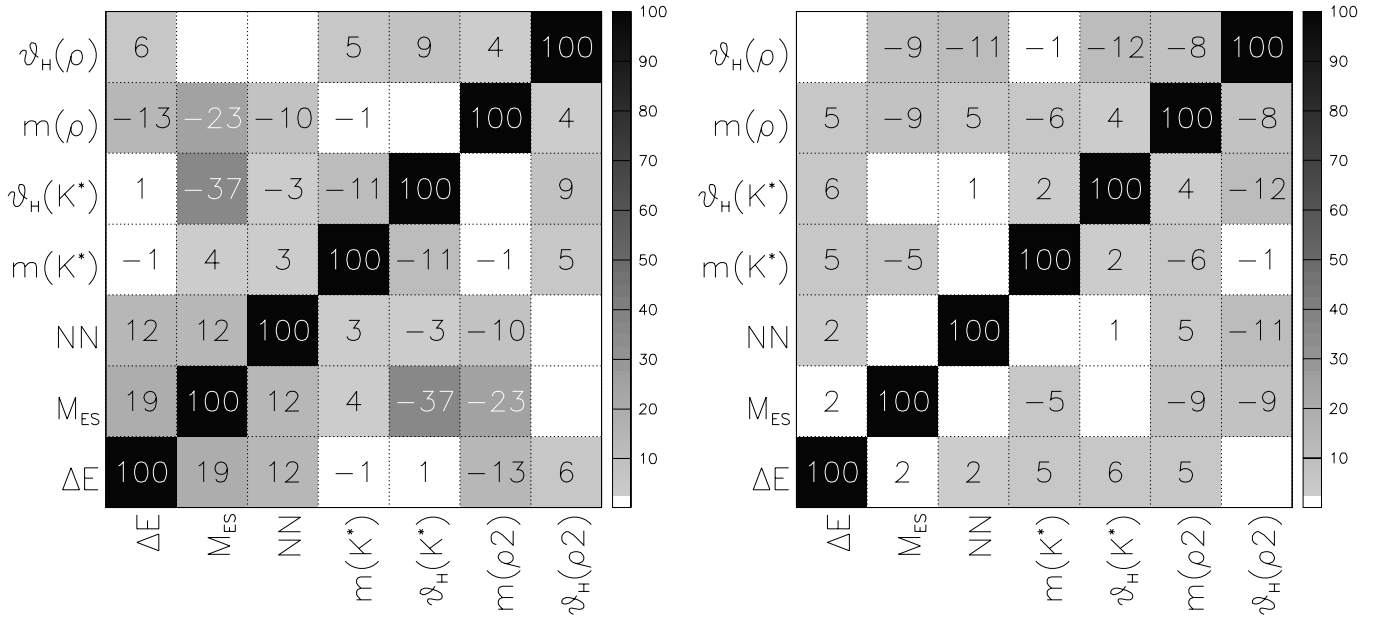


Figure C.8: Linear correlation coefficients between discriminating variables for B background class 9 ($B^+ \rightarrow \phi(\rightarrow \pi\pi\pi)K^+$) (left) and B background class 10 ($B^+ \rightarrow K^{*+}(\rightarrow K^+\pi^0)\rho^0$) (right) as defined in Table 3.4.

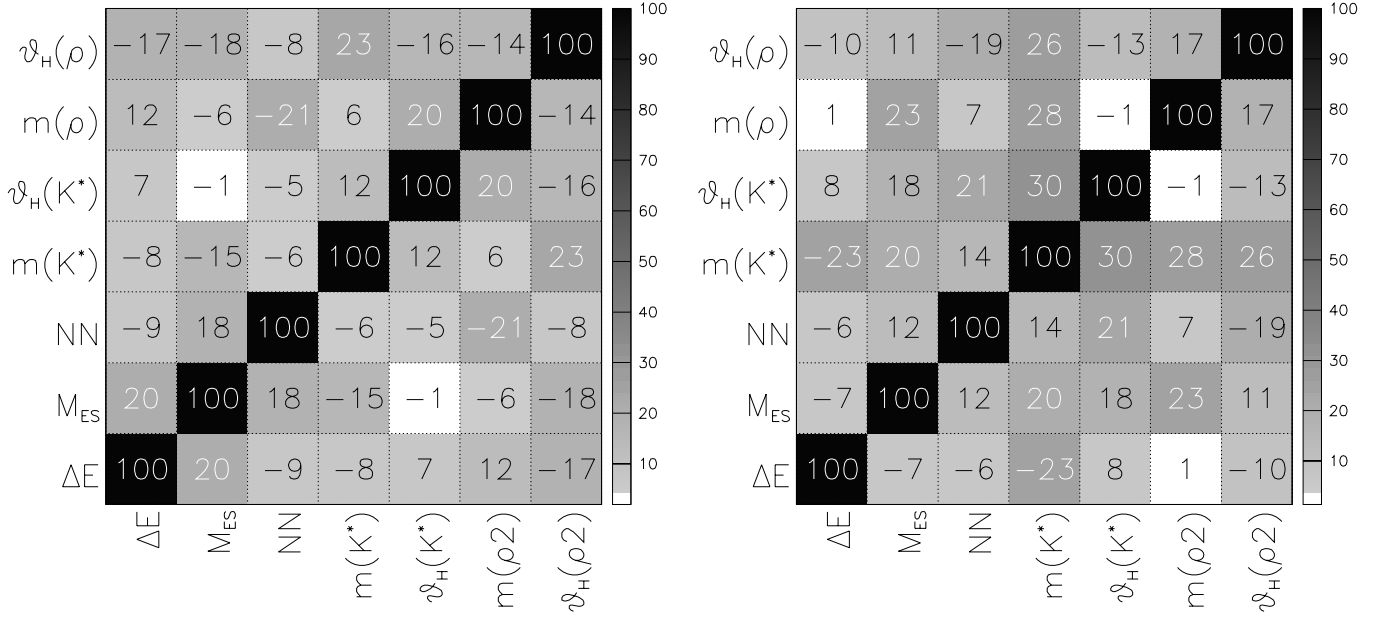


Figure C.9: Linear correlation coefficients between discriminating variables for B background class 11 ($B^+ \rightarrow \eta'(\rightarrow \rho^0 \gamma) K^+$) (left) and B background class 12 ($B^+ \rightarrow (K^{(*)}) (\rightarrow [\text{anything}] \pi)^+$) (right) as defined in Table 3.4.

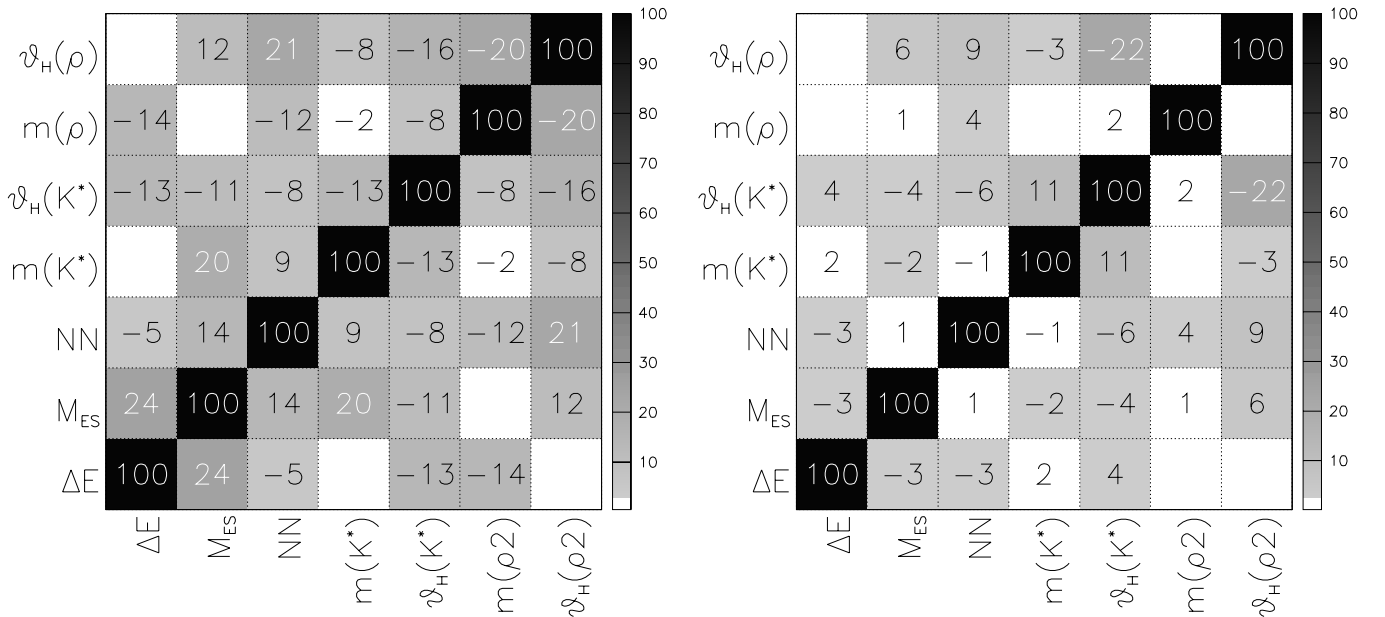


Figure C.10: Linear correlation coefficients between discriminating variables for B background class 13 ($B^+ \rightarrow (K^{(*)}) (\rightarrow [\text{anything}] \rho)^+$) (left) and B background class 14 ($B^+ \rightarrow \text{charm}$) (right) as defined in Table 3.4.

Bibliography

- [1] S.L. Glashow, “Partial Symmetries of Weak Interactions”, *Nucl. Phys.* **22**, 579 (1961);
S. Weinberg, “A Model of Leptons”, *Phys. Rev. Lett.* **19**, 1264 (1967);
A. Salam, *Elementary Particle Theory*, (Stockolm: Almquist and Wiksells) (1967).
- [2] D.J. Gross, “Twenty Five Years of Asymptotic Freedom”, *Nucl. Phys. Proc. Suppl.* **74**, 426 (1999).
- [3] P.W. Higgs, “Broken Symmetries, Massless Particlees and Gauge Fields”, *Phys. Lett.* **12**, 132 (1964).
- [4] M. Kobayashi and T. Maskawa, “CP Violation in the Renormalizable Theory of Weak Interaction”, *Prog. Theo. Phys.* **49**, 652 (1973).
- [5] S. Eidelman *et al.*, Particle Data Group, “Review of Particle Physics”, *Phys. Lett. B* **592**, 130 (2004).
- [6] L. Wolfenstein, “Parametrization of the Kobayashi-Maskawa Matrix”, *Phys. Rev. Lett.* **51**, 1945 (1983).
- [7] K.G. Wilson, “Non-Lagrangian Models of Current Algebra”, *Phys. Rev.* **179** 1499 (1969); K.G. Wilson and W. Zimmermann, “Operator Product Expansions and Composite Field Operators in the General Framework of Quantum Field Theory”, *Comm. Math. Phys.* **24**, 87 (1972).

- [8] G. Kramer and W.F. Palmer, “Branching Ratios and CP Asymmetries in the Decay $B \rightarrow VV$ ”, *Phys. Rev.* **D 45**, 193 (1992).
- [9] J. Schwinger, “Delta T=3/2 Nonleptonic Decay”, *Phys. Rev. Lett.* **12**, 630 (1964);
R.P. Feynman, in *Symmetries in Particle Physics*, ed. A. Zichichi, Acad. Press, 167 (1965);
O. Haan and B. Stech, *Nucl. Phys.* **B 22**, 448 (1970).
- [10] A. Abada *et al.*, “A Lattice Study of the Exclusive $B \rightarrow K^*\gamma$ Decay Amplitude, Using the Clover Action at $\beta = 6.0$ ”, APE Collaboration, *Phys. Lett.* **B 365**, 275 (1996);
J.M. Flynn *et al.*, “Lattice Study of the Decay $\bar{B}^0 \rightarrow \rho^+ l^- \bar{\nu}_l$: Model-Independent Determination of $|V_{ub}|$ ”, UKQCD Collaboration, *Nucl. Phys.* **B 461**, 327 (1996);
L.D. Debbio *et al.*, “Lattice-Constrained Parametrizations of Form Factors for Semileptonic and Rare Radiative B Decays”, *Phys. Lett.* **B 416**, 392 (1998).
- [11] A. Ali, V.M. Braun, and H. Simma, “Exclusive Radiative B Decays in the Light Cone QCD Sum Rule Approach”, *Z. Phys.* **C 63**, 437 (1994);
P. Ball and V.M. Braun, “Use and Misuse of QCD Sum Rules in Heavy-to-Light Transitions: The Decay $B \rightarrow \rho e \nu$ Reexamined”, *Phys. Rev.* **D 55**, 5561 (1997).
- [12] J.D. Bjorken, “Topics in B-Physics”, *Nucl. Phys. (Proc. Suppl.)* **B 11**, 325 (1989).
- [13] BABAR Collaboration, “Study of the Decay $B^0(\bar{B}^0) \rightarrow \rho^+ \rho^-$, and Constraints on the Cabibbo-Kobayashi-Maskawa Angle α ”, *Phys. Rev. Lett.* **93**, 231801 (2004).
- [14] BABAR Collaboration, “Rates, Polarizations, and Asymmetries in Charmless Vector-Vector B Meson Decays”, *Phys. Rev. Lett.* **91**, 171802 (2003).
- [15] Belle Collaboration, “Observation of $B^\mp \rightarrow \rho^\mp \rho^0$ ”, *Phys. Rev. Lett.* **91**, 221801 (2003).

- [16] *BABAR* Collaboration, “Measurements of Branching Fraction, Polarization, and Direct CP-Violating Charge Asymmetry in $B^+ \rightarrow K^{*0} \rho^+$ Decays”, ICHEP, Beijing, China (2004). hep-ex/0408093.
- [17] Belle Collaboration, “Measurements of Branching Fractions and Polarization in $B \rightarrow K^* \rho$ Decays”, ICHEP, Beijing, China (2004). hep-ex/0408102.
- [18] *BABAR* Collaboration, “Measurement of the $B^0 \rightarrow \phi K^{*0}$ Decay Amplitudes”, *Phys. Rev. Lett.* **93**, 231804 (2004).
- [19] Belle Collaboration, “Measurement of Branching Fractions and Polarization in $B \rightarrow \phi K^{(*)}$ Decays”, *Phys. Rev. Lett.* **91**, 201801 (2003).
- [20] J. Seeman *et al.*, “Results and Plans of the PEP-II B Factory”, *Presented at 9th European Particle Accelerator Conference (EPAC 2004)*, Lucerne, Switzerland, 5-9 Jul. 2004. SLAC-PUB-10547.
- [21] M. Sullivan, “ B Factory Interaction Region Design”, *Proceedings of the IEEE Particle Accelerator Conference (PAC97)*, Vancouver, BC, Canada (1997). SLAC-PUB-7563.
- [22] J.L. Turner *et al.*, “Trickle-Charge: A New Operational Mode for PEP-II”, *Presented at 9th European Particle Accelerator Conference (EPAC 2004)*, Lucerne, Switzerland, 5-9 Jul. 2004.
- [23] B.N. Ratcliff, “The B Factory Detector for PEP-II: a Status Report”, (1992). SLAC-PUB-5946;
 B.N. Ratcliff, “The DIRC Counter: A New Type of Particle Identification Device for B Factories”, (1993). SLAC-PUB-6047;
 P. Coyle *et al.*, “The DIRC Counter: A New Type of Particle Identification Device for B Factories”, *Nucl. Instr. Meth.* **A 343**, 292 (1994). SLAC-PUB-6371.

- [24] W.R. Nelson *et al.*, “Electron-Induced Cascade Showers in Copper and Lead at 1 GeV”, *Phys. Rev.* **149**, 201 (1966).
- [25] P.F. Harrison, “Blind Analysis”, *J. Phys.* **G 28**, 2679 (2002).
- [26] D.J. Lange, “The EvtGen Particle Decay Simulation Package”, *Nucl. Instr. Meth.* **A 462**, 152 (2001).
- [27] T. Sjöstrand, “PYTHIA 5.7 and JETSET 7.4 Physics and Manual”, CERN-TH7112-93-REV (1995), hep-ex/9508391.
- [28] S. Agostinelli *et al.*, “GEANT4 - a Simulation Toolkit”, *Nucl. Instr. Meth.* **A 506**, 250 (2003).
- [29] A. Drescher *et al.*, “The Argus Electron-Photon Calorimeter III. Electron-Hadron Separation”, *Nucl. Instr. Meth* **A 237**, 464 (1985).
- [30] ARGUS Collaboration, H. Albrecht *et al.*, “Exclusive Hadronic Decays of B Mesons”, *Z. Phys.* **C 48**, 543 (1990).
- [31] P. Gay, B. Michel, J. Proriot, and O. Deschamps, “Tagging Higgs Bosons in Hadronic LEP-II Events with Neural Networks”, *New Computing Techniques in Physics Research*, Pisa, 725 (1995).
- [32] M. Fisher, “The Use of Multiple Measurements in Taxonomic Problems”, *Annals of Eugenics* **7**, 179 (1936).
- [33] A. Kagan, “Polarization in $B \rightarrow VV$ Decays”, *Phys. Lett.* **B 601**, 151 (2004). hep-ph/0405134.
- [34] R. Aleksan *et al.*, “Measurement of Branching Fractions and CP -Violating Asymmetries in $B^0 \rightarrow \rho^\pm h^\mp$ ”, *BABAR Analysis Documents* #350 (2003).

- [35] D. Antreasyan *et al.*, *Crystal Ball Note* 321 (1983).
- [36] K.S. Cranmer, “Kernel Estimation for Parameterization of Discriminant Variable Distributions”, *Comput. Phys. Commun.* **136**, 198 (2001).
- [37] A. Höcker, S. Laplace F. Le Diberder, V. Shelkov *et al.*, “Search for $B^0 \rightarrow a_0(980)\pi$ ”, *BABAR Analysis Document #141* (2001).
- [38] *BABAR* Collaboration, “Measurement of Branching Fractions and Charge Asymmetries in $B^\pm \rightarrow \rho^\pm \pi^0$ and $B^\pm \rightarrow \rho^0 \pi^\pm$ Decays, and Search for $B^0 \rightarrow \rho^0 \pi^0$ ”, *Phys. Rev. Lett.* **93**, 051802 (2004).
- [39] “Systematic Corrections for the Neutrals”,
<http://www.slac.stanford.edu/BFROOT>
[/www/Physics/Tools/BetaTools/MicroNeutralKilling-RUN2.html](http://www/Physics/Tools/BetaTools/MicroNeutralKilling-RUN2.html)
- [40] “Tracking Efficiency Task Force in 2004”,
<http://www.slac.stanford.edu/BFROOT>
[/www/Physics/TrackEfficTaskForce/TrackingTaskForce-2004.html](http://www/Physics/TrackEfficTaskForce/TrackingTaskForce-2004.html)